FEDERAL UNIVERSITY OF UBERLANDIA
MECHANICAL ENGINEERING FACULTY
MECHANICAL ENGINEERING

IAGO TETSUO NONAKA

Modeling and Simulation of Multicomponent Evaporative Sprays in Generic Conditions

Uberlândia

2025

IAGO TETSUO NONAKA

Modeling and Simulation of Multicomponent Evaporative Sprays in Generic Conditions

Dissertation submitted to the Graduate Program in Mechanical Engineering at the Federal University of Uberlandia, as part of the requirements for the degree of Master in Mechanical Engineering.

Area of Concentration: Heat Transfer and Fluid Mechanics

Advisor: Dr. João Marcelo Vedovotto

Uberlândia

2025

IAGO TETSUO NONAKA

Modeling and Simulation of Multicomponent Evaporative Sprays in Generic Conditions

Dissertation submitted to the Graduate Program in Mechanical Engineering at the Federal University of Uberlandia, as part of the requirements for the degree of Master in Mechanical Engineering.

Area of Concentration: Heat Transfer and Fluid Mechanics

Uberlândia, 2025

Examination Committee:

Prof. Dr. João Marcelo Vedovotto (UFU)

Prof. Dr. Francisco José de Souza (UFU)

Prof. Dr. Fernando Luiz Sacomano Filho (USP)

Eng. Dr. Ricardo Serfaty (PETROBRAS)

International Cataloguing-in-Publication Data (CIP)
UFU Library System, MG, Brazil.

N812m 2025

Nonaka, Iago Tetsuo, 1998-
Modeling and Simulation of Multicomponent Evaporative Sprays in Generic Conditions [electronic resource] / Iago Tetsuo Nonaka. - 2025.

Advisor: João Marcelo Vedovotto.
Dissertation (Master's) - Federal University of Uberlândia, Postgraduate Program in Mechanical Engineering.
Access mode: Internet.
Available at: http://doi.org/10.14393/ufu.di.2025.5579
Includes bibliography.
Includes illustrations.

1. Mechanical engineering. 2. Heat - Transmission. 3. Fluid mechanics. I. Vedovotto, João Marcelo, 1981-, (Orient.). II. Federal University of Uberlândia, Postgraduate Program in Mechanical Engineering. III. Título.

CDU: 621.01

Rejâne Maria da Silva
Librarian - Documentalist – CRB6/1925

UNIVERSIDADE FEDERAL DE UBERLÂNDIA
Coordenação do Programa de Pós-Graduação em Engenharia Mecânica
Av. João Naves de Ávila, nº 2121, Bloco 1M, Sala 212 - Bairro Santa Mônica, Uberlândia-MG, CEP 38400-902
Telefone: (34) 3239-4282 - www.posmecanicaufu.com.br - secposmec@mecanica.ufu.br

ATA DE DEFESA - PÓS-GRADUAÇÃO

Programa de Pós-Graduação em:	Engenharia Mecânica				
Defesa de:	Dissertação de Mestrado Acadêmico, número 664, PPGEM				
Data:	06 de agosto de 2025	Hora de início:	13:30	Hora de encerramento:	[16:30]
Matrícula do Discente:	12412EMC011				
Nome do Discente:	Iago Tetsuo Nonaka				
Título do Trabalho:	Modeling and Simulation of Multicomponent Evaporative Sprays in Generic Conditions				
Área de concentração:	Transferência de Calor e Mecânica dos Fluidos				
Linha de pesquisa:	Dinâmica dos Fluidos e Transferência de Calor				
Projeto de Pesquisa de vinculação:	Modelagem matemática e computacional de processos de corrosão e erosão em superfícies metálicas em tubulações das Unidades de Refino – Petrobras/MFLab-FEMEC-UFU				

Reuniu-se por videoconferência, a Banca Examinadora, designada pelo Colegiado do Programa de Pós-graduação em Engenharia Mecânica, assim composta: Prof. Dr. Ricardo Serfaty - PETROBRAS; Prof. Dr. Fernando Luiz Sacomano Filho - USP; Prof. Dr. Francisco José de Sousa - UFU e Prof. Dr. João Marcelo Vedovotto - UFU, orientador(a) do(a) candidato(a).

Iniciando os trabalhos o presidente da mesa, Dr. João Marcelo Vedovotto, apresentou a Comissão Examinadora e o candidato(a), agradeceu a presença do público, e concedeu ao Discente a palavra para a exposição do seu trabalho. A duração da apresentação do Discente e o tempo de arguição e resposta foram conforme as normas do Programa.

A seguir o senhor(a) presidente concedeu a palavra, pela ordem sucessivamente, aos(às) examinadores(as), que passaram a arguir o(a) candidato(a). Ultimada a arguição, que se desenvolveu dentro dos termos regimentais, a Banca, em sessão secreta, atribuiu o resultado final, considerando o(a) candidato(a):

Aprovado(a).

Esta defesa faz parte dos requisitos necessários à obtenção do título de Mestre.

O competente diploma será expedido após cumprimento dos demais requisitos, conforme as normas do Programa, a legislação pertinente e a regulamentação interna da UFU.

Nada mais havendo a tratar foram encerrados os trabalhos. Foi lavrada a presente ata que após lida e achada conforme foi assinada pela Banca Examinadora.

Documento assinado eletronicamente por **João Marcelo Vedovotto**, **Professor(a) do Magistério Superior**, em 06/08/2025, às 16:34, conforme horário oficial de Brasília, com fundamento no art. 6º, § 1º, do Decreto nº 8.539, de 8 de outubro de 2015.

Documento assinado eletronicamente por **Francisco José de Souza**, **Professor(a) do Magistério Superior**, em 06/08/2025, às 16:34, conforme horário oficial de Brasília, com fundamento no art. 6º, § 1º, do Decreto nº 8.539, de 8 de outubro de 2015.

Documento assinado eletronicamente por **Fernando Luiz Sacomano Filho**, **Usuário Externo**, em 06/08/2025, às 16:37, conforme horário oficial de Brasília, com fundamento no art. 6º, § 1º, do Decreto nº 8.539, de 8 de outubro de 2015.

Documento assinado eletronicamente por **ricardo serfaty**, **Usuário Externo**, em 25/08/2025, às 08:16, conforme horário oficial de Brasília, com fundamento no art. 6º, § 1º, do Decreto nº 8.539, de 8 de outubro de 2015.

A autenticidade deste documento pode ser conferida no site https://www.sei.ufu.br/sei/controlador_externo.php?acao=documento_conferir&id_orgao_acesso_externo=0, informando o código verificador **6535267** e o código CRC **93612F6E**.

Referência: Processo nº 23117.050621/2025-99 SEI nº 6535267

To my family,

whose unconditional support, love,

and encouragement have been

my foundation throughout this journey.

ACKNOWLEDGEMENTS

The work presented in this dissertation was carried out during my time at the Fluid Mechanics Laboratory (MFLab). My interest in propulsion systems was first sparked during the course taught by Professor João Marcelo Vedovotto and my participation in Tucano Aerodesign. Since then, studying propulsion-related topics has been a source of great enthusiasm. I am especially grateful to Professor Vedovotto, whose unwavering support and guidance played a crucial role in the successful completion of this dissertation and made my Master's journey both enriching and enjoyable.

I am deeply thankful to my father, Flavio, who has always been a role model to me—both professionally and personally—and to my mother, Flavia, whose continuous support and encouragement gave me the strength to pursue my dreams and believe in my potential. I also thank my brother, Arthur, whose humor and companionship have brought joy and resilience to my days, and my sister, Isabele, for her constant support through both the good and challenging moments.

I would like to express my gratitude to my friends and colleagues Pedro Mota, Daniel Santiago, Danilo de Brito, Gabriel Sabino, Rafael Coelho, João Emanuel Firmino, Mauro Maciel, Luis Vasconcellos, Estevan Rezende, Lucas Meira, Thiago Assis, and Thiago Santiago. Thank you for your friendship, patience, and companionship throughout these formative years. I will always treasure the memories we shared during both the highs and lows of our academic journey.

To the professors who have made the public university a space for critical thinking, inclusivity, and intellectual exchange—thank you. In particular, I acknowledge Professor Dr. Aristeu Silveira Neto, whose dedication to teaching and passion for knowledge have left a lasting impression. I am also thankful to Eng. Dr. Ricardo Serfaty for his invaluable insights into the industrial field.

I extend my sincere thanks to the entire technical staff of the Fluid Mechanics Laboratory (MFLab) for their tireless commitment, which made this work possible. I also gratefully acknowledge the financial and technical support provided by Petróleo Brasileiro S.A. (Petrobras), the National Council for Scientific and Technological Development (CNPq), the Minas Gerais Research Support Foundation (FAPEMIG), and the Coordination for the Improvement of Higher Education Personnel (CAPES).

Lastly, I thank God for guiding me, opening doors, and blessing me with the strength and opportunities that made these achievements possible.

NONAKA, I. T. **Modeling and Simulation of Multicomponent Evaporative Sprays in Generic Conditions.** 2025. 144f. Master's Dissertation, Federal University of Uberlândia, Uberlândia/MG, Brazil.

ABSTRACT

This dissertation presents the development and analysis of a multicomponent droplet evaporation model within a Discrete Particle Method (DPM) framework for turbulent flows. The model incorporates key physical phenomena, including differential diffusion, radiation heat transfer, mass source terms in the PISO algorithm, and coupling with external thermodynamic property databases. A multicomponent formulation was implemented and validated through single droplet evaporation tests, showing good agreement with experimental data and literature references.

The numerical methodology was also extended to spray simulations in industrial cases, enabling detailed analysis of evaporation dynamics under complex conditions. The results highlight the importance of accurate transport models and thermal boundary treatments for capturing phase-change behavior in multicomponent systems.

The results demonstrate that the developed numerical and computational tools enable MFSim to simulate multicomponent droplet evaporation and condensation under general conditions with high efficiency. The framework supports large numbers of Lagrangian parcels while maintaining low computational cost, making it suitable for practical engineering applications involving complex spray dynamics.

These developments are essential for advancing the predictive capabilities of CFD tools applied to fuel sprays, heat exchangers, and other engineering systems involving multiphase and multicomponent transport phenomena.

Keywords: Differential diffusion, sprays, multicomponent.

NONAKA, I. T. **Modelagem e Simulação da Evaporação de Sprays Multicomponentes em Condições Genéricas.** 2025. 144f Dissertação de Mestrado, Universidade Federal de Uberlândia, Uberlândia/MG, Brasil.

RESUMO

Esta dissertação apresenta o desenvolvimento e a análise de um modelo de evaporação de gotas multicomponentes dentro de um framework baseado no Método de Partículas Discretas (DPM) aplicado a escoamentos turbulentos. O modelo incorpora fenômenos físicos relevantes, incluindo difusão diferencial, transferência de calor por radiação, termos-fonte de massa na equação de pressão do algoritmo PISO e o acoplamento com bancos de dados externos de propriedades termodinâmicas. A formulação multicomponente foi implementada e validada por meio de testes de evaporação de gotas isoladas, apresentando boa concordância com dados experimentais e referências da literatura.

A metodologia numérica também foi estendida para simulações de sprays em casos industriais, permitindo uma análise detalhada da dinâmica de evaporação sob condições complexas. Os resultados evidenciam a importância da modelagem precisa dos mecanismos de transporte e do tratamento das condições térmicas de contorno para a representação adequada da mudança de fase em sistemas multicomponentes.

Os resultados demonstram que as ferramentas numéricas e computacionais desenvolvidas permitem ao MFSim simular com eficiência a evaporação e condensação de gotas multicomponentes em condições gerais. A estrutura do modelo suporta um grande número de partículas Lagrangianas mantendo baixo custo computacional, o que o torna adequado para aplicações práticas em engenharia envolvendo dinâmicas complexas de sprays.

Esses desenvolvimentos são fundamentais para aprimorar a capacidade preditiva de ferramentas de CFD aplicadas a sprays combustíveis, trocadores de calor e outros sistemas de engenharia que envolvem fenômenos de transporte multifásicos e multicomponentes.

Palavras-chave: Difusão diferencial, sprays, multicomponente.

List of Figures

List of Tables

List of Symbols

Symbol	Unit	Description
u_t	m/s	Turbulent flame speed
u_L	m/s	Laminar flame speed
Φ	–	Equivalence ratio
Φ_{geom}	–	Geometric factor in dipole–dipole interaction
T	K	Temperature
P	Pa	Pressure
μ	Pa·s	Dynamic viscosity
μ_i, μ_j	C·m	Dipole moments of molecules i and j
D_1, D_2	m^2/s	Binary diffusion coefficients
W_1, W_2	kg/mol	Molecular weight
r_{ij}	m	Distance between molecules i and j
ϵ_{ij}	J	Depth of potential well (Lennard-Jones/Stockmayer)
σ_{ij}	m	Collision diameter
θ_i, θ_j, ϕ	rad	Angles defining dipole orientation
$f(\mathbf{r}, \mathbf{p}, t)$	–	Velocity distribution function (Boltzmann)
$f^{(N)}$, $f^{(h)}$, $f^{(1)}$	–	Reduced distribution functions
$Q(f, f)$	–	Collision operator
$\hat{f}_i^{[r]}$	–	r^{th}-order correction in Chapman–Enskog expansion
ξ	–	Perturbation parameter
n_i	m^{-3}	Number density of species i
m_i	kg	Molecular mass
k_B	J/K	Boltzmann constant
$\mathbf{v}_0$	m/s	Mass-average velocity

Symbol	Unit	Description
$\mathbf{v}_i$	m/s	Molecular velocity
ϕ_i	–	Correction function in Chapman–Enskog theory
$\mathbf{q}_i^{(1)}$	W/m^2	First-order heat flux
λ_i	W/(m·K)	Thermal conductivity of species i
W_i	–	Reduced peculiar velocity
A_i	–	Polynomial coefficient in Sonine expansion
$\Omega_{ij}^{(l,s)}$	–	Collision integral for species i and j
X_i, X_1, X_2	–	Mole fraction of species i, or components 1/2
X_k	–	Mole fraction of condensed species k
X_j	–	Mole fraction of gas-phase species j
P, P_k, P_i, P_i^*	Pa	Total pressure, partial pressure, and vapor pressure of species i
σ_i, σ_j, σ_{ij}	m	Lennard-Jones collision diameter
ε_i, ε_j, ε_{ij}	J	Lennard-Jones potential well depth
$\mu_i^{(\mathrm{liq})}$, $\mu_i^{(\mathrm{vap})}$	J/mol	Chemical potential of species i in liquid/vapor phase
G°_{vap}, G°_{liq}	J/mol	Standard Gibbs free energy of vapor/liquid
ΔG°	J/mol	Change in Gibbs free energy for phase transition
γ_1, γ_2	–	Activity coefficients of components 1 and 2
G^E	J/mol	Excess Gibbs free energy
n_1, n_2	mol	Number of moles of components 1 and 2
R	J/(mol·K)	Universal gas constant
K_k	Pa	Henry's law constant for species k
p_k	Pa	Partial pressure of species k
pH	–	Logarithmic measure of hydrogen ion concentration

Symbol	**Unit**	**Description**
Y_k	–	Mass fraction of condensed species k
Y_j	–	Mass fraction of gas-phase species j
Y_i	–	Mass fraction of species i
Le	–	Lewis number
D_c	m^2/s	Characteristic mass diffusivity
c_p	J/(kg·K)	Specific heat at constant pressure
μ_k	Pa·s	Viscosity of species k
μ	Pa·s	Viscosity of the mixture
σ_k, σ_{va}	m	Lennard-Jones collision diameter
$\Omega_{kk}^{(2,2)\star}$, Ω_D	–	Collision integral (depends on reduced temperature)
Φ_{kj}	–	Interaction function for mixture viscosity
λ_k	W/(m·K)	Thermal conductivity of species k
λ	W/(m·K)	Thermal conductivity of the mixture
D_{km}^*	m^2/s	Mixture-averaged diffusivity (molar flux, mole fraction gradient)
D_{km}	m^2/s	Mixture-averaged diffusivity (mass flux, mass fraction gradient)
D'_{km}	m^2/s	Mixture-averaged diffusivity (mass flux, mole fraction gradient)
J_k^*	mol/(m^2·s)	Molar diffusion flux of species k
j_k	kg/(m^2·s)	Mass diffusion flux of species k
$\widetilde{V}_k$	m/s	Molar-average velocity of species k
M_{va}	kg/mol	Reduced molar mass between vapor and gas
δ_{va}	m	Effective collision diameter for vapor–gas interaction
$T^\star$	–	Reduced temperature for diffusion integral
χ_{g_m}	–	Molar fraction of total gas phase mixture

Symbol	**Unit**	**Description**
χ_{v,k_m}	–	Molar fraction of vapor species k
a_{00}^1, a_{10}^1, a_{01}^1	–	Chapman–Enskog expansion coefficients
$L^{ab,cd}$	–	Submatrices of the Chapman–Enskog L matrix
$\lambda_{0,\text{trans}}$	W/(m·K)	Translational thermal conductivity
$\lambda_{0,\text{int}}$	W/(m·K)	Internal thermal conductivity
λ_0	W/(m·K)	Total thermal conductivity
D_{jk}	m^2/s	Multicomponent diffusion coefficient
P_{jk}, P_{jj}	–	Chapman–Enskog polynomial coefficients
T_d	K	Droplet temperature
T_g	K	Gas temperature
R_d	m	Droplet radius
D_{AB}	m^2/s	Binary diffusion coefficient between species A and B
k_l, k_g	W/(m·K)	Thermal conductivity of the liquid and gas phases
h	$\text{W}/(\text{m}^2\cdot\text{K})$	Heat transfer coefficient
Nu	–	Nusselt number
Sh	–	Sherwood number
Re	–	Reynolds number
Sc	–	Schmidt number
Pr	–	Prandtl number
B_T, B_M	–	Spalding thermal and mass transfer numbers
h_v	J/kg	Latent heat of vaporization
m_d	kg	Droplet mass
$\dot{m}_d$	kg/s	Droplet evaporation rate
ρ_d, ρ_g	kg/m^3	Density of droplet and gas
$c_{p,d}$, $c_{p,g}$	J/(kg·K)	Specific heat of droplet and gas

Symbol	Unit	Description
$\mathbf{v}_d$, $\mathbf{v}_g$	m/s	Velocity of droplet and gas
τ_d	s	Droplet response time
D_t	m^2/s	Turbulent diffusion coefficient
$\widetilde{Y}_k$	–	Favre-averaged mass fraction of species k
$\widetilde{T}$	K	Favre-averaged temperature
$\widetilde{u}_i$	m/s	Favre-averaged velocity component
u_i'	m/s	Fluctuating component of velocity
S_{ij}	1/s	Mean strain rate tensor
ε	$\mathrm{m}^2/\mathrm{s}^3$	Dissipation rate of turbulent kinetic energy
k	$\mathrm{m}^2/\mathrm{s}^2$	Turbulent kinetic energy
ρ_l	kg/m^3	Liquid density
$c_{p,l}$	J/(kg·K)	Specific heat of liquid phase
τ_h	s	Heat-up time of droplet
$\dot{T}_d$	K/s	Time derivative of droplet temperature
$\dot{m}_k$	kg/s	Evaporation rate of species k from the droplet
x_p, y_p, z_p	m	Particle position coordinates
x_0, y_0, z_0	m	Origin coordinates of the domain
Δx, Δy, Δz	m	Eulerian cell size in each direction
i_c, j_c, k_c	–	Index of the Eulerian cell where the particle is located
F_M	–	Correction factor for mass transfer (Abramzon–Sirignano model)
F_T	–	Correction factor for heat transfer (Abramzon–Sirignano model)
N_k	$\mathrm{mol}/(\mathrm{m}^2\cdot\mathrm{s})$	Molar flux of species k (Maxwell–Stefan formulation)
$\mathbf{J}_k$	$\mathrm{mol}/(\mathrm{m}^2\cdot\mathrm{s})$	Diffusive molar flux vector of species k

Symbol	**Unit**	**Description**
∇X_k	1/m	Gradient of mole fraction of species k
T_s	K	Temperature at the droplet surface
T_g	K	Temperature of the surrounding gas far from the droplet
$Y_{v,s}$	–	Mass fraction of vapor at the droplet surface
$Y_{v,g}$	–	Mass fraction of vapor in the far-field gas

Contents

1 Introduction

1.1 Motivation and Objective

Spray systems are extensively employed in engineering applications due to their ability to transport substances across different phases in a controlled and efficient manner. According to Lefebvre and McDonell [45], sprays are utilized in a wide range of fields, including combustion systems, process industries, agriculture, medicine and meteorology. A variety of spray devices have been developed for these purposes, commonly referred to as atomizers or nozzles.

Over the past decade, interest in the science and technology of atomization has grown significantly, evolving into a major international and interdisciplinary research field. This heightened focus has been accompanied by significant advancements in laser diagnostics for spray analysis and the development of numerous mathematical models for spray combustion processes. As a result, it has become increasingly crucial for engineers to deepen their understanding of the fundamental evaporation processes and to be well-versed in the capabilities and limitations of various atomization devices.

Specifically, engineers must be able to identify the most suitable atomizer by understanding the spray behavior for a given application. This is essential because operating conditions affect flow properties, particle size and velocity, and the range reached by the liquid phase. All of these aspects influence the performance of the atomizer.

Computational Fluid Dynamics (CFD) is one of the most widely used technologies for improving the performance of aerodynamic systems [4]. Its ability to accurately predict fluid behavior in diverse and complex scenarios allows for the optimization of engineering designs without the need for extensive experimental testing. However, as noted by Silveira Neto [54], CFD simulations often entail a high computational cost, which is directly related to the desired level of detail and complexity. Consequently, numerous models and numerical strategies have been developed to reduce computational expenses while preserving acceptable levels of accuracy.

Given the high computational cost associated with CFD methods, this study adopts and improves MFSim, an in-house code designed for multiphase flow simulations. The objective is to enhance its capability to simulate droplet evaporation and condensation phenomena in multicomponent spray modeling. As highlighted by Wang [85], multicomponent evaporation models have a significant influence on spray kinetics and, consequently, on phase change modeling. In addition to improving the physical modeling of spray dynamics, this work also aims to increase the usability of MFSim by streamlining the configuration of boundary and initial conditions for end users.

1.2 Scope and Assumptions

One of the main focuses of this work is to investigate the Discrete Particle Method (DPM), an Euler–Lagrange approach within CFD used to analyze particle motion and its interaction with the surrounding flow, specifically the evaporation/condensation phenomena.

The fluid studied is Newtonian, and compressible flow is assumed throughout the simulations. Although the theoretical foundations are discussed, it is important to emphasize that evaporation behavior under high-pressure conditions (up to 2.0 MPa) was tested but not studied in detail, as it was not the focus of this research, including in the context of the industrial case presented later. The effects of elevated pressure are not trivial. One particular challenge lies in obtaining accurate thermophysical properties of pure substances in both liquid and gaseous phases. While real-gas properties at high pressure are relatively accessible, the liquid phase was treated as a pure substance, which introduces limitations.

A detailed analysis of droplet–droplet interactions, including particle and wall collisions (as described by Santos [21]), coalescence and breakup [61], oscillations such as instabilities during evaporation, and size distribution, is beyond the scope of this study. As a result, the coupling model adopted here does not account for the full complexity of a four-way interaction model, which will be discussed later. Moreover, neither particle–wall nor fluid–wall interactions are considered in this work.

Building upon the classification of Lagrangian evaporation heating models proposed by Sazhin [69], diffusion models can likewise be organized into hierarchical levels according to their complexity, as summarized in Table 2.

Table 2: Heating models and diffusion models categories

	Heating model	Diffusion model
1	Droplet surface temperature is uniform and does not change with time	Single component
2	No temperature gradient inside droplets (infinite thermal conductivity [ITC] of liquid)	Multicomponent droplet with no molar fraction gradient inside (ID)
3	Finite thermal conductivity (FTC), but not re-circulation inside droplets (conduction limit)	Finite diffusion (FD), but not re-circulation inside droplets (conduction limit)
4	Effective Thermal Conductivity (ETC) with finite liquid thermal conductivity and re-circulation inside droplets via the introduction of a correction factor to the liquid thermal conductivity	Effective Diffusion (ED) with finite components diffusion and re-circulation inside droplets via the introduction of a correction factor to the mass fraction
5	Re-circulation inside droplets in terms of vortex dynamics (vortex models)	
6	Full solution to the Navier-Stokes equation	

Table 2 presents both heating and diffusion models, arranged from the simplest to the most detailed formulations. In the present study, models corresponding to levels 3 and 4 were adopted, as they offer a suitable balance between physical accuracy and computational efficiency.

The model adopted in this research for spray simulations is based on the Euler–Lagrange framework. As highlighted by Wörner [91], the Discrete Phase Model (DPM) offers several advantages, particularly with respect to computational efficiency, since it assumes perfectly spherical particles. For validation, particles of different sizes were studied, following the experimental data used for comparison.

To analyse different particle shapes, alternative methods such as the Volume-of-Fluid (VOF) approach [64] are available; however, they are significantly more computationally expensive for spray applications, because they require a considerable increase in mesh refinement. Nevertheless, in specific scenarios that demand a more detailed description of interface dynamics or complex rheological behavior, such as non-Newtonian droplets, VOF-based models may be more suitable. For example, Vasconcellos [22] employed a

VOF approach to simulate the free fall of a single non-Newtonian droplet.

1.3 Topics

To distinguish the contributions developed by the author from methodologies previously implemented, this work is organized into the following chapters. Chapter 2 to 5 presents the fundamental physics related to evaporation, providing the theoretical background necessary to interpret the simulation results. Chapter 6 reviews the literature and summarizes previous developments associated with MFSim. In order to maintain the document concise, some implementations by other authors are not discussed in detail but are properly acknowledged and referenced where appropriate. Chapter 1.4.1.1 describes the data structure and some internal developments of the code; however, these are not the central focus of the dissertation. Chapter 7 introduces the methodologies and improvements implemented during this research, along with selected results. Finally, the main findings are presented and discussed in Results 8, followed by conclusions and suggestions for future improvements, as identified by the author to further enhance the simulation framework.

1.4 Softwares

This section presents the main software tools employed in this research. A brief overview is provided to ensure that the reader has the necessary background to understand the simulations and interpret the results.

1.4.1 MFSim

MFSim is an in-house CFD software that employs a structured block mesh combined with dynamic adaptive mesh refinement to perform fluid mechanics simulations. The software was originally developed by Villar [84], who highlighted three key advantages of this approach: the ability to simulate multiphase flows, the use of adaptive mesh refinement

for enhanced resolution where needed, and reduced computational cost in solving complex flow regimes.

The Front-Tracking and Structured-Block Adaptive Mesh framework described by Nourgaliev [56] offers an efficient and robust approach to CFD simulations. In this structure, the Lagrangian and Eulerian components of the flow are distributed across different processors, enabling parallelization and improving performance. As a result, the method provides fast, high-fidelity simulations while maintaining clarity and ease of interpretation.

Several other advantages of MFSim are presented in the literature; however, they are beyond the scope of this document. For a more comprehensive description, the reader is referred to the Ph.D. thesis of Villar [84]. Subsequent developments were carried out by graduate students at the Federal University of Uberlândia (UFU), who further enhanced the software as part of their research in the Laboratory of Fluid Mechanics (MFLab).

1.4.1.1 Lagrangian Data Structure Guarato [21] explains the memory management methodology used by MFSim to handle Discrete Particle Model (DPM) simulations. Since MFSim runs in parallel using Message Passing Interface (MPI), and because of the dynamic nature of sprays with particles continuously being added and removed, a robust memory management system is required. One efficient solution implemented is a *hash map*, similar to the hash table concept described by Cormen et al. [16].

Each Lagrangian particle is associated with an Eulerian mesh cell, and the hash map structure allows indexing using the cell identifier and the particle's unique ID. This enables contiguous memory storage and fast access, even under dynamic remeshing operations.

The cell index of a particle is computed based on its position as:

$$i_c = \text{int}\left(\frac{x_p - x_0}{\Delta x}\right), \quad j_c = \text{int}\left(\frac{y_p - y_0}{\Delta y}\right) \quad \text{e} \quad k_c = \text{int}\left(\frac{z_p - z_0}{\Delta z}\right), \tag{1}$$

where x_0, y_0, and z_0 are the domain origin coordinates, and Δx, Δy, and Δz depend on the refinement level of the Eulerian mesh. Figure 1 illustrates a schematic of this multilevel data structure.

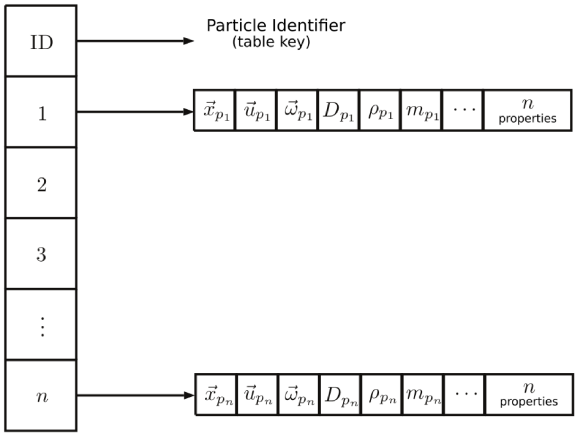

Figure 1: Sketch of lagrangian map hash composed by levels of refinement. Adapted from Guarato [21].

The hash map is indexed by the particle's unique identifier, which acts as the key to access all of its properties (position, velocity, diameter, density, mass, etc.). This enables managing millions of particles without scanning the entire data structure. Figure 2 depicts this hash structure.

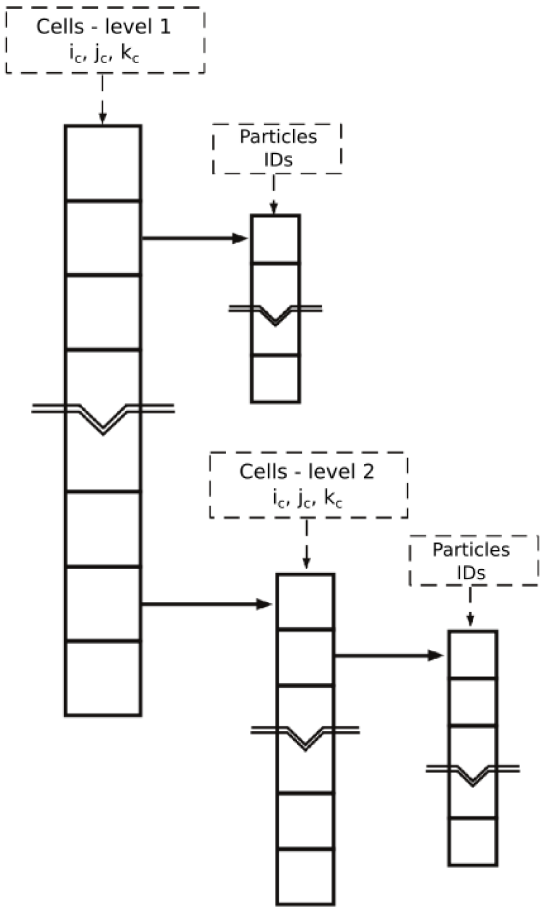

Figure 2: Sketch of hash map that allocates the computational particles. Adapted from Guarato [21].

The implementation in MFSim uses the `UTHASH` library [18], developed in C. As a result, most of the DPM module (`dpm.c`) is also written in C. `UTHASH` offers macros such as `HASH_ADD_INT`, `HASH_FIND_INT`, and `HASH_DEL` to create, query, and modify the hash tables. Each particle is encapsulated in a `struct dpm_particle_t` containing its physical properties.

MFSim uses MPI for parallelization. Each process (or *rank*) maintains a local hash table with its set of particles. When particles move across subdomain boundaries, they are removed from the current process using `HASH_DEL` and sent to the appropriate neighboring process using MPI send/receive calls. The receiving process then inserts the particle with `HASH_ADD_INT`, assigning a new local ID.

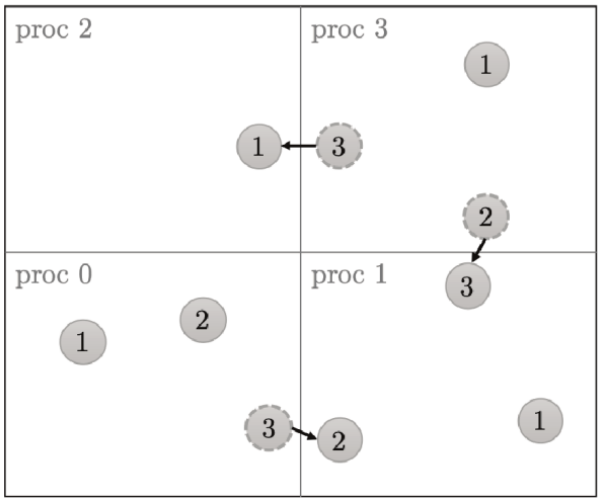

Figure 3: Sketch of particles transferring between processes. Adapted from Guarato [21].

Each particle has a unique ID known only to its local process. When transferred, its ID and data are removed from the local table and a new ID is assigned on the receiving end. MPI communications are handled in C, but Eulerian transport equations are discretized in Fortran, requiring careful interfacing between both languages.

This hybrid model allows for efficient redistribution of the domain and real-time exchange of particles with minimal computational overhead. Data consistency is ensured through collective and point-to-point communication strategies provided by MPI.

1.4.2 Cantera

Cantera [32] is an open-source software suite designed for modeling and simulation in the applied sciences, particularly in fields such as chemistry, process engineering, thermodynamics, and computational fluid dynamics (CFD). Originally developed in C++, Cantera offers interfaces for Python, Fortran, MATLAB, and Julia, making it highly accessible and easily integrable with a wide range of simulation environments.

Cantera is particularly well-suited for simulating chemical reactions, heat and mass transfer, chemical equilibrium, and the thermodynamic properties of pure substances. It is widely used in combustion modeling, multiphase reaction systems involving real and ideal gas simulations, and industrial chemical reactor design.

The main advantages of using Cantera are summarized below:

- **Chemical Reaction Simulation:** Capable of modeling both isothermal and non-isothermal reactions, Cantera tracks the evolution of chemical compositions over time.
- **Chemical Equilibrium:** It computes the equilibrium states of systems composed of multiple phases and components, allowing for accurate prediction of final reactive states.
- **Thermodynamic Properties:** Cantera evaluates essential thermodynamic properties such as enthalpy, entropy, and internal energy across a wide range of temperatures and pressures.
- **Chemical Kinetics:** The software includes a comprehensive library of kinetic models for simulating complex chemical reactions, including those involved in combustion and gasification.
- **Fluid Flow Simulations:** Through its interfaces, Cantera can be coupled with fluid dynamics solvers to model reactive flows involving gas, liquid, and solid phases.
- **Integration with Other Platforms:** Its compatibility with external simulation tools, including CFD and process simulation software, enhances its versatility in tackling multifaceted engineering problems.

Cantera is a sponsored project of NumFOCUS, a nonprofit organization based in the United States. NumFOCUS provides fiscal, legal, and administrative support to ensure the long-term sustainability and continued development of the Cantera project.

2 Molecular and Thermodynamic Principles

This section introduces the fundamental principles of chemical kinetics and molecular transport, which serve as the foundation for understanding diffusion processes in multi-component flows. These concepts are essential for analyzing the evaporation dynamics at the droplet surface, where molecular motion governs both mass and heat transfer mechanisms.

2.1 Chemical Kinetics and Diffusion

As stated by Atkins [6], liquid droplets tend to adopt a spherical shape due to the intrinsic tendency of liquids to minimize their surface area. Because a sphere has the lowest surface-to-volume ratio, the Discrete Particle Method (DPM) assumption of spherical particles is often a good approximation. However, as particle size increases, this assumption becomes less valid. In addition, when droplets are in motion, deviations from the spherical shape can be amplified, leading to breakup phenomena. Therefore, for cases involving larger droplets, the DPM becomes less appropriate, and alternative methods such as those mentioned above should be employed.

Diffusive processes are ubiquitous in natural and engineered systems, occurring primarily in two forms: mass diffusion and thermal diffusion. The diffusion rate can vary depending on several factors, including temperature, pressure, advection intensity, and the magnitude of concentration gradients.

Kuznetsov [42] investigates premixed reactants in turbulent flows, focusing on the discrepancy between the maximum turbulent and laminar burning velocities (u_t and u_L, respectively). These maxima occur at different equivalence ratios depending on the fuel. For example, in mixtures of H_2 and CH_4, the maximum u_t is observed at $\Phi = 1.0$ for H_2 and at $\Phi = 1.4$ for benzene, whereas the maximum u_L occurs at $\Phi = 1.7$ for H_2 and $\Phi = 1.0$ for benzene.

These observations support the conclusion that preferential diffusion plays a critical

role in turbulent combustion, particularly in premixed flames where lighter species, such as hydrogen, diffuse more rapidly than heavier ones. Kuznetsov's analysis of experimental data demonstrates that the peak turbulent and laminar flame speeds occur at distinct equivalence ratios, and that this shift correlates with the ratio of molecular diffusivities between fuel and oxidizer. As emphasized by Kuo [41], the coupling of molecular transport phenomena with chemical kinetics is essential for accurate combustion modeling, especially in multiphase systems. Accurate modeling of spray heating and evaporation is essential for understanding diffusive and thermal transport phenomena, as these processes critically influence droplet lifetime, flame structure, and overall combustion performance.

The molecular velocity in a multicomponent flow can be estimated using the Maxwell–Boltzmann velocity distribution, as explained by Atkins [7]. This statistical model shows that, at a given temperature, lighter molecules possess higher average velocities than heavier ones.

These molecular motions collectively define the internal energy of a substance, influencing macroscopic properties such as temperature (T), pressure (P), and viscosity (μ). As diffusion arises from the random motion of molecules, it is inherently governed by this internal energy. In multicomponent systems, coupling between mass and heat transfer leads to cross-diffusion phenomena, which are particularly relevant in reactive or highly non-uniform flows. Among these, the Soret effect refers to mass fluxes induced by temperature gradients (thermal diffusion), while the Dufour effect corresponds to heat fluxes driven by concentration gradients.

Mass diffusion, in its classical form, describes the transport of species due to concentration gradients. According to Graham's Law [49], the relative diffusion rates of two gases are inversely proportional to the square root of their molecular weights:

$$\frac{D_1}{D_2} = \sqrt{\frac{W_2}{W_1}} \tag{2}$$

where D_1 and D_2 are the diffusion coefficients of species 1 and 2, respectively, W_1 and W_2 are the corresponding molecular weights (molar masses).

Thermal diffusion refers to the transport of energy due to a temperature gradient, primarily through molecular collisions. As molecules undergo elastic collisions, kinetic energy is exchanged, resulting in heat transfer from hotter to cooler regions. This process, governed by Fourier's law, continues until thermal equilibrium is reached, characterized by a Maxwell–Boltzmann distribution of molecular velocities.

In multicomponent systems, however, temperature gradients can also induce mass fluxes, a phenomenon known as the Soret effect (or thermal diffusion in the strict sense). In such cases, lighter or more mobile species tend to migrate differently compared to heavier ones under thermal gradients, even when concentration gradients are absent. This cross-diffusion effect plays a significant role in systems such as evaporating sprays and reacting flows, where temperature fields are highly non-uniform.

If the energy transferred during molecular collisions exceeds a critical threshold, it may break existing chemical bonds or form new ones, initiating a chemical reaction. This minimum required energy is known as the activation energy. However, the detailed mechanisms of chemical reactions are beyond the scope of this document.

Differential diffusion can also be understood through the Boltzmann velocity distribution [7]. At room temperature (25°C), hydrogen molecules exhibit the highest average velocity among common gases due to their low molecular mass. This high velocity arises from translational and rotational motion, and at higher temperatures, vibrational modes also contribute. Consequently, hydrogen diffuses more rapidly than heavier molecules, which plays a significant role in the transport behavior of multicomponent mixtures. In contrast, large hydrocarbon molecules—with significantly higher molecular weights—exhibit much lower average velocities, leading to slower diffusion rates and stronger spatial segregation in mixture compositions.

2.2 Intermolecular Potentials

Intermolecular interactions between neutral molecules can be effectively modeled using the Lennard-Jones potential, which accounts for both short-range repulsion and long-range

van der Waals attractions. This potential function is widely employed in simulations of molecular systems due to its simplicity and ability to capture essential physical behavior. The Lennard-Jones potential $u_{ij}(r_{ij})$ is given by Equation 3, and the resulting potential energy curve is shown in Figure 4.

$$u_{ij}(r_{ij}) = 4\epsilon_{ij}\left[\left(\frac{\sigma_{ij}}{r_{ij}}\right)^{12} - \left(\frac{\sigma_{ij}}{r_{ij}}\right)^{6}\right]. \tag{3}$$

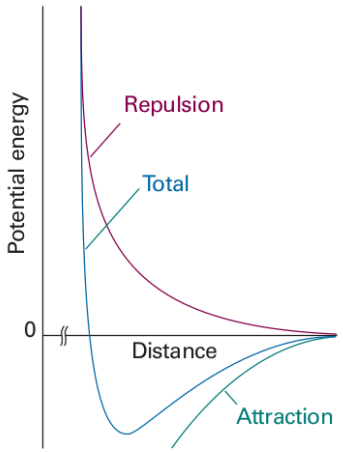

Figure 4: General form of an intermolecular potential energy curve. At large separations, the interaction is attractive due to van der Waals forces; at short distances, repulsion dominates. Source: Atkins [6].

In Equation 3, r_{ij} denotes the distance between the centers of mass of molecules i and j, ϵ_{ij} represents the depth of the potential well—indicating the strength of the intermolecular attraction—and σ_{ij} is the collision diameter, i.e., the distance at which the potential energy u_{ij} is zero.

Due to its balance between physical accuracy and computational efficiency, the Lennard-Jones potential is extensively used in modeling transport properties of gases and liquids, particularly in the context of molecular dynamics and kinetic theory applications.

To account for interactions between polar molecules, the Stockmayer potential extends the Lennard-Jones model by incorporating dipole–dipole interactions. The Stockmayer potential $u_{ij}(r_{ij}, \mu_i, \mu_j, \theta)$ is defined in Equation 4, and it includes an additional term that captures the influence of the relative orientation of molecular dipoles, as illustrated in

Figures 5 and 6.

$$u_{ij}(r_{ij}, \mu_i, \mu_j, \theta) = 4\epsilon_{ij} \left[\left(\frac{\sigma_{ij}}{r_{ij}} \right)^{12} - \left(\frac{\sigma_{ij}}{r_{ij}} \right)^{6} \right] - \frac{\mu_i \mu_j}{r_{ij}^3} \Phi_{\text{geom}}. \tag{4}$$

In this expression, μ_i and μ_j are the dipole moments of molecules i and j, respectively, and Φ_{geom} is a geometric factor given by:

$$\Phi_{\text{geom}} = 2\cos\theta_i \cos\theta_j - \sin\theta_i \sin\theta_j \cos\phi. \tag{5}$$

where θ_i, θ_j, and ϕ describe the orientations of the dipoles relative to the intermolecular axis.

The Stockmayer potential is particularly valuable for modeling polar systems, as it accounts for the long-range and orientation-dependent nature of dipole–dipole interactions. While the Lennard-Jones potential is adequate for non-polar molecules, the Stockmayer potential is indispensable when dealing with substances that exhibit permanent dipole moments.

However, both models share certain limitations. They assume pairwise additive interactions and neglect many-body effects, which can be significant in dense or strongly interacting systems. Furthermore, quantum mechanical effects are not explicitly included, which may limit their accuracy in systems containing light molecules or operating at cryogenic temperatures.

Despite these constraints, the combined use of Lennard-Jones and Stockmayer potentials remains a powerful and widely adopted approach for simulating intermolecular interactions across a broad range of physical and chemical applications.

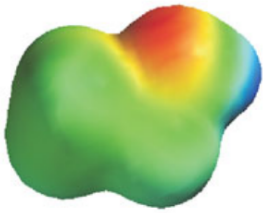

Figure 5: Electrostatic potential surface diagram of ethanol. Source: Atkins [6].

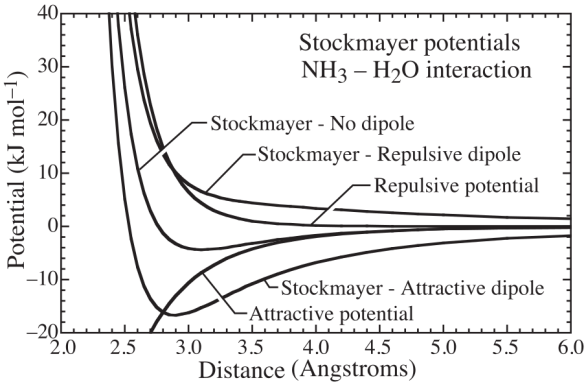

Figure 6: Stockmayer potential for the interaction between NH_3 and H_2O. Source: Kee [39].

2.3 Boltzmann Equation and Chapman–Enskog Theory

The Boltzmann equation governs the statistical behavior of a dilute gas by describing the time evolution of the velocity distribution function $f(\mathbf{r}, \mathbf{p}, t)$, which represents the probability of finding a molecule at position $\mathbf{r}$ with momentum $\mathbf{p}$ at time t. This equation inherently accounts for molecular transport due to temperature gradients, external forces, concentration gradients, and chemical reactions.

For a system of N molecules, the complete microscopic description is provided by the N-particle distribution function $f^{(N)}(\mathbf{r}^{(N)}, \mathbf{p}^{(N)}, t)$, which depends on $6N$ variables (three position and three momentum components per molecule). However, for macroscopic systems, where N is on the order of Avogadro's number, direct computation of $f^{(N)}$ is intractable. Instead, reduced distribution functions such as $f^{(h)}$, with $h \ll N$, are employed. These functions average over the remaining $N - h$ particles, yielding a more tractable yet useful statistical description.

Of particular importance is the single-particle distribution function $f^{(1)}(\mathbf{r}, \mathbf{p}, t)$, which suffices for evaluating most macroscopic properties of dilute gases. It provides the probability of finding any molecule at a given spatial location with a given momentum, regardless of the states of the other particles.

The Boltzmann equation is a nonlinear integro-differential equation for $f^{(1)}$. A key component of this equation is the *collision term*, often denoted by $Q(f, f)$, which accounts for the change in the distribution function due to binary molecular collisions. This term represents the net effect of molecules scattering into and out of a given velocity state.

Mathematically, the collision operator evaluates the balance between incoming and outgoing molecular velocities resulting from elastic collisions. It integrates over all possible collision angles and post-collision velocities, making it the most complex and computationally intensive part of the equation. Despite its difficulty, this term is what enables the Boltzmann equation to capture transport phenomena such as viscosity, thermal conductivity, and mass diffusion from first principles.

In practical applications, approximations to the collision term—such as the Bhatnagar-Gross-Krook (BGK) model or Enskog expansions—are employed to make the equation solvable while retaining key physical features. Further discussion on the formulation and approximations of the collision operator can be found in Kee et al. [39].

The Chapman–Enskog theory provides a rigorous method for deriving transport properties from the Boltzmann equation. In 1922, Enskog proposed a perturbative solution to the Boltzmann equation by expanding the velocity distribution function in powers of an ordering parameter ξ, later set to unity:

$$\hat{f}_i = \hat{f}_i^{[0]} + \xi \hat{f}_i^{[1]} + \xi^2 \hat{f}_i^{[2]} + \dots \tag{6}$$

Each term $\hat{f}_i^{[r]}$ represents the r^{th}-order correction to the equilibrium distribution $\hat{f}_i^{[0]}$. Retaining only the first-order correction yields expressions consistent with the Navier–Stokes equations. Including the second-order term leads to the Burnett equations, which are applicable to more rarefied gas.

The zeroth-order solution $\hat{f}_i^{[0]}$ corresponds to the local Maxwell–Boltzmann distribution, given by:

$$\hat{f}_i^{[0]} = n_i \left(\frac{m_i}{2\pi k_B T} \right)^{3/2} \exp\left(-\frac{m_i (\mathbf{v}_i - \mathbf{v}_0)^2}{2 k_B T} \right), \tag{7}$$

where n_i is the number density, m_i the molecular mass, k_B the Boltzmann constant, T the temperature, and $\mathbf{v}_0$ the mass-average velocity.

The first-order correction $\hat{f}_i^{[1]}$ is written as a product of the equilibrium distribution and an unknown function ϕ_i:

$$\hat{f}_i^{[1]} = \hat{f}_i^{[0]} \, \phi_i. \tag{8}$$

The function ϕ_i satisfies a linearized version of the Boltzmann equation, leading to an integro-differential equation involving collision integrals. Enskog solved this by expanding ϕ_i in a series of Sonine polynomials, which allowed the derivation of transport coefficients such as viscosity, thermal conductivity, and diffusion.

For example, the first-order heat flux can be written as:

$$\mathbf{q}_i^{(1)} = -\lambda_i \nabla T, \tag{9}$$

and comparing this expression to Fourier's law gives the expression for thermal conductivity:

$$\lambda_i = -\frac{2}{3} \frac{k_B^2 T}{m_i \nu_i} \int A_i(W_i) W_i^2 \left(W_i^2 - \frac{5}{2} \right) \hat{f}_i^{[0]} \, d\mathbf{v}_i, \tag{10}$$

where W_i is the reduced peculiar velocity and A_i is a function expanded in Sonine polynomials. Similar derivations apply for viscosity and diffusivity, and the final expressions depend on collision integrals $\Omega_{ij}^{(l,s)}$, which describe how intermolecular forces affect momentum and energy transport.

The Chapman–Enskog theory, despite its mathematical complexity, forms the backbone of rigorous transport property calculations in dilute gases. Detailed derivations and expressions are presented in Kee et al. [39].

Diffusion is a molecular-level phenomenon that plays a critical role in multicomponent transport. According to the Maxwell–Boltzmann velocity distribution [7], lighter molecules move faster on average than heavier ones at the same temperature, leading to differential diffusion effects in gas mixtures. These diffusive processes result from random molecular motion, which includes translational, rotational, and, at higher temperatures, vibrational components [98]. The internal energy associated with these motions governs macroscopic fluid properties such as temperature, pressure, and viscosity. Consequently, the diffusion rate is influenced by both molecular characteristics and thermodynamic conditions. As described by Graham's Law [49], the diffusion coefficient of a gas is inversely proportional to the square root of its molecular weight, reinforcing the observation that light species like hydrogen diffuse more rapidly than heavier ones. These effects are fundamental in modeling mass and energy transport in sprays, where differences in molecular mass among fuel components strongly affect evaporation dynamics and flame behavior.

3 Phase Equilibrium and Multiphase Systems

This section presents the fundamental thermodynamic principles governing phase equilibrium between liquid and vapor phases, with emphasis on gas–gas, liquid–liquid, and vapor–liquid interactions. These concepts are essential for understanding multicomponent evaporation, diffusion, and mass transfer in sprays and other multiphase systems.

3.1 Gas–Gas Interaction

As discussed by Poling et al. [57], multicomponent gas mixtures can often be approximated as ideal gases at low pressures. Under these conditions, intermolecular interactions are weak, and thermodynamic properties can be derived using simple models such as Dalton's law of partial pressures:

$$P = \sum_{i=1}^{N} X_i * P = \sum_{i=1}^{N} P_i. \tag{11}$$

where P is the total pressure of the gas mixture, X_i is the mole fraction of species i, and P_i is the partial pressure of species i.

At moderate to high pressures, however, deviations from ideality become significant due to molecular size and intermolecular forces. These deviations are typically handled through more sophisticated models, such as virial equations of state or cubic equations of state (e.g., Peng–Robinson, Soave–Redlich–Kwong), which include interaction parameters fitted to experimental data or estimated via corresponding-states correlations.

In gas–gas interactions relevant to evaporation, it is essential to consider how vaporized species diffuse through the surrounding gas mixture. The assumption of ideality implies that each species diffuses independently, but in reality, cross-interactions and molecular sizes alter the effective transport properties. Lennard–Jones parameters ε and σ are often used to describe these interactions, with the following combining rules used for binary mixtures:

$$\sigma_{ij} = \frac{\sigma_i + \sigma_j}{2}, \qquad \varepsilon_{ij} = \sqrt{\varepsilon_i \varepsilon_j}. \tag{12}$$

The variables σ_i, σ_j, ε_i, and ε_j are the Lennard–Jones parameters associated with species i and j, commonly used to characterize intermolecular interactions in gas mixtures:

- σ_i, σ_j: Effective molecular diameters of species i and j, respectively, typically given in angströms (Å) or nanometers (nm). These represent the distance at which the intermolecular potential between two molecules becomes zero, and are used as a measure of molecular size.
- ε_i, ε_j: Depths of the Lennard–Jones potential wells for species i and j, respectively. These values quantify the strength of the intermolecular attractive forces, and are often expressed in Kelvin (K) when used in conjunction with Boltzmann's constant k_B, or in energy units such as joules (J) or kilojoules per mole (kJ/mol).
- σ_{ij}: Effective collision diameter for interactions between species i and j, calculated as the arithmetic mean of their individual diameters.
- ε_{ij}: Effective energy of interaction for species i and j, given by the geometric mean of their individual energy parameters.

These combined Lennard–Jones parameters are used in kinetic theory models—such as Chapman–Enskog theory—to estimate transport properties in multicomponent gas mixtures, including binary diffusion coefficients, viscosity, and thermal conductivity.

In evaporation scenarios, the role of vapor pressure is particularly important. As stated by Yaws [95], the vapor pressure of a substance depends solely on temperature, and at equilibrium, the partial pressure of the vapor in the gas phase must equal the vapor pressure of the pure substance at that temperature. If the ambient gas initially contains no vapor, it will gradually become saturated through diffusion until equilibrium is reached.

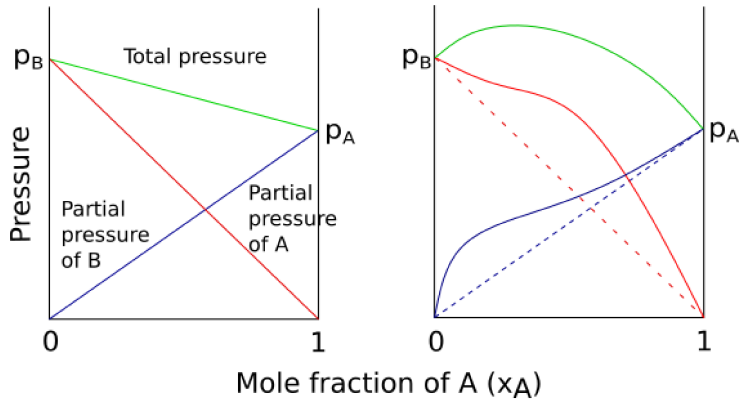

Figure 7: The ideal solution by Dalton's Law and the real comportment of pressure in real solution.

In multicomponent systems, accurate modeling of gas–gas interactions and diffusion behavior is essential for predicting evaporation rates and droplet lifetime. These effects become even more significant when considering non-ideal gas mixtures, high pressures, or multicomponent sprays with strong concentration gradients and species with different volatilities.

3.2 Liquid–Liquid Equilibrium (LLE)

Raoult's Law provides a foundational thermodynamic relationship for modeling phase equilibria in mixtures. It states that, in an ideal liquid solution, the partial vapor pressure of each component is directly proportional to its mole fraction in the liquid phase and the vapor pressure of the pure component at the same temperature:

$$P_k = X_k P_k^*, \tag{13}$$

where P_k is the partial pressure of component k, X_k is its mole fraction in the liquid, and P_k^* is the pure-component vapor pressure at the system temperature.

While Raoult's Law is accurate for ideal or nearly ideal solutions—typically involving chemically similar components—it fails for systems with significant differences in polarity or molecular structure. In such cases, non-ideal behavior arises, often resulting in liquid–liquid phase separation. This occurs when intermolecular interactions between unlike

molecules (e.g., between polar and non-polar species) are weaker than those between like molecules, causing partial miscibility or immiscibility in the liquid phase.

Liquid-liquid equilibrium (LLE) is a fundamental phenomenon in separation processes, phase behavior studies, and mixture thermodynamics. It refers to the equilibrium established between two immiscible or partially miscible liquid phases under given conditions of temperature and pressure. The nature and extent of phase separation depend strongly on molecular interactions, particularly those between polar and non-polar species.

Smith et al. [75] analyze the behavior of binary liquid–liquid systems under constant pressure, where pressure effects are assumed negligible. They classify solubility diagrams into three representative types, based on the degree of miscibility and the presence of critical solution temperatures, as illustrated in Figure 8.

These diagrams describe the temperature–composition dependence of phase separation in partially miscible liquid mixtures. The central region labeled "Two liquid phases" corresponds to conditions where the mixture separates into two distinct liquid phases with different compositions. Cases (a) and (b) exhibit a closed miscibility gap with an Upper Critical Solution Temperature (UCST), above which complete miscibility is observed. In contrast, case (c) illustrates a system with a Lower Critical Solution Temperature (LCST), below which the components are completely miscible.

In general, mixtures involving components with large differences in polarity—such as alcohols and hydrocarbons—tend to show limited mutual solubility and display UCST-type behavior. Understanding this phase separation behavior is essential for accurate modeling of liquid–liquid equilibrium (LLE), particularly in systems relevant to separation processes and spray-phase interactions.

Matsuda and Ochi [50] experimentally studied LLE for binary systems consisting of short-chain alcohols and long-chain n-alkanes, such as methanol + decane, ethanol + tetradecane, and ethanol + hexadecane. These systems exhibit limited miscibility at low temperatures and display UCST behavior, with mutual solubility increasing as temperature rises. The phase boundaries were determined using laser scattering techniques to

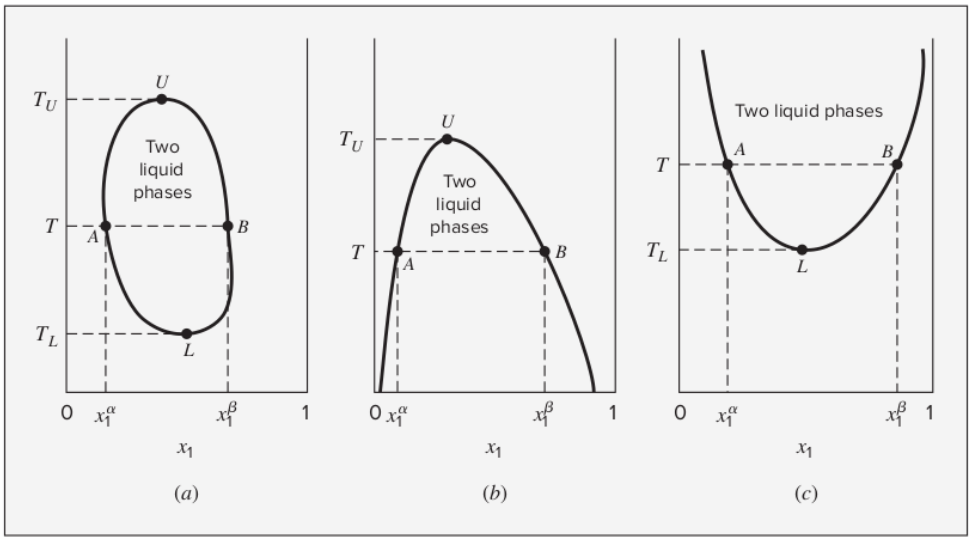

Figure 8: Three types of constant-pressure liquid/liquid solubility diagram. Source: Smith et al [75].

detect cloud points with high precision.

Their data were correlated using local composition models, including Non-Random Two-Liquid model (NRTL), Tsuboka–Katayama (a modified Wilson model), and the Complete Local Composition (CLC) model. These correlations not only reproduced the experimental LLE data accurately but also allowed prediction of vapor-liquid equilibrium (VLE) in partially miscible regions, demonstrating the consistency of such models across phase boundaries.

Understanding liquid-liquid interactions is critical for developing accurate thermodynamic models and for the reliable design of separation processes where immiscibility plays a key role.

3.3 Vapor–Liquid Equilibrium (VLE)

Vapor–liquid equilibrium (VLE) is the condition under which a liquid and its vapor coexist in equilibrium at a given temperature and pressure. According to Albright [3], phase equilibrium is achieved when both phases share the same temperature, pressure, and fugacity for each chemical species. Since fugacity is a measure of a species' chemical potential in a real mixture, the equilibrium condition can also be expressed as equality of chemical potentials between phases:

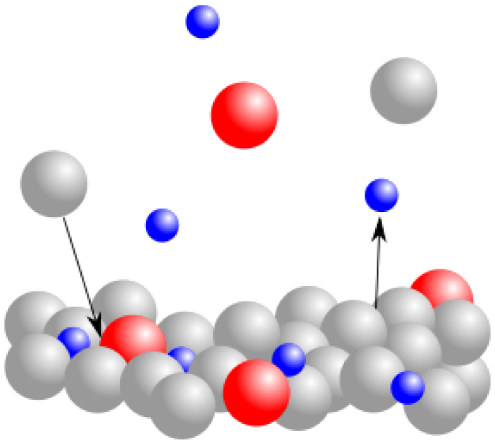

Figure 9: Gas-Liquid interaction representation.

$$\mu_i^{(\text{liquid})} = \mu_i^{(\text{vapor})}. \tag{14}$$

The vapor pressure of a substance at a given temperature is the pressure at which this equilibrium is satisfied for the pure component. From a thermodynamic perspective, this corresponds to the condition where the change in the standard Gibbs free energy G° for the phase transition is zero:

$$\Delta G^\circ = G^\circ_{\text{vap}} - G^\circ_{\text{liq}} = 0. \tag{15}$$

As described by Atkins [7], the Gibbs free energy determines the spontaneity of phase changes. When the free energy of the system is minimized, the system is in equilibrium. Thus, the vapor pressure emerges as the pressure at which a molecule has equal tendency to remain in the liquid phase or escape into the vapor phase.

Physically, equilibrium at the molecular level is reached when the rate of evaporation equals the rate of condensation. Molecules at the liquid surface gain sufficient kinetic energy—typically through collisions—to overcome intermolecular forces and escape into the gas phase. Simultaneously, vapor-phase molecules may lose energy and return to the liquid phase. When these two rates are balanced, the system reaches dynamic equilibrium.

Albright [3] also discusses binary systems, where two-component mixtures exhibit more complex vapor–liquid equilibrium (VLE) behavior. Figure 10 illustrates a typical

gas–liquid equilibrium surface for a binary mixture as a function of temperature (T), pressure (P), and mole fraction of component B (x_B). The dashed lines represent the vapor pressure curves of the pure components A and B, terminating at their respective critical points C_A and C_B. The solid lines connecting points A to B and C_A to C_B represent the phase boundaries and the critical locus of the mixture.

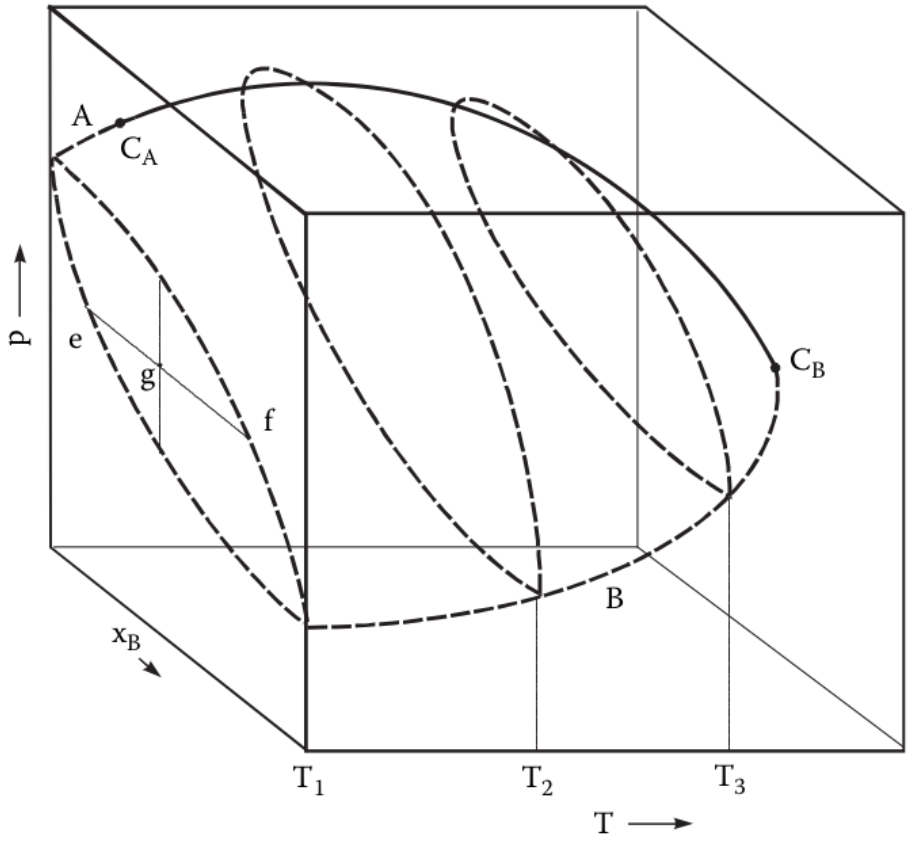

Figure 10: Gas-liquid equilibria of a binary system. Source: Albright [3].

Two-phase regions exist between the bubble-point surface (lower boundary) and the dew-point surface (upper boundary), which enclose the region where liquid and vapor phases coexist in equilibrium. The bubble-point surface corresponds to conditions at which the first bubble of vapor forms upon heating a liquid, while the dew-point surface indicates the conditions where the first droplet of liquid appears upon cooling a vapor mixture. The 3D representation provides a unified view of the system's phase behavior, encompassing the commonly used T–x, P–x, and P–T diagrams. Such visualization is fundamental for analyzing the dependence of VLE on composition, temperature, and

pressure—particularly in the context of multicomponent evaporation, where variations in volatility and critical properties play a key role.

In ideal systems, VLE can be described by the combined application of Dalton's and Raoult's laws. For example, at 298 K, the vapor pressure of pure water is approximately 3.141 kPa. In a dry air environment at atmospheric pressure (101.325 kPa), water will continue to evaporate until its partial pressure in the air reaches 3.141 kPa. According to Dalton's law, this corresponds to a water vapor mole fraction of:

$$X_{\mathrm{H_2O}} = \frac{P_{\mathrm{H_2O}}}{P_{\mathrm{total}}} = \frac{3.141}{101.325} \approx 0.031 \tag{16}$$

This illustrates the thermodynamic condition for saturation in an ideal gas mixture.

3.4 Non-Ideal VLE and Activity Coefficients

Poling et al [57] presents some models of Non-ideal (VLE), the non-ideal consideration considers the activity coefficient of each component. Poling et al [57] explains that thermodynamics does not give the experimental quantity desired but only relates it to other experimental quantities. The Gibbs-Duhem equation, as demonstrated by Denbigh [23] provides a useful tool for correlating and extending limited experimental data. In essence, the Gibbs-Duhem equation says that, in a mixture, the activity coefficients of the individual components are not independent of one another but are related by a differential equation.

For example, the estimation of accurate Henry's Law constants and activity coefficients for all components would introduce significant complexity and data requirements that are often impractical, especially for systems involving numerous species or limited experimental data. Therefore, Henry's Law with empirically determined coefficients—such approaches were not adopted in this work.

Although several non-ideal models, such as Van Laar, NRTL, and Wilson were studied, their implementation was not required in the present study. The numerical results closely

matched the experimental data, even without incorporating activity coefficient models. This indicates that, for the conditions analyzed, the assumption of ideality was sufficient to capture the essential phase behavior of the system. A detailed comparison between simulation and experimental results will be presented in a later section.

4 Diffusion Velocities

The accurate modeling of diffusion velocities in multicomponent mixtures is essential for describing mass transport phenomena in evaporation, combustion, and spray systems. In such contexts, the presence of strong gradients in species concentration, temperature, and pressure gives rise to complex diffusion behavior that cannot always be captured by simplified models. This section presents three commonly used formulations to describe diffusion velocities: Fick's Law, the Stefan–Maxwell equations, and the Hirschfelder–Curtiss approximation. Each model offers a different balance between physical accuracy and computational cost, and their respective assumptions, limitations, and applicability to multicomponent systems are discussed in the following subsections.

4.1 Fick's Law

Fick's Law describes mass diffusion as a flux proportional to the concentration gradient of a species in a mixture. It was first formulated by Adolf Fick in 1855 based on analogies with Fourier's law of heat conduction and Ohm's law for electrical conduction. The law can be expressed for a species k in a binary mixture as:

$$\mathbf{J}_k = -\rho D_k \nabla Y_k, \tag{17}$$

where $\mathbf{J}_k$ is the diffusive mass flux of species k, ρ is the mixture density, D_k is the mass diffusivity of species k in the mixture, and Y_k is the mass fraction of species k [8].

This equation is strictly valid for binary mixtures and under specific assumptions: (1) negligible pressure and temperature gradients, (2) no significant chemical reactions, and (3) constant diffusivity. For multicomponent systems, particularly those undergoing phase change or combustion, these assumptions may not hold. In such cases, models based on Fick's Law become inaccurate, especially when differential diffusion effects are significant [39, 41].

Physically, the diffusive flux represents the net movement of molecules from regions

of higher to lower concentration, driven by the random thermal motion of particles. The proportionality to the gradient reflects the statistical tendency of molecules to disperse over time, which is a consequence of the second law of thermodynamics [8].

In spray modeling, many simplified approaches are based on Fickian assumptions, either assuming constant diffusivity or neglecting cross-coupling between species. While this allows for computational efficiency, it can lead to inaccuracies in predicting evaporation rates and species profiles in the gas phase, particularly in multicomponent fuel systems [41].

4.2 Stefan-Maxwell Equations

The Stefan-Maxwell formulation of diffusion originates from the combination of Stefan's experimental work [78] and Maxwell's kinetic theory of gases [51]. This theory provides a rigorous basis for describing multicomponent mass diffusion, especially when differential diffusion, cross-coupling, or non-equimolar counterdiffusion is relevant [8, 39].

Coltrin et al. [39] explain that the diffusive mass fluxes J_k are expressed in terms of the diffusion velocities $\mathbf{V}_k$, which are determined implicitly from gradients of mole fraction, pressure, and temperature. The governing Stefan-Maxwell equation for a multicomponent mixture is:

$$\nabla X_k = \sum_{j=1}^{K} \frac{X_k X_j}{D_{kj}} (\mathbf{V}_j - \mathbf{V}_k) + (Y_k - X_k) \left(\frac{\nabla p}{p} \right) + \sum_{j=1}^{K} \frac{X_k X_j}{\rho D_{kj}} \left(\frac{D_j^T}{Y_j} - \frac{D_k^T}{Y_k} \right) \left(\frac{\nabla T}{T} \right), \quad (18)$$

where X_k is the mole fraction, Y_k is the mass fraction, D_{kj} is the binary diffusion coefficient, ρ is the mixture density, and D_k^T is the thermal diffusion coefficient of species k.

This formulation inherently satisfies mass conservation and provides greater fidelity than Fick's law, particularly in mixtures with large gradients or high non-ideality. Notably, the Stefan-Maxwell equations employ binary diffusion coefficients D_{kj}, avoiding the need to compute the full multicomponent diffusion matrix D_{ij} explicitly.

To solve Eq. 18, one must enforce the constraints:

$$\sum_{k=1}^{K} \rho Y_k \mathbf{V}_k = 0 \qquad \text{and} \qquad \sum_{k=1}^{K} \nabla X_k = 0. \tag{19}$$

These ensure that the mass fluxes are consistent and that the mole fractions remain normalized. A common numerical approach involves solving only $K - 1$ equations and computing the velocity of the remaining species via:

$$\mathbf{V}_k = \frac{1}{Y_k} \sum_{k=1}^{K-1} Y_k \mathbf{V}_k. \tag{20}$$

This technique reduces the linear system and satisfies the constraint identically. However, in systems without a dominant species, the choice of which species to exclude can significantly influence numerical accuracy [39, 41].

Despite its computational complexity, the Stefan-Maxwell formulation is favored in high-fidelity simulations of combustion, reacting flows, and evaporation phenomena involving multicomponent mixtures. It captures cross-diffusion effects, Soret diffusion (thermal diffusion), and barodiffusion (pressure-driven diffusion), which are critical in accurately modeling spray evaporation and fuel mixing.

4.3 Hirschfelder-Curtiss Approximation

In situations where Fick's law is insufficient to capture multicomponent diffusion behavior, an effective alternative is the Hirschfelder-Curtiss approximation. Originally proposed in the classical monograph by Hirschfelder, Curtiss, and Bird, and further discussed by Poinsot and Veynante [63], this method provides a simplified but physically grounded approach to modeling diffusion in multicomponent mixtures.

Rather than resolving the full Stefan-Maxwell system, which requires solving a coupled set of equations involving all species pairs, the Hirschfelder-Curtiss approximation reduces complexity by assuming that each species k diffuses independently into the rest of the mixture. This leads to a formulation where the diffusion velocity is given by:

$$\mathbf{V}_k X_k = -D_k \nabla X_k. \tag{21}$$

The effective diffusion coefficient D_k for species k is obtained by weighting the diffusivites of species k relative to all other species j, thereby determining the effective diffusivity of species k in the mixture:

$$D_k = \frac{1 - Y_k}{\sum_{j \neq k} \frac{X_j}{D_{kj}}}. \tag{22}$$

Here, D_{kj} is the binary diffusion coefficient between species k and j, X_j is the mole fraction, and Y_k is the mass fraction of species k. Unlike D_{kj}, the coefficient D_k is not a true binary diffusion coefficient, but rather an *effective diffusivity* of species k into the remainder of the mixture.

Substituting Eqs. 21 and 22 into the mass fraction transport equation yields:

$$\frac{\partial \rho Y_k}{\partial t} + \nabla \cdot (\rho \mathbf{u} Y_k) = \nabla \cdot \left(\rho D_k \frac{W_k}{W} \nabla X_k \right) + \dot{\omega}_k. \tag{23}$$

This formulation is especially advantageous in reactive flows where computational efficiency is critical. It preserves mass conservation and is frequently used in combustion modeling frameworks such as flamelet and spray evaporation simulations [63, 8].

Despite being an approximation, the Hirschfelder-Curtiss method offers a robust compromise between physical fidelity and computational simplicity. It captures the essential physics of multicomponent diffusion while avoiding the complexity of the full Stefan-Maxwell approach.

The choice of diffusion model plays a critical role in determining the accuracy of mass transport predictions, particularly in multicomponent systems subject to evaporation and combustion. While Fick's law provides a basic framework with low computational cost, more advanced formulations like the Stefan–Maxwell equations or the Hirschfelder–Curtiss approximation are required to capture cross-diffusion, thermodiffusion, and multicompo-

nent interactions. Each model offers a distinct trade-off between fidelity and efficiency. In the following section, these diffusion frameworks are connected to the broader class of transport models—implemented in tools such as Cantera and MFSim—which not only determine diffusivity but also incorporate thermal conductivity and viscosity calculations based on molecular and thermodynamic properties. This integration is essential for accurately modeling spray evaporation in complex multicomponent mixtures.

5 Transport Models in Multicomponent Mixtures

Building on the diffusion velocity formulations previously discussed, this section presents the transport models used to evaluate thermophysical properties—namely viscosity, thermal conductivity, and mass diffusivity—in multicomponent gas mixtures. These properties are essential for accurately modeling heat and mass transfer in spray evaporation, combustion, and reactive flows. The models implemented in software packages such as Cantera, as well as custom formulations like the Lennard-Jones, offer varying degrees of complexity and accuracy. Each model is built upon different assumptions regarding molecular interactions and mixture-averaging strategies, and their selection directly affects the predictive capability and computational cost of the simulation. The following subsections describe the theoretical basis and implementation of the Unity-Lewis, Mixture-Averaged, Lennard-Jones, and Multicomponent models.

5.1 Unity Lewis Model

The Lewis number (Le) is a dimensionless parameter that represents the ratio of thermal to mass diffusivity in a fluid. It is defined as

$$Le = \frac{\lambda}{\rho D_k c_p}, \tag{24}$$

where λ is the thermal conductivity, ρ is the density, D_k is the mass diffusivity of k species, and c_p is the specific heat at constant pressure. The Unity-Lewis model assumes $Le = 1$ for all species, implying that thermal and mass diffusivities are equal. This simplification is often employed to reduce computational cost in spray and flame simulations where differential diffusion effects are considered negligible.

In Cantera, both the Unity-Lewis and Mixture-Averaged models use the same approach to compute viscosity. The mixture viscosity μ is given by:

$$\mu = \frac{\sum_{k=1}^{K} X_k \mu_k}{\sum_{k=1}^{K} \sum_{j=1}^{K} X_j \Phi_{kj}}, \tag{25}$$

where μ_k is the viscosity of pure species k, calculated as:

$$\mu_k = \frac{5}{16} \frac{\sqrt{\pi m_k k_B T}}{\pi \sigma_k^2 \Omega_{kk}^{(2,2)\star}}, X * Y \tag{26}$$

and the interaction term Φ_{kj} is given by:

$$\Phi_{kj} = \frac{1}{\sqrt{8}} \left(1 + \frac{W_k}{W_j}\right)^{-1/2} \left[1 + \left(\frac{\mu_k}{\mu_j}\right)^{1/2} \left(\frac{W_j}{W_k}\right)^{1/4}\right]^2. \tag{27}$$

Here, σ_k is the Lennard-Jones collision diameter of species k, m_k is the molecular mass, k_B is the Boltzmann constant, and T is the temperature. The collision integral $\Omega_{kk}^{(2,2)\star}$ depends on the reduced temperature and dipole moment, as described in Kee [39].

Thermal conductivity is calculated using:

$$\lambda = \frac{1}{2} \left(\sum_{k=1}^{K} X_k \lambda_k + \frac{1}{\sum_{k=1}^{K} \frac{X_k}{\lambda_k}} \right), \tag{28}$$

where λ_k is the thermal conductivity of species k. The values of c_p are typically obtained from the NASA 7- or 9-coefficient polynomial parameterizations, as provided in Goodwin et al. [33].

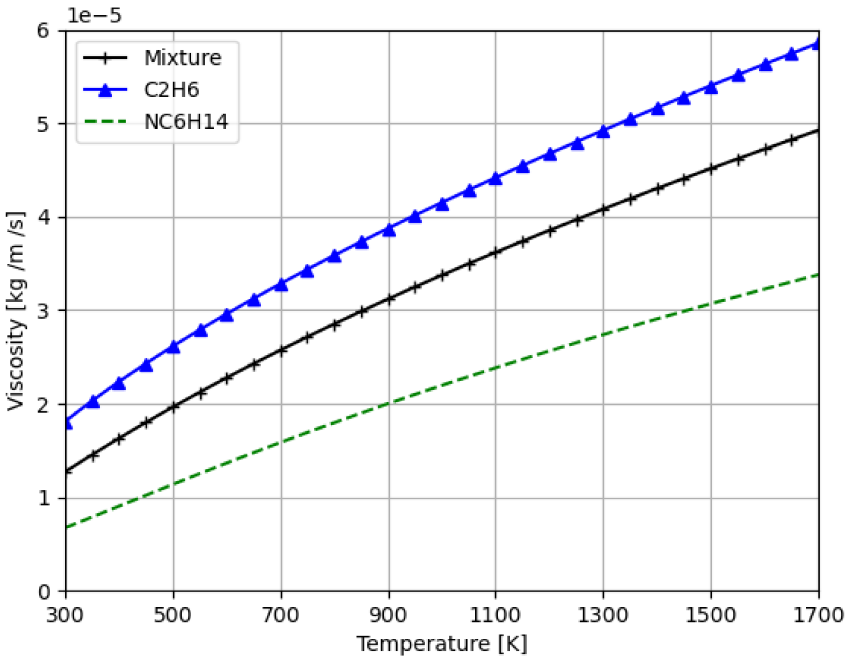

Figure 11: Species viscosities and resulting mixture viscosity computed by Cantera for a binary mixture of n-hexane and ethane.

Figure 11 illustrates the individual viscosities of n-hexane and ethane, as well as the resulting mixture viscosity calculated by Cantera. The model evaluates each species' viscosity based on molecular parameters and combines them using mixing rules to obtain the overall viscosity of the gas mixture.

This methodology for computing species and mixture viscosities is consistently applied across all transport models discussed in this section. While the Unity-Lewis model assumes a constant Lewis number ($Le = 1$) for simplicity—implying equal thermal and mass diffusivities—this assumption becomes inadequate in systems where differential diffusion is significant. For instance, Mukundakumar et al. [53] investigated the impact of non-unity Lewis numbers in hydrogen flame dynamics, demonstrating the need for more comprehensive transport models in such cases.

5.2 Mixture-Averaged Model

The Mixture-Averaged model is widely used in reacting flow simulations due to its balance between computational efficiency and accuracy. Kee et al. [39] describe this approach based on the concept of binary diffusion, where each species diffuses relative to a mixture-averaged background. The diffusion coefficient for each species is computed from pairwise binary diffusion coefficients and species mole or mass fractions.

Viscosity in this model is evaluated using a semi-empirical formulation originally proposed by Wilke [87] and later refined by Bird et al. [8]. Thermal conductivity is also computed analogously, using mixture rules similar to those applied for viscosity. The key difference between the Unity-Lewis and Mixture-Averaged models lies in the treatment of mass diffusivity: while the Unity-Lewis model assumes equal diffusivities for all species, the Mixture-Averaged model assigns a distinct value to each species, allowing for differential diffusion effects.

Figure 12 shows the mass diffusivity coefficients computed using Cantera, highlighting the differences between species.

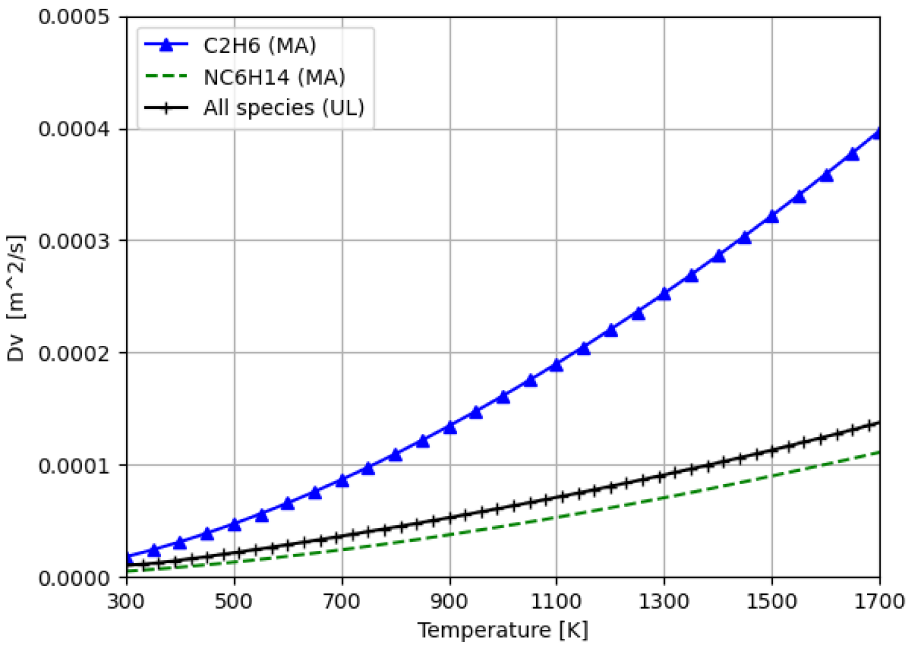

Figure 12: Cantera mass diffusion coefficients comparison.

It's important to notice that Kee [39] explains three different formulas to calculate mass diffusivity depending on the usage. They all differ in the form of Fick's first law to which they are applied. A notation convention is presented to distinguish one usage from another. The mixture-averaged diffusion coefficient D^*_{km} when calculating the molar flux J^*_k with respect to the molar average velocity as a function of the mole-fraction gradient of species k; a mixture-averaged D_{km} when calculating the mass flux j_k with respect to the mass average velocity as a function of the mass-fraction gradient of species k; and D'_{km} when calculating the mass flux j_k with respect to the mass average velocity as a function of the mole-fraction gradient.

$$D^*_{km} = \frac{1 - X_k}{\sum_{j \neq k}^{K} X_j / D_{kj}}, \tag{29}$$

$$D_{km} = \left(\sum_{j \neq k} \frac{X_j}{D_{jk}} + \frac{X_k}{1 - Y_k} \sum_{j \neq k} \frac{Y_j}{D_{jk}} \right)^{-1}, \tag{30}$$

$$D'_{km} = \frac{1 - Y_k}{\sum_{j \neq k}^{K} X_j / D_{kj}}. \tag{31}$$

Since Cantera employs the mass-based formulation D_{km}, the species diffusion flux is given by:

$$j_k = \rho_k \left(\widetilde{V}_k - V \right) = \rho Y_k V_k = -\rho D_{km} \nabla Y_k. \tag{32}$$

However, unlike the Stefan–Maxwell formulation, the Mixture-Averaged model does not inherently ensure conservation of the total mass diffusion flux across control volumes in a finite volume discretization, as it does not enforce the following condition:

$$\sum_{k=1}^{K} \rho Y_k \mathbf{V}_k = 0. \tag{33}$$

In practical terms, this inconsistency can lead to errors in simulations involving inter-

cellular species transport. Nevertheless, in scenarios such as droplet evaporation, where the diffusion velocity primarily determines the local evaporation rate rather than intercell flux, the issue becomes negligible.

To address this inconsistency in Eulerian formulations, Poinsot and Veynante [63] discuss two corrective strategies. In general, resolving this mass-conservation issue depends on the specific numerical scheme and problem setup, and there is no universal correction applicable in all cases. Thus, careful implementation is required when using the Mixture-Averaged model in conservative numerical solvers.

5.3 Lennard-Jones Diffusion Model

The Lennard-Jones (LJ) diffusion model presented here is a simplified model of the methodology outlined by Poling et al. [57], which builds on the formulation proposed by Wilke and Lee [88] for evaluating the vapor–gas mixture diffusion coefficient $D_{v,m}$:

$$D_{v,m} = \frac{[3.03 - (0.98/M_{va}^{1/2})(10^{-7})(T^{3/2})]}{P M_{va}^{1/2} \sigma_{va}^2 \Omega_D}. \tag{34}$$

where M_{va} is the reduced molar mass of the vapor–gas pair, σ_{va} is the collision diameter, and Ω_D is the collision integral, which is a function of the reduced temperature $T^* = k_B T/\varepsilon_{va}$, as described by Sazhin [72].

The reduced mass is computed as:

$$M_{va} = 2[(1/M_v) + (1/M_a)]^{-1} \tag{35}$$

where M_v and M_a are the molar masses of the vapor and gas species, respectively. The LJ parameters σ_{va} and ε_{va}/k_B are obtained from Cantera's thermodynamic database [33], using:

$$\sigma_{va} = \frac{\sigma_v + \sigma_a}{2}, \quad \varepsilon_{va} = \sqrt{\varepsilon_v \varepsilon_a} \tag{36}$$

These parameters are available for common hydrocarbons and gases, as shown in Tables 3 and 4.

Table 3: Lennard-Jones characteristics lengths and energies for vapor species.

Vapor species	$\sigma_{v,a}(A)$	$\varepsilon_{va}/k_B(K)$
n-octane	6.270	612.840
n-decane	6.690	704.920
n-dodecane	7.060	789.160
n-tetradecane	7.480	857.180
n-hexadecane	7.730	938.920
2-methylheptane	6.240	596.060
2-methylundecane	7.120	833.780
toluene	5.549	450.000
meistylene	5.960	523.060

To the gaseous mixture inert the following values were presented in Goodwin et al [32].

Table 4: Lennard-Jones characteristics lengths and energies for gaseous species.

Gaseous species	$\sigma_{v,a}(A)$	$\varepsilon_{va}/k_B(K)$
air	3.711	78.600
argon	3.330	136.500
carbon dioxide	3.760	244.000
methane	3.750	141.400
water	2.600	572.400
nitrogen	3.620	97.530

Air may be treated as a single effective gas species. The molar fraction of the inert gaseous phase is computed by:

$$X_{g_m} = 1 - \sum kX_{v,k_m} \tag{37}$$

The average transport properties of the vapor and gas mixtures—such as molar mass and LJ parameters—are weighted by the respective molar fractions $x_{g,j_m}/\sum_j x_{g,j_m}$ and $x_{v,k_m}/\sum_k x_{v,k_m}$, following the methodology in [71].

In this formulation, multicomponent effects are captured by pairwise combinations of LJ parameters and mixture averaging techniques, offering a simplified yet effective approach to model droplet evaporation in complex spray environments.

5.4 Multicomponent Model

The most detailed and physically accurate description of species transport in multicomponent mixtures is provided by the multicomponent model based on the Chapman-Enskog theory [11]. In this framework, the mass diffusivities, thermal conductivities, and thermal diffusion coefficients are determined by solving a system of equations involving the L matrix, composed of nine submatrix blocks:

$$\begin{pmatrix} L^{00,00} & L^{00,10} & 0 \\ L^{10,00} & L^{10,10} & L^{10,01} \\ 0 & L^{01,10} & L^{01,01} \end{pmatrix} \begin{pmatrix} a^1_{00} \\ a^1_{10} \\ a^1_{01} \end{pmatrix} = \begin{pmatrix} 0 \\ X \\ X \end{pmatrix}, \tag{38}$$

where the right-hand side contains mole fraction vectors X_k. The first-order approximation to the multicomponent diffusion coefficients is given by Lewis and von Elbe [25] as:

$$D_{jk} = X_j \frac{16T}{25pm_k} \overline{W} \left(P_{jk} - P_{jj}\right), \tag{39}$$

The first-order approximation to the multicomponent diffusion coefficients [25] is given in terms of the inverse of the $L^{00,00}$ block as a linear transformation between mole fraction gradients and diffusion velocities. Specifically, the matrix $L^{00,00}$ contains interaction terms derived from the Chapman–Enskog collision integrals, and its inverse encapsulates the multicomponent transport coupling. The resulting diffusivity matrix D_{jk} quantifies how the flux of species j responds to the concentration gradient of species k, accounting for cross-diffusion effects. Unlike in the binary case, these coefficients are not independent and must satisfy mass conservation and symmetry constraints imposed by kinetic theory.

Bird [8] emphasizes the difference between binary diffusion and multicomponent diffusion. In binary diffusion the movement of species K is always proportional to the negative of the concentration gradient of species K. In multicomponent diffusion, however, other interesting situations can arise: (*i*) reverse diffusion, in which a species moves against its own concentration gradient; (*ii*) osmotic diffusion, in which a species diffuses even though its concentration gradient is zero; (*iii*) diffusion barrier, when a species does not diffuse

even though its concentration gradient is nonzero. In addition, the flux of a species is not necessarily collinear with the concentration gradient of that species.

These phenomena arise due to the coupling between species through cross-diffusion terms, which are absent in simpler models.

The thermal conductivity is also computed differently in the multicomponent model, being fully coupled with the diffusion process via the Chapman-Enskog framework.

$$\lambda_{0,\text{trans}} = -4 \sum_{k=1}^{K} X_k a^1_{k10}, \tag{40}$$

$$\lambda_{0,\text{int}} = -4 \sum_{k=1}^{K} X_k a^1_{k01}, \tag{41}$$

$$\lambda_0 = \lambda_{0,\text{trans}} + \lambda_{0,\text{int}}. \tag{42}$$

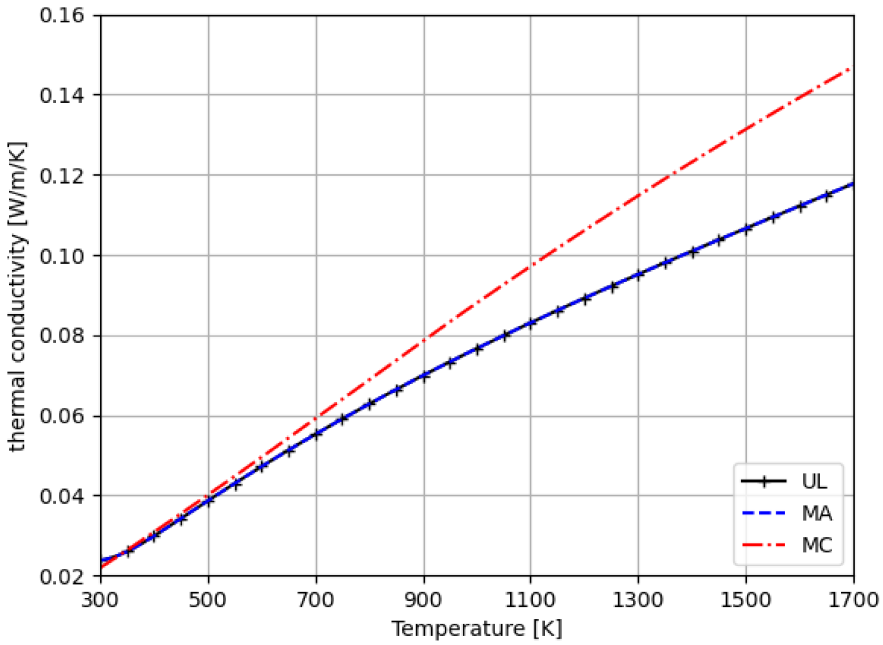

Figure 13: Thermal conductivity coefficients computed using Cantera. UL: Unity-Lewis, MA: Mixture-Averaged, MC: Multicomponent.

Figure 13 illustrates the thermal conductivity values obtained using different transport

models in Cantera. As observed, the Unity-Lewis and Mixture-Averaged models compute thermal conductivity using the same formulation, based on simplified mixture-averaging rules. In contrast, the Multicomponent model incorporates additional transport phenomena, such as the Soret effect (thermal diffusion), and evaluates thermal conductivity through a more rigorous Chapman–Enskog-based formulation. As a result, its predicted values may differ from the simpler models, especially in systems with strong thermal gradients or species with highly distinct transport properties.

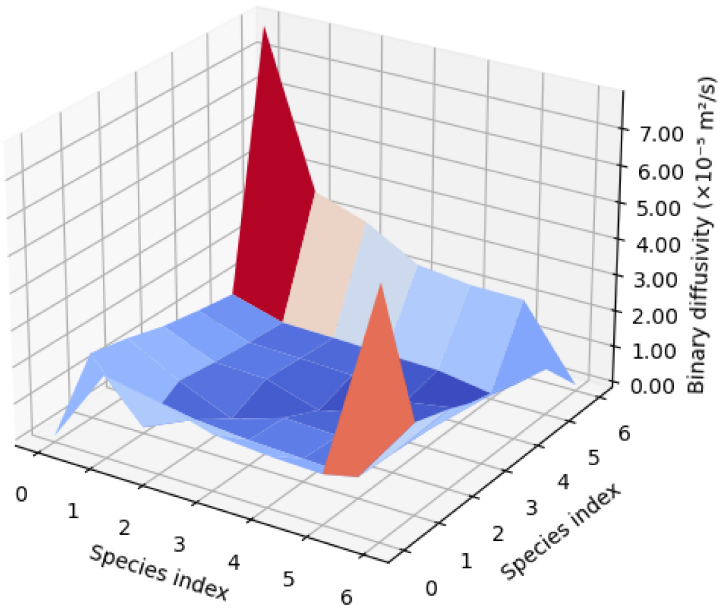

Figure 14: Multicomponent diffusion coefficients for a hydrocarbon mixture.

Figure 14 presents the multicomponent diffusion coefficients calculated in Cantera for a chemical mechanism involving seven species. In this formulation, the diffusivity of each species is evaluated with respect to every other species, resulting in a full matrix (or second-order tensor) of cross-diffusion coefficients. This representation captures the coupling between species in multicomponent transport, which is essential for accurately modeling systems where differential diffusion plays a significant role.

Table 5: Comparison of transport models for spray simulation

Model	Diffusivity	Thermal Conductivity	Viscosity	Main Characteristics
Unity-Lewis	Assumes D_k such that $Le = 1$ for all species	Computed based on simplified mean values	Calculated using Wilke/Bird correlations	• Simplest model • Assumes mass and thermal diffusivities are equal • Fast and computationally inexpensive • Suitable for single-component or weakly coupled systems
Mixture-Averaged	D_{km} from binary D_{kj} using Wilke or Hirschfelder-Curtiss approx.	Same as Unity-Lewis	Same as Unity-Lewis	• Species-specific diffusivity • Captures differential diffusion • Conservation may require correction (e.g. V_c) • Balanced cost vs accuracy
Lennard-Jones	Derived from LJ potentials using σ, ε from molecular data	Not explicitly modified	Not explicitly modified	• Molecular-based estimation of $D_{v,m}$ • Accounts for species mass, diameter, interaction energy • Suitable for low-pressure gas mixtures • Implemented in MFSim using Sazhin's approach
Multicomponent	Solves Stefan-Maxwell or Chapman-Enskog system; D_{jk} via matrix inversion	Computed using L-matrix blocks from C.-E. theory	Computed via molecular theory	• Most accurate and rigorous model • Handles non-ideal behavior, cross-diffusion • High computational cost • Required for strongly coupled or reacting multicomponent systems

Despite its accuracy, the multicomponent model is computationally expensive. For a mixture with N species, the number of diffusion coefficients scales as $N(N-1)/2$, requiring matrix inversion at every spatial and temporal point in the simulation. This cost becomes prohibitive in large-scale simulations with many species or high mesh resolution. Therefore, multicomponent diffusion models are typically used only in highly detailed simulations, such as DNS or LES of flames and combustion fronts.

An additional advantage of multicomponent models is the correct prediction of counter-gradient diffusion (CGD), a phenomenon observed in nonpremixed turbulent flames. Jiang [38] shows that CGD effects — in which the scalar flux opposes the scalar gradient — can arise naturally in multicomponent formulations due to differential diffusion and thermodiffusion coupling, especially for light species like hydrogen. This behavior cannot be captured by unity-Lewis or mixture-averaged models.

In summary, the multicomponent and Stefan–Maxwell models offer the most comprehensive representation of species transport in reacting flows. However, their use requires balancing physical fidelity with numerical feasibility, particularly in large, complex simulations.

6 Mathematical Modelling

As highlighted in Subsection 1.3, this section will explore the subjects, methods, and methodologies implemented in MFSim by previous researchers, focusing on the multicomponent droplet evaporation process. It's important to mention that many concepts written by their dissertations and thesis were studied, and definitely they are of utmost importance to understand some criteria and conditions taken to analyze the particle behavior.

6.1 Continuum Hypothesis

Classical fluid mechanics is based on the continuum hypothesis, which assumes that fluids occupy all space continuously and that their properties are smoothly distributed at all points. Under this assumption, the governing equations for fluid flow consist of the mass conservation equation, the Navier-Stokes equations for momentum, and the energy conservation equation. Collectively, these are known as the Navier-Stokes equations.

This framework allows for the analysis of the macroscopic behavior of fluids without significant error due to molecular-scale variations. As discussed by White [86], fluid molecules are in constant motion, making it impossible to precisely determine their instantaneous positions with current computational capabilities. Therefore, there exists a physical lower limit to the size of a control volume or mesh element below which molecular fluctuations become non-negligible.

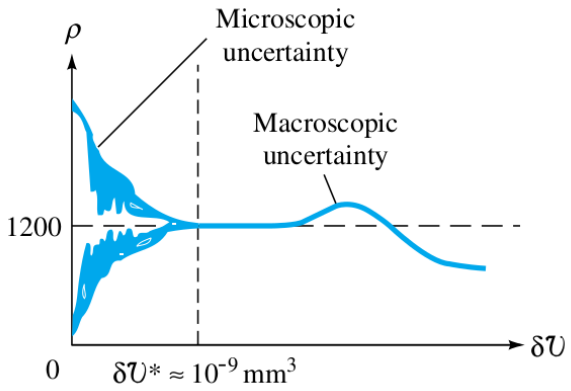

Figure 15: Calculated density versus size of the elemental volume. White [86].

The local fluid density ρ is defined as the limit:

$$\rho = \lim_{\delta\mathcal{V} \to \delta\mathcal{V}^*} \frac{\delta m}{\delta \mathcal{V}} \tag{43}$$

where $\delta\mathcal{V}^*$ is the minimum volume at which the continuum assumption holds. According to White [86], this critical volume is approximately 10^{-9} mm^3 for liquids and for gases at atmospheric pressure.

As further noted by Silveira Neto [54], this limiting volume may increase depending on the Reynolds number of the flow. It is important to emphasize that the adoption of continuum mechanics does not preclude the presence of discontinuities in fluid properties across interfaces, such as free surfaces or shock waves in compressible flows.

6.2 Eulerian–Lagrangian Model

For spray combustion simulations and phase change applications, the Eulerian–Lagrangian approach is widely employed, particularly for dilute sprays, where the droplet volume fraction is low. In this formulation, the continuous phase is treated using the Eulerian framework, in which mass, momentum, energy, and species transport equations are solved on a fixed spatial grid. Meanwhile, the dispersed phase (droplets) is tracked individually using a Lagrangian frame of reference, where ordinary differential equations govern the temporal evolution of each droplet's position, velocity, diameter, and temperature.

The Lagrangian formulation typically adopts the point-droplet approximation, assuming sphericity and quasi-steady interface conditions. Interactions between droplets and the surrounding gas—such as momentum exchange, energy transfer, and mass evaporation—introduce source terms into the Eulerian equations. These exchanges significantly influence the spatial and temporal distribution of scalar fields, especially temperature and species mass fractions, which in turn affect the computation of thermophysical properties like density and viscosity.

Lefebvre [45] discusses that, from a physical standpoint, a droplet in a multiphase

flow is in mechanical equilibrium when the internal conditions counterbalance external influences, such as aerodynamic forces and surface tension. In such cases, the internal vapor pressure p_v balances the external aerodynamic pressure p_A and the surface tension pressure p_σ:

$$p_v = p_A + p_\sigma, \tag{44}$$

with the surface tension pressure for a spherical droplet expressed as:

$$p_\sigma = \frac{4\sigma}{D}, \tag{45}$$

where σ is the surface tension and D is the droplet diameter.

In the present work, this pressure equilibrium is not explicitly modeled; instead, droplet motion and mass exchange are computed assuming spherical shape and quasi-steady conditions at the interface.

Peters [59] highlights several advantages of the Discrete Particle Method (DPM): its versatility in modeling a wide range of industrial particulate systems, the capacity to resolve phase interaction within individual particles, the ensemble motion of particle populations, and reactive flows in the void space, also known as Stefan flow.

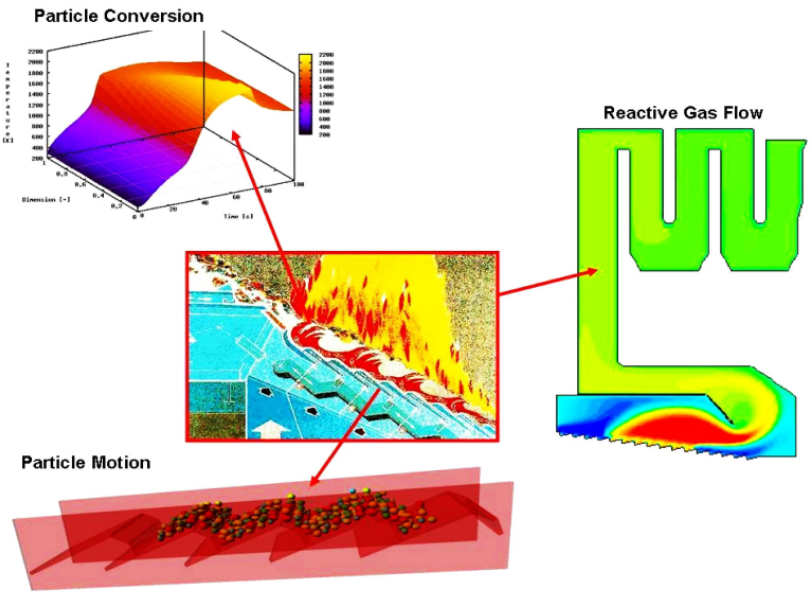

Figure 16: Approach to solid fuel conversion using the Discrete Particle Method (DPM). Source: Peters [59].

6.2.1 Governing Equations and Particle-Phase Coupling

In Eulerian–Lagrangian frameworks, the governing equations for mass, momentum, energy, and species transport in the gas phase must account for source terms arising from the interaction with the dispersed phase. These source terms represent mass, momentum, and energy exchange due to droplet heating, vaporization, and motion, and they appear on the right-hand side of the transport equations:

$$\frac{\partial \rho}{\partial t} + \frac{\partial \rho u_i}{\partial x_i} = S_m^L, \tag{46}$$

$$\frac{\partial \rho u_i}{\partial t} + \frac{\partial \rho u_i u_j}{\partial x_i} = -\frac{\partial p}{\partial x_i} + \frac{\partial \tau_{ij}}{\partial x_i} + S_{u,i}^L, \tag{47}$$

$$\frac{\partial \rho c_p T}{\partial t} + \frac{\partial \rho u_i c_p T}{\partial x_i} = -\frac{\partial q_i}{\partial x_i} + \tau_{ij}\frac{\partial u_i}{\partial x_j} + S_{cpT}^L, \tag{48}$$

$$\frac{\partial \rho Y_k}{\partial t} + \frac{\partial \rho u_i Y_k}{\partial x_i} = -\frac{\partial J_{k,i}}{\partial x_i} + S_k^L. \tag{49}$$

Here ρ is the density, u_i the velocity in the i direction, p the pressure, τ_{ij} the viscous stress tensor, T the gas temperature, c_p the specific heat capacity at constant pressure, k the thermal conductivity, and Y_k is the mass fraction of the k species. q_i is the heat flux and $J_{k,i}$ is the molecular diffusion flux of species k.

The terms S_m^L, $S_{u,i}^L$, S_{cpT}^L, and S_k^L denote the source terms introduced by the Lagrangian phase into the continuity, momentum, energy, and species equations, respectively. These terms are nonzero in regions where droplets are present and act as localized sources of mass, energy, and momentum. The heat and mass diffusion fluxes are evaluated using Fourier's and Fick's laws, respectively [8].

For Newtonian fluids, the viscous stress tensor τ_{ij} is expressed as:

$$\tau_{ij} = \mu \left(\frac{\partial u_i}{\partial x_j} + \frac{\partial u_j}{\partial x_i} \right) - \frac{2}{3} \mu \frac{\partial u_k}{\partial x_k} \delta_{ij}, \tag{50}$$

where μ is the dynamic viscosity, and δ_{ij} is the Kronecker delta function.

To resolve the turbulent and unsteady nature of high-speed spray flows, Large-Eddy Simulation (LES) is employed. LES resolves the largest turbulent structures explicitly, while smaller, subgrid-scale (SGS) phenomena are modeled. Compared to Reynolds-Averaged Navier–Stokes (RANS) models, which provide time-averaged solutions, LES offers greater temporal and spatial fidelity, particularly in capturing transient interactions between the gas and droplet phases [37]. For these reasons, LES is adopted in this study.

6.2.2 Filtered transport equations

The core idea behind the Large-Eddy Simulation (LES) methodology is to resolve the largest turbulent structures in the flow, typically those larger than the computational grid, while modeling the nonlinear interactions between the resolved and subgrid-scale (SGS) motions. In this work, a box filter in physical space is employed. A filtered quantity f is defined as:

$$\overline{f}(x) = \int f(x')F(x - x')\,dx', \tag{51}$$

where F is the LES filter, defined as:

$$F(\mathbf{x}) = F(x_1, x_2, x_3) = \begin{cases} \frac{1}{\Delta^3}, & \text{if } |x_i| \leq \Delta,\ i = 1, 2, 3, \\ 0, & \text{otherwise.} \end{cases} \tag{52}$$

with Δ representing the characteristic filter width, taken as the cubic root of the control volume V_c, i.e., $\Delta = V_c^{1/3}$.

In flows with variable density, it is convenient to define the mass-weighted (Favre) filtered variable $\tilde{f}$ as:

$$\overline{\rho\tilde{f}}(\mathbf{x}) = \int \rho f(\mathbf{x}')F(\mathbf{x} - \mathbf{x}')\,d\mathbf{x}'. \tag{53}$$

In numerical simulations, $\overline{f}$ and $\tilde{f}$ are the computed filtered quantities, while $f' = f - \tilde{f}$ represents the unresolved subgrid-scale fluctuations. The governing equations for the gas phase are thus written in their filtered form as:

$$\frac{\partial\overline{\rho}}{\partial t} + \frac{\partial\overline{\rho}\tilde{u}_i}{\partial x_i} = S_m^L, \tag{54}$$

$$\frac{\partial\overline{\rho}\tilde{u}_i}{\partial t} + \frac{\partial\overline{\rho}\tilde{u}_i\tilde{u}_j}{\partial x_i} = -\frac{\partial\overline{p}}{\partial x_i} + \frac{\partial\overline{\tau}_{ij}}{\partial x_i} - \frac{\partial\tau_{ij}^{\text{sgs}}}{\partial x_j} + S_{u,i}^L, \tag{55}$$

$$\frac{\partial\overline{\rho}c_p\tilde{T}}{\partial t} + \frac{\partial\overline{\rho}\tilde{u}_i c_p\tilde{T}}{\partial x_i} = -\frac{\partial(\overline{q}_i + q_i^{\text{sgs}})}{\partial x_i} + \frac{\partial[(\overline{\tau}_{ij} - \tau_{ij}^{\text{sgs}})\tilde{u}_i]}{\partial x_j} + S_{cpT}^L, \tag{56}$$

$$\frac{\partial\overline{\rho}\tilde{Y}_k}{\partial t} + \frac{\partial\overline{\rho}\tilde{u}_i\tilde{Y}_k}{\partial x_i} = -\frac{\partial(\overline{J}_{k,i} + J_{k,i}^{\text{sgs}})}{\partial x_i} + S_k^L. \tag{57}$$

In the equations above, the superscript *sgs* denotes subgrid-scale terms. These require

appropriate modeling, as they represent unresolved phenomena due to filtering at the LES cutoff scale.

6.2.3 Subgrid-scale models

The unclosed subgrid-scale (SGS) terms that arise from the filtering of the transport equations are modeled using gradient-type closures [44]. The unresolved SGS stress tensor τ_{ij}^{sgs} is modeled following the Boussinesq hypothesis [27]:

$$\tau_{ij}^{\text{sgs}} - \frac{\delta_{ij}}{3}\tau_{kk}^{\text{sgs}} = \mu_{\text{sgs}}\left(\frac{\partial \tilde{u}_i}{\partial x_j} + \frac{\partial \tilde{u}_j}{\partial x_i} - \frac{2}{3}\frac{\partial \tilde{u}_k}{\partial x_k}\delta_{ij}\right) = 2\mu_{\text{sgs}}\left(\tilde{S}_{ij} - \frac{\delta_{ij}}{3}\tilde{S}_{kk}\right), \tag{58}$$

In this context, δ_{ij} allows the SGS stress tensor τ_{ij}^{sgs} to be decomposed into its **deviatoric (anisotropic)** and **isotropic** components, ensuring that only the anisotropic part contributes to the modeled turbulent viscosity.

$$\tilde{S}_{ij} = \frac{1}{2}\left(\frac{\partial \tilde{u}_i}{\partial x_j} + \frac{\partial \tilde{u}_j}{\partial x_i}\right). \tag{59}$$

In this work, the eddy viscosity μ_{sgs} is computed using the dynamic Smagorinsky model proposed by Germano [30], with the modifications introduced by Lilly [47]. This model assumes that the small-scale motions are in local equilibrium, meaning that production and dissipation of turbulent energy are balanced. The eddy viscosity is given by:

$$\mu_{\text{sgs}} = 2\overline{\rho}(C_s\Delta)^2|\tilde{S}| = 2\overline{\rho}(C_s\Delta)^2\left(2\tilde{S}_{ij}\tilde{S}_{ij}\right)^{1/2}, \tag{60}$$

where C_s is the Smagorinsky constant, dynamically computed during the simulation as described in detail by Vedovoto [82], and Δ is the filter width.

The subgrid heat flux q_i^{sgs} and species diffusion flux $J_{k,i}^{\text{sgs}}$ are also modeled with gradient-type approximations:

$$q_i^{\text{sgs}} = -\overline{\rho}\frac{\mu_{\text{sgs}}}{\text{Pr}_t}\frac{\partial \tilde{c}_p T}{\partial x_i}, \tag{61}$$

$$J_{k,i}^{\text{sgs}} = -\overline{\rho}\frac{\mu_{\text{sgs}}}{\text{Sc}_t}\frac{\partial \tilde{Y}_k}{\partial x_i}, \tag{62}$$

where Pr_t and Sc_t are the turbulent Prandtl and Schmidt numbers, respectively.

For more details on the Eulerian-phase modeling and implementation in MFSim, the reader is referred to previous works developed at MFLab, such as those by Vedovoto [82], Melo [52], and Damasceno [20].

6.3 Flow regime and Coupling Model

The flow regime (disperse and dense) is intrinsically related to the coupling model of Euler-Lagrange simulation.

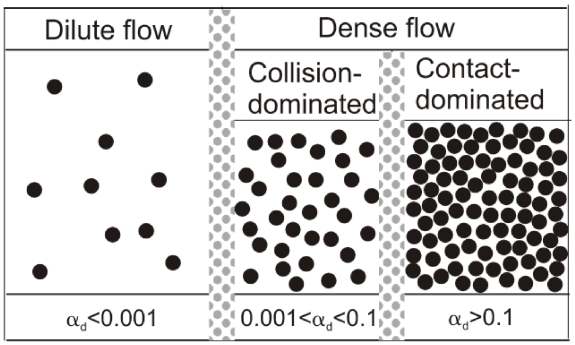

Figure 17: Flow regimes for dilute and dense flows. Source: Crowe [17].

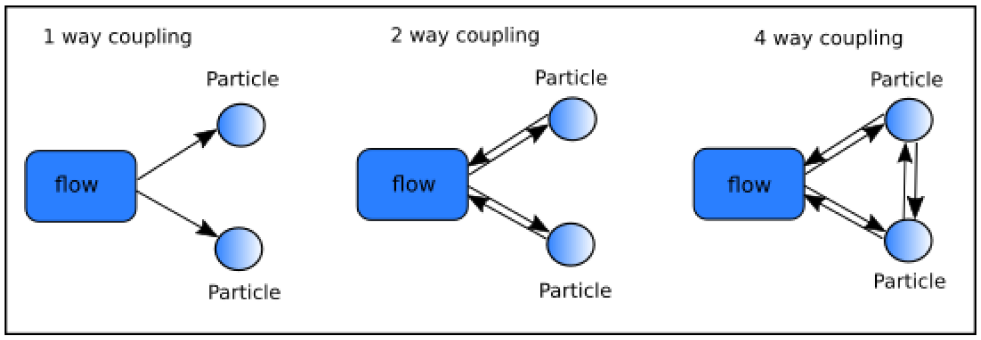

Figure 18: Schematic diagram of the continuous and dispersed phase coupling method. Source: Adapted Guarato [21].

6.4 Droplet Motion

In engineering applications involving spray evaporation, the dominant forces acting on a droplet are typically drag and gravity. Other forces—such as the Basset history term, added mass, Magnus, Saffman lift, buoyancy, and pressure gradient—are generally negligible under the conditions of interest [74]. Based on these assumptions, and within a Lagrangian framework, the governing equations for droplet motion are expressed as:

$$\frac{dx_{d,i}}{dt} = u_{d,i}, \tag{63}$$

$$m_d \frac{du_{d,i}}{dt} = \sum F_{d,i} = \frac{u_i - u_{d,i}}{\tau_d} + g_i, \tag{64}$$

where $x_{d,i}$ and $u_{d,i}$ are the droplet position and velocity components in direction i, u_i is the gas-phase velocity, and g_i is the gravitational acceleration component. The droplet relaxation time τ_d quantifies the response time of the droplet to velocity changes in the surrounding fluid and is defined as:

$$\tau_d = \frac{4}{3} \frac{\rho_l}{\rho_g} \frac{D_d}{C_D \left| \mathbf{u}_i - \mathbf{u}_{d,i} \right|}, \tag{65}$$

where ρ_l and ρ_g denote the densities of the liquid droplet and the gas phase, respectively, and D_d is the droplet diameter. The relative velocity magnitude between the gas and the droplet is given by $|\mathbf{u}_i - \mathbf{u}_{d,i}|$. Note that droplet mass variation due to evaporation is neglected in Eq. (64).

The drag coefficient C_D is determined by semi-empirical correlations. In this work, the correlation proposed by Feng and Michaelides [26] is adopted. This formulation accounts for internal circulation within viscous droplets by introducing the viscosity ratio $\lambda = \mu_l/\mu_g$, where μ_l and μ_g are the viscosities of the liquid and gas phases, respectively. While many classical correlations exist for solid particles ($\lambda \to \infty$) and inviscid bubbles ($\lambda \to 0$) [13], few incorporate the internal viscosity effects relevant for liquid droplets.

For $0 \leq Re_d \leq 5$, the drag coefficient is given by:

$$C_D = \frac{8}{Re_d}\frac{3\lambda+2}{\lambda+1}\left(1+0.05\frac{3\lambda+2}{\lambda+1}Re_d\right) - 0.01\frac{3\lambda+2}{\lambda+1}Re_d\ln(Re_d), \tag{66}$$

where the droplet Reynolds number is defined as:

$$Re_d = \frac{\rho_g D_d \left|u_i - u_{d,i}\right|}{\mu_g}. \tag{67}$$

For intermediate Reynolds numbers ($5 < Re_d \leq 1000$), different expressions for C_D are used depending on the viscosity ratio λ:

$$C_D = \begin{cases} \dfrac{2-\lambda}{2}C_{D,0} + \dfrac{4\lambda}{6+\lambda}C_{D,2}, & \text{if } 0 \leq \lambda \leq 2, \\ \dfrac{4}{\lambda+2}C_{D,2} + \dfrac{\lambda-2}{\lambda+2}C_{D,\infty}, & \text{if } 2 < \lambda \leq \infty, \end{cases} \tag{68}$$

with the following auxiliary expressions:

$$C_{D,0} = \frac{48}{Re_d}\left(1 + \frac{2.21}{\sqrt{Re_d}} - \frac{2.14}{Re_d}\right), \tag{69}$$

$$C_{D,2} = 17.0Re_d^{-2/3}, \tag{70}$$

$$C_{D,g} = \frac{24}{Re_d}\left(1 + \frac{1}{6}Re_d^{2/3}\right). \tag{71}$$

Finally, for $Re_d > 1000$, the drag coefficient is assumed constant:

$$C_D = 0.44. \tag{72}$$

This comprehensive formulation allows for smooth transitions across a wide range of Reynolds numbers and viscosity ratios, capturing the dominant effects of internal and

external fluid dynamics on droplet drag. For more details, the reader is referred to previous studies conducted at the MFLab, such as those by Pinheiro [60] and Santos [21].

6.5 Evaporation rate

The Classical Evaporation Model (CEM), also known as the Stefan-Maxwell model or rapid mixing model, was initially introduced by Spalding [76] and further developed by Godsave [31]. It was later improved by Maxwell by incorporating Stefan's flow, which refers to the mass flux between the ambient gas and the droplet [60].

Bird [8] introduces the Maxwell-Stefan convective model, which calculates both mass and heat transport in the presence of phase change. The Maxwell-Stefan equations were originally proposed for binary mixtures and were later generalized by Stefan for multi-component flows based on the Hirschfelder-Curtiss equation.

A quasi-steady gaseous medium under constant pressure and temperature is assumed, along with thermodynamic equilibrium at the droplet surface between the liquid and vapor phases. The vapor pressure at the droplet interface is taken as equal to the saturation pressure of the evaporating component at the droplet surface temperature.

Based on a detailed investigation of different evaporation models, Pinheiro [61] implemented in MFSim an evaporation model based on Abramzon and Sirignano [1]. In this document, this model will be referred to as the Abramzon and Sirignano Model (ASM), even with later implementations by Continillo and Sirignano [15], which generalized the method to deal with multicomponent droplets. In this model, the droplet evaporation rate $\dot{m}_d$ is given by:

$$\dot{m}_d = 2\pi R_d D_{v,m} \rho_m Sh_m \ln\left(1 + B_M\right), \tag{73}$$

where R_d is the droplet radius, $D_{v,m}$ the vapor diffusion coefficient, ρ_m the density of the gas-vapor mixture in the film around the droplet, Sh_m the modified Sherwood number, and B_M the Spalding mass transfer number.

$$Sh_m = 2 + \frac{Sh_0 - 2}{F_M}, \tag{74}$$

$$F_M = (1 + B_M)^{0.7} \frac{\ln(1 + B_M)}{B_M}, \tag{75}$$

The modified Sherwood number accounts for internal circulation within the droplet. The well-known Ranz-Marshall empirical correlation [65], modified by Li and Mason [46] for high Reynolds numbers, is used to estimate Sh_0:

$$Sh_0 = \begin{cases} 2 + 0.6 Re_m^{1/2} Sc_m^{1/3}, & \text{if } Re_m \leq 200 \\ 2 + 0.6 Re_m^{1/2} Sc_m^{1/3} + 0.02 Re_m^{0.8} Sc_m^{1/3}, & \text{if } 200 < Re_m \leq 1500 \\ 2 + 0.000045 Re_m^{1.8}, & \text{if } Re_m > 1500 \end{cases} \tag{76}$$

where Sc_m is the Schmidt number and Re_m is the droplet Reynolds number:

$$Sc_m = \frac{\mu_m}{\rho + m D_{v,m}}, \tag{77}$$

$$Re_m = \frac{2 \rho_g R_d |u_i - u_{d,k}|}{\mu_m} \tag{78}$$

in which μ_m is the dynamic viscosity and $|u_i - u_{d,k}|$ is the slip velocity between the gas and the droplet.

The Spalding mass transfer number B_M is calculated as:

$$B_M = \frac{\sum_k Y_{v,k_s} - \sum_k Y_{v,k_g}}{1 - \sum_k Y_{v,k_s}}, \tag{79}$$

where Y_{v,k_s} and Y_{v,k_g} are the vapor mass fractions of species k at the droplet surface and in the far-field ambient gas, respectively.

At thermodynamic equilibrium, the partial pressure of each component k at the droplet

surface is given by:

$$p_{v,k_s} = \gamma_k X_{l,k_s} p^*_{v,k}, \tag{80}$$

where X_{l,k_s} is the mole fraction of component k in the liquid phase at the droplet surface, $p^*_{v,k}$ is its pure component vapor pressure, and γ_k is the activity coefficient. Assuming ideal mixtures of hydrocarbons, $\gamma_k \approx 1$, and Eq. 80 simplifies to Raoult's law:

$$p_{v,k_s} = X_{l,k_s} p^*_{v,k}, \tag{81}$$

According to Woodrow [90], Eq. 81 is a reasonable assumption due to the similar chemical nature of the components typically present in spray fuels.

The vapor mole fraction at the surface is computed as:

$$X_{v,k_s} = \frac{p_{v,k_s}}{p_g}. \tag{82}$$

and the corresponding vapor mass fraction Y_{v,k_s} is then:

$$Y_{v,k_s} = \frac{X_{v,k_s} W_{v,k}}{X_{v,k_s} W_{v,k} + X_{g_s} W_g}, \tag{83}$$

where W denotes molecular weight, and subscripts v and g refer to vapor and gas phases, respectively.

To determine thermophysical properties at the droplet interface, an averaging procedure is employed. Following recommendations by Hubbard, Denny and Mills [36], and Yuen and Chen [96], the 1/3 averaging rule (Wilke's rule) is adopted. Accordingly, the reference values are:

$$T_m = T_s + \frac{1}{3}(T_g - T_s), \tag{84}$$

$$Y_{v,k_m} = Y_{v,k_s} + \frac{1}{3}\left(Y_{v,k_g} - Y_{v,k_s}\right). \tag{85}$$

6.6 Mixture Properties

The evaluation of thermophysical properties of multicomponent droplets is essential for accurately modeling evaporation, heat transfer, and momentum exchange. In this work, the mixture properties are computed following the formulation proposed by Sazhin [69], based on weighted averages of the corresponding pure component properties.

The mixture properties are estimated as follows:

$$L_\nu = \sum_k \left(\varepsilon_k L_k\right), \tag{86}$$

where L_ν is the latent heat of vaporization of the mixture, L_k is the latent heat of species k, and ε_k is the mass fraction of evaporated component k among all components that have already evaporated. This definition ensures that the mixture latent heat reflects the contribution of each component to the ongoing evaporation process.

$$p_{vs} = \sum_k \left(X_{l,k} p_{v,k,s}\right), \tag{87}$$

where p_{vs} is the total vapor pressure at the droplet surface, $X_{l,k}$ is the mole fraction of component k in the liquid phase, and $p_{v,k,s}$ is the partial vapor pressure of component k at the droplet surface, typically evaluated via Raoult's law.

$$\rho_l = \left[\sum_k \left(\frac{Y_{l,k}}{\rho_{l,k}}\right)\right]^{-1}, \tag{88}$$

where ρ_l is the liquid density of the mixture, $Y_{l,k}$ is the mass fraction of species k in the liquid phase, and $\rho_{l,k}$ is the density of the pure liquid species k. This formulation is based on the additive volume rule and accounts for mass-based averaging.

$$\ln \mu_l = \sum_k \left(X_{l,k} \ln \mu_{l,k} \right), \tag{89}$$

where μ_l is the dynamic viscosity of the mixture and $\mu_{l,k}$ is the dynamic viscosity of species k. This logarithmic mixing rule, weighted by mole fractions $X_{l,k}$, is commonly used for estimating the viscosity of ideal liquid mixtures.

$$k_l = \left[\sum_k \left(\frac{Y_{l,k}}{k_{l,k}^2} \right) \right]^{-1/2}, \tag{90}$$

where k_l is the thermal conductivity of the mixture and $k_{l,k}$ is the thermal conductivity of species k. This is a semi-empirical correlation for computing mixture conductivity from species conductivities, often used in combustion and spray modeling.

$$c_l = \sum_k \left(Y_{l,k} c_{l,k} \right), \tag{91}$$

where c_l is the specific heat capacity of the vapor and $c_{l,k}$ is the specific heat of species k. This mass-fraction-weighted average assumes ideal mixing behavior.

$$D_l = \sum_k \left(X_{l,k} D_{l,k} \right), \tag{92}$$

where D_l is the effective binary diffusion coefficient in the liquid phase and $D_{l,k}$ is the diffusivity of species k in the mixture. The averaging is performed using mole fractions, which is appropriate for transport properties governed by molecular interactions.

The thermodynamic and transport properties are assumed constant during each time step, but they are updated between time steps based on the current droplet composition and temperature. This quasi-steady approach reduces computational cost while maintaining sufficient accuracy for most engineering applications.

6.7 Thermal Conductivity and Diffusion Models

The treatment of species diffusion and internal thermal transport in spray evaporation is a critical component of accurate CFD modeling. However, many studies adopt simplifying assumptions to reduce computational cost, often at the expense of physical fidelity. As noted by Sazhin [69], models frequently treat droplet composition and vaporization as single-component processes or assume uniform diffusivity across all species, which can misrepresent multicomponent evaporation dynamics, particularly in mixtures with large volatility differentials.

Several authors [43, 2, 28, 69] have proposed reduced-order models to capture the essential features of multicomponent evaporation while maintaining computational feasibility. For instance, the quasi-discrete models developed by Sazhin et al. enable transient resolution of both thermal and mass transfer processes using effective conductivity and diffusivity coefficients. These methods reconcile detailed transport physics with tractable numerical formulations, particularly when full resolution of species gradients is computationally prohibitive.

Brenn et al. [10] further noted that, in the gas phase, the inter-diffusivity between volatile components can be orders of magnitude lower than their respective diffusivities in air. This justifies the approximation that each species diffuses independently into the carrier gas, significantly simplifying the mass transport formulation in the gas phase.

A key factor in predicting high-speed liquid jet sprays is accurate modeling of the interaction between gas and liquid phases. Due to the unsteady and turbulent nature of the gas flow produced by high-speed sprays, along with the intrinsically transient behavior of other physical phenomena in the liquid droplets, Large-Eddy Simulation (LES) is considered more suitable than Reynolds-Averaged Navier-Stokes (RANS) for capturing such features. Although RANS remains useful for engineering design, LES provides enhanced fidelity in transient flow resolution and is therefore adopted in this work [37].

6.7.1 Thermal Conductivity Models

Accurate prediction of droplet heating is critical for modeling evaporation dynamics in multicomponent sprays. Various thermal conductivity models have been proposed to account for internal temperature gradients and their effects on evaporation.

The Infinite Thermal Conductivity (ITC) model assumes a uniform temperature within the droplet, implying that the center, surface, and average temperatures are equal: $T_{d,c} = T_{d,s} = T_{d,av}$. This simplification leads to a straightforward energy balance but neglects internal temperature gradients. As a result, it tends to underestimate the surface temperature, especially under high ambient conditions, which increases the latent heat requirement and consequently reduces the evaporation rate.

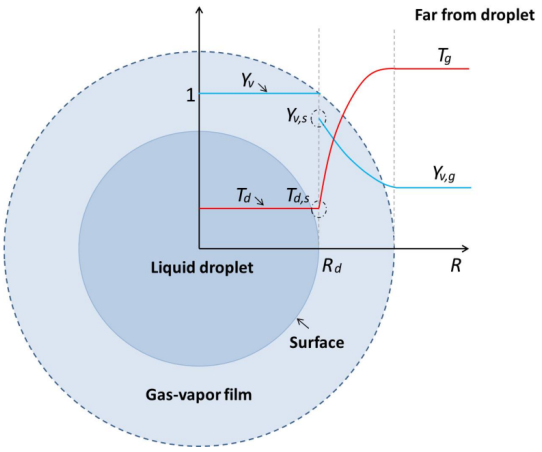

Figure 19: ITC internal temperature representation. Source: Pinheiro [60].

In contrast to this simplification, the Finite Thermal Conductivity (FTC) model accounts for internal thermal gradients, enabling more realistic predictions under non-isothermal conditions. The FTC model discretizes the droplet into radial layers and solves the unsteady heat conduction equation. An example of the internal temperature field obtained using the FTC approach is shown in Figure 20.

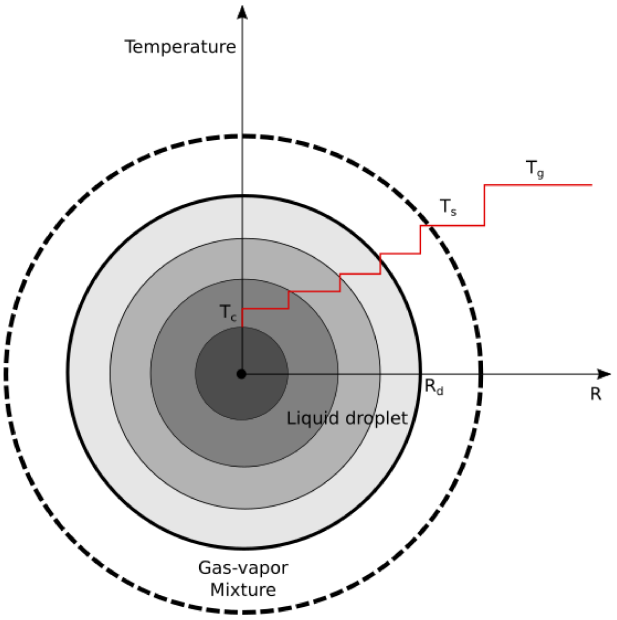

Figure 20: FTC internal temperature representation.

In spherical coordinates, assuming Fourier's law of heat conduction, constant liquid properties (k_l, ρ_l, c_{p_l}), spherical symmetry, and zero internal velocity ($u_R = u_\theta = u_\phi = 0$), the energy balance inside the droplet becomes:

$$\frac{\partial T}{\partial t} = \frac{k_l}{\rho_l c_{p_l}} \left(\frac{\partial^2 T}{\partial R^2} + \frac{2}{R} \frac{\partial T}{\partial R} \right), \tag{93}$$

This equation is solved subject to the initial condition:

$$T(R)\big|_{t=0} = T_0, \tag{94}$$

and the Robin boundary condition at the droplet surface:

$$h(T_{eff} - T_s) = k_l \frac{\partial T}{\partial R}\bigg|_{R=R_d-0}, \tag{95}$$

where T_{eff} is the effective gas-side temperature accounting for evaporation effects, T_s is the droplet surface temperature, and h is the convective heat transfer coefficient. The latter is calculated as:

$$h = \frac{Nu^*}{2}\frac{k_g}{R_d}, \tag{96}$$

with the effective Nusselt number:

$$Nu^* = Nu_m \frac{\ln(1.0 + B_T)}{B_T}, \tag{97}$$

and the Spalding heat transfer number B_T:

$$B_T = (1 + B_M)^{\varphi} - 1, \tag{98}$$

$$\varphi = \left(\frac{c_{p_v}}{c_{p_g}}\frac{Sh}{Nu}\right)\frac{1}{Le_m}. \tag{99}$$

Here, c_{p_v} and c_{p_g} are the specific heats of vapor and gas, respectively. The Lewis number Le_m is given by:

$$Le_m = \frac{k_m}{c_{p_m} D_{v,m} \rho_m}, \tag{100}$$

where k_m is the thermal conductivity, c_{p_m} is the specific heat, $D_{v,m}$ is the diffusion coefficient, and ρ_m is the mixture density in the film region.

The reference Nusselt number Nu_m is obtained from the base Nusselt number Nu_0 and a correction factor F_T:

$$Nu_m = 2 + \frac{Nu_0 - 2}{F_T}. \tag{101}$$

$$F_T = (1 + B_T)^{0.7}\frac{\ln(1 + B_T)}{B_T}. \tag{102}$$

As with the Sherwood number, Nu_0 can be estimated from a Ranz-Marshall type correlation:

$$Nu_0 = \begin{cases} 2 + 0.6 Re_m^{1/2} Pr_m^{1/3}, & \text{if } Re_m \leq 200, \\ 2 + 0.6 Re_m^{1/2} Pr_m^{1/3} + 0.02 Re_m^{0.8} Pr_m^{1/3}, & \text{if } 200 < Re_m \leq 1500, \\ 2 + 0.000045 Re_m^{1.8}, & \text{if } Re_m > 1500, \end{cases} \tag{103}$$

with the Prandtl number $Pr_m = \mu_m c_{p_m} / k_m$.

Assuming h is constant within each time step, the analytical solution of Eq. 93 is given by [69]:

$$T(r,t) = \frac{1}{r} \sum_{n=1}^{\infty} \left\{ \left(I_n - \frac{\sin \lambda_n}{\lambda_n^2} \zeta \right) \frac{\exp\left(-\kappa \lambda_n^2 t\right)}{b_n} - \frac{\sin \lambda_n}{b_n \lambda_n^2} \int_0^t \frac{d\zeta(\tau)}{d\tau} \exp\left(-\kappa \lambda_n^2 (t-\tau)\right) d\tau \right\} \sin(\lambda_n r) + T_{\text{eff}}, \tag{104}$$

with the normalised radial coordinate $r = R/R_d$, and constants:

$$\kappa = \frac{k_l}{c_{p,l} \rho_l R_d^2}, \quad \zeta = \frac{h T_{\text{eff}} R_d}{k_l}, \quad j = \frac{h R_d}{k_l} - 1. \tag{105}$$

$$\lambda \cos \lambda + j \sin \lambda = 0, \quad b_n = \frac{1}{2} \left(1 + \frac{j}{j^2 + \lambda_n^2} \right), \quad I_n = \int_0^1 r T_0(r) \sin(\lambda_n r)\, dr, \tag{106}$$

Here, $T_0(r)$ is the temperature distribution at $t = 0$ or from the previous time step.

While this formulation is strictly valid for stagnant droplets, it can be extended to moving droplets using the effective thermal conductivity k_{eff} introduced by Abramzon and Sirignano [1]:

$$k_{eff} = \chi k_l, \tag{107}$$

$$\chi = 1.86 + 0.86 \tanh\left(2.225 \log \frac{Pe_l}{30}\right), \tag{108}$$

where $Pe_l = Re_l Pr_l$ is the liquid-phase Peclet number, with:

$$Re_l = \frac{2\rho_l R_d U_{s,max}}{\mu_l}, \tag{109}$$

$$Pr_l = \frac{\mu_l c_{pl}}{k_l}, \tag{110}$$

and the maximum surface velocity:

$$U_{s,\max} = \frac{1}{32} |u_i| \frac{\mu_g}{\mu_l} Re_d C_F, \tag{111}$$

$$C_F = \frac{12.69 Re_d^{2/3}}{1 + B_M}. \tag{112}$$

χ transforms k_l into a global heat transfer coefficient k_{eff}, capturing both conduction and internal convection due to droplet motion.

The analytical solution in Eq. 104 was validated experimentally by Starinskaya et al. [77] and computationally by Sazhin et al. [71]. It accurately represents the internal temperature distribution of multicomponent evaporating droplets.

Figure 21, adapted from Abramzon and Sirignano [1], illustrates the non-uniform internal temperature profiles observed in real evaporating droplets. While resolving such detailed thermal gradients requires significant computational resources, the Finite Thermal Conductivity (FTC) model captures this physical behavior with a validated and computationally efficient formulation, making it suitable for use in large-scale spray simulations.

In summary, the ITC model offers a simplified yet computationally efficient approach for droplet heating, while the FTC model, especially with the k_{eff} correction, provides physically consistent predictions for complex, non-uniform heating in multicomponent

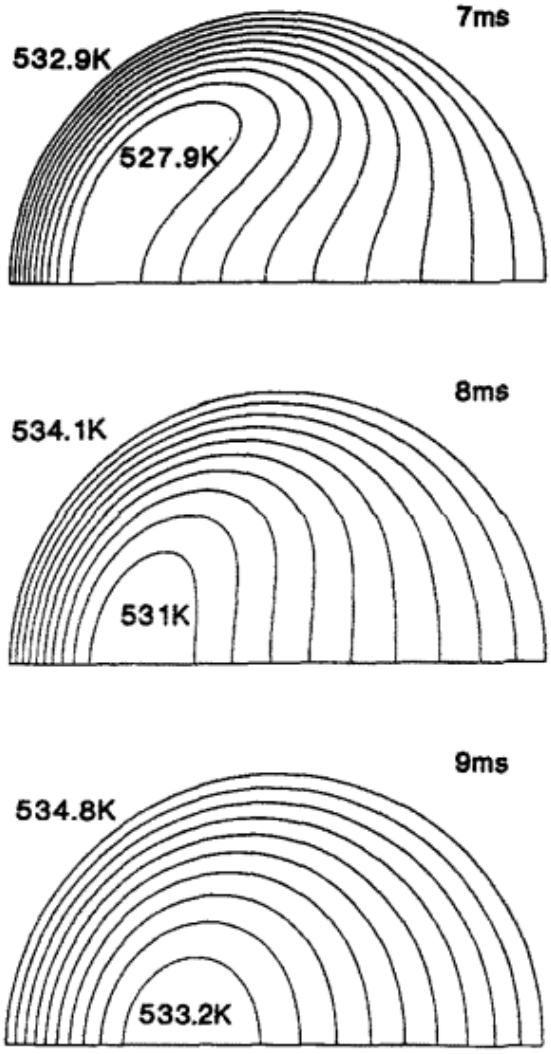

Figure 21: Droplet isotherms illustrating internal temperature gradients. Source: Abramzon et al. [1].

sprays.

The following section discusses diffusion models, which complement the thermal treatment by addressing multicomponent mass transfer mechanisms in the droplet and gas phases.

6.7.2 Diffusion Models

Different approaches are employed to model species diffusion in multicomponent droplet evaporation. These models differ in how they treat internal gradients of mass fractions and species-specific transport phenomena.

The Finite Diffusivity Model assumes that the evaporation rate of each component is governed by its individual diffusivity and the local mass fraction gradient at the droplet surface. In this approach, Fick's law is applied to compute the spatial distribution of species within the droplet, particularly across discretized radial layers. As such, more volatile or more diffusive species tend to evaporate at faster rates, leading to preferential evaporation. This method can capture internal composition gradients more accurately than simplified models.

Pinheiro [61] demonstrated that this approach enables a more detailed resolution of transient mass fraction profiles in multicomponent droplets. The internal evolution of composition within the droplet is calculated by solving the unsteady mass diffusion equation, layer by layer, with boundary conditions informed by the local equilibrium at the droplet surface.

More recently, Effective Diffusivity Models have been proposed to further enhance prediction accuracy. These models incorporate the effects of internal droplet recirculation and thermal gradients on mass transport. The effective diffusivity D_{eff} is defined to represent the combined influence of molecular diffusion and internal convective mixing, which occur due to Marangoni effects and temperature gradients. Starinskaya et al. [77] validated this approach experimentally using ethanol–water mixtures and reported improved agreement with measured species distributions and evaporation rates.

Overall, the choice of diffusion model—whether based on simplified assumptions or detailed formulations—should be guided by the desired balance between computational cost and physical accuracy. While reduced-order models offer robustness and efficiency, only comprehensive multicomponent formulations, such as those proposed by Sazhin and Starinskaya, are capable of capturing the complex species interactions and preferential evaporation effects typical of real spray systems.

6.7.3 Diffusivity Model

Different approaches are employed to model species diffusion in multicomponent droplet evaporation. These models differ in how they treat internal gradients of mass fractions and species-specific transport phenomena.

The Finite Diffusivity Model assumes that the evaporation rate of each component is governed by its individual diffusivity and the local mass fraction gradient at the droplet surface. In this approach, Fick's law is applied to compute the spatial distribution of species within the droplet, particularly across discretized radial layers. As such, more volatile or more diffusive species tend to evaporate at faster rates, leading to preferential evaporation. This method can capture internal composition gradients more accurately than simplified models.

Pinheiro [61] demonstrated that this approach enables a more detailed resolution of transient mass fraction profiles in multicomponent droplets. The internal evolution of composition within the droplet is calculated by solving the unsteady mass diffusion equation, layer by layer, with boundary conditions informed by the local equilibrium at the droplet surface.

More recently, Effective Diffusivity Models have been proposed to further enhance prediction accuracy. These models incorporate the effects of internal droplet recirculation and thermal gradients on mass transport. The effective diffusivity D_{eff} is defined to represent the combined influence of molecular diffusion and internal convective mixing, which occur due to Marangoni effects and temperature gradients. Starinskaya et al. [77] validated this approach experimentally using ethanol–water mixtures and reported improved agreement with measured species distributions and evaporation rates.

Overall, the choice of diffusion model—whether based on simplified assumptions or detailed formulations—should be guided by the desired balance between computational cost and physical accuracy. While reduced-order models offer robustness and efficiency, only comprehensive multicomponent formulations, such as those proposed by Sazhin and Starinskaya, are capable of capturing the complex species interactions and preferential

evaporation effects typical of real spray systems.

In summary, this chapter presented the theoretical framework and numerical models used to describe the behavior of multicomponent evaporating droplets in spray systems. The discussion covered the governing equations, turbulence modeling, droplet dynamics, and heat and mass transfer mechanisms, including thermal conductivity and diffusion models of varying complexity. These models form the foundation upon which the MFSim solver was extended and applied in this research. In the following chapter, the development and implementation of the proposed models are detailed, along with the simulation setups, numerical strategies, and validation procedures that support the findings of this work.

7 Development

This section presents the development and implementation of the numerical models discussed in the previous chapters within the MFSim framework. Building upon the mathematical formulations and physical principles previously established, this phase of the work focuses on adapting, extending, and validating the evaporation models for multicomponent droplets under various conditions. The development process involved software familiarization, model verification through comparison with experimental data, and stepwise integration of advanced thermal and diffusion formulations. Each subsection details the simulations performed, the challenges encountered, and the reasoning behind the methodological decisions that shaped the final implementation strategy.

7.1 Preliminary Simulations

To validate the numerical simulations against experimental observations, a commonly adopted experimental configuration in the literature is the single droplet evaporation test. Experimentally, it consists of suspending a droplet on a fiber and exposing it to well-defined ambient conditions. Based on this experimental setup, droplet evaporation simulations were developed using the conditions presented by Nomura [55], aiming to verify the overall behavior of the numerical model.

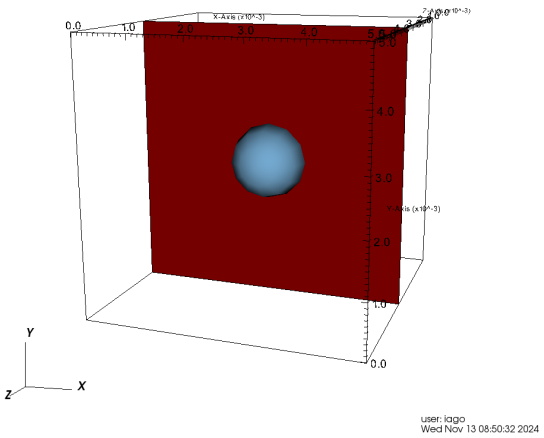

Figure 22: Schematic representation of the single droplet evaporation experiment by Nomura [55].

The first test case reproduced the conditions of the experiment illustrated in Figure 22, originally conducted by Nomura [55]. In that work, several test cases were carried out by varying the ambient gas composition, pressure, and temperature to investigate different evaporation behaviors. For the purposes of initial validation in MFSim, the first four experiments listed in Table 6 were selected; all of them correspond to relatively low-temperature conditions with nitrogen as the ambient gas. Subsequently, the fifth experiment was considered, as it involves droplet evaporation under higher-temperature conditions. The droplet was composed of $d_0 = 700$ μm and an initial temperature of 300 K. The Infinite Thermal Conductivity (ITC) model was employed in this initial phase.

Table 6: Low-temperature single droplet tests based on Nomura [55].

Parameters	1st Case	2nd Case	3rd Case	4th Case	5th Case
Temperature	471K	468K	466K	452K	741K
Pressure	0.1MPa	0.5MPa	1.0MPa	2.0MPa	0.1MPa

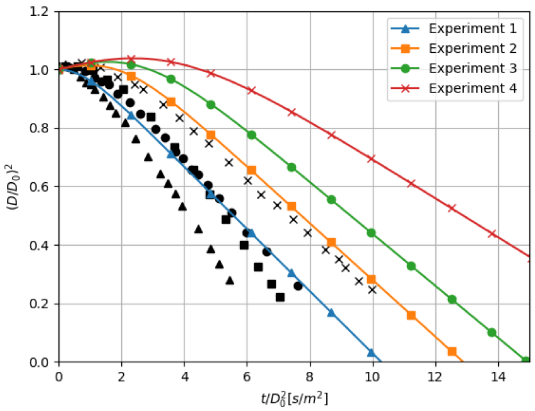

Figure 23: Comparison between numerical results and experimental data from Nomura [55] using the ITC model.

As shown in Figure 23, although the overall behavior was qualitatively consistent with the experimental trend, a noticeable discrepancy was observed in the total evaporation time. This discrepancy indicates that the current modeling assumptions, together with the Infinite Thermal Conductivity (ITC) approach, underestimate the evaporation rate. It demonstrated that this set of assumptions may be too simplistic for accurately capturing the thermal behavior of the droplet, especially under the tested conditions. Therefore, the use of more detailed thermal models becomes necessary to improve the predictive capability of the simulation.

Before analyzing more advanced evaporation models, preliminary simulations were carried out to explore the influence of droplet velocity. The objective was to verify the consistency of the well-known physical behavior in which droplets moving through dry air at higher relative velocities tend to evaporate more rapidly. The relative velocity between the droplet and the surrounding gas, commonly referred to as "slip velocity" is used to compute the Reynolds number, which in turn directly influences the evaporation rate through the modified Sherwood number (Sh_m).

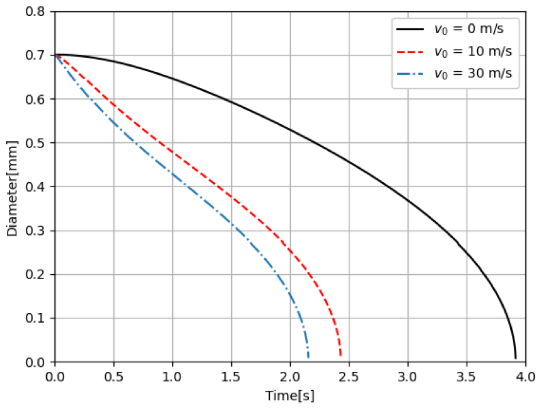

Figure 24: Effect of relative velocity on droplet evaporation.

The results qualitatively confirmed that higher slip velocities lead to faster evaporation rates. Another observed phenomenon was the droplet deceleration due to diameter reduction, which decreases the Stokes number and results in reduced slip velocity in quiescent conditions.

To improve the physical accuracy of the simulations, Tonini [81], and later Pinheiro [61], emphasized the importance of incorporating the Effective Thermal Conductivity (ETC) model when analyzing moving droplets. In the present case, no quantitative validation against experimental or benchmark data was performed—only a qualitative assessment of the droplet behavior was conducted.

7.2 Thermal Conductivity Model

Following the initial tests, a comparison was carried out between the Infinite Thermal Conductivity (ITC) and Finite Thermal Conductivity (FTC) models. The goal was to assess how thermal conduction assumptions inside the droplet affect the evaporation dynamics, particularly in environments where the ambient temperature is higher than the droplet's initial temperature.

Both cases studied in Figures 25 and 26 refer to the experiments detailed in Table 6. Analysing Figure 25, it's possible to understand that in this case of a heptane droplet evaporating in Nitrogen, the assumption of Unity-Lewis brought a higher evaporation rate

due to the diffusivity coefficient.

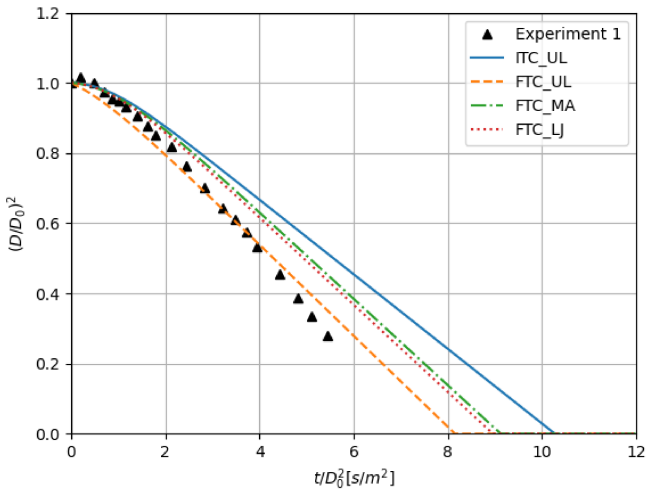

Figure 25: Comparison between ITC and FTC models in Nomura's experiment 1 (see Table 6), using different transport models: Unity-Lewis (UL), Mixture-Averaged (MA), and Lennard-Jones (LJ). The FTC model assumes 100 discretized layers within the droplet.

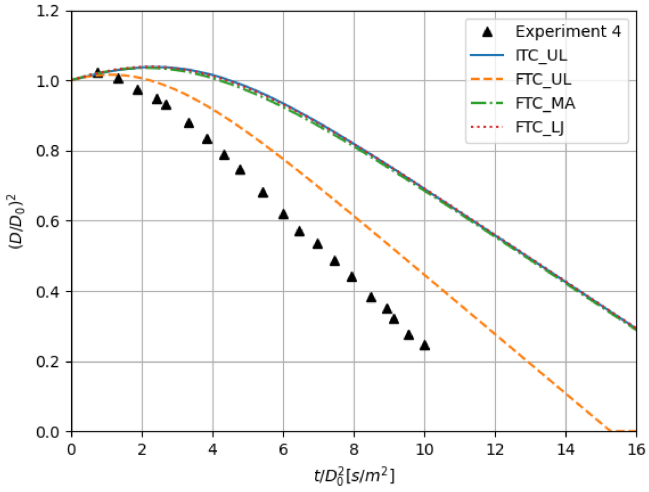

Figure 26: Comparison between ITC and FTC models in Nomura's experiment 4 (see Table 6), using different transport models: Unity-Lewis (UL), Mixture-Averaged (MA), and Lennard-Jones (LJ). The FTC model assumes 100 discretized layers within the droplet.

By this conclusion in Figure 25, another conclusion can be made in Figure 26, the FTC model predicts a higher evaporation rate than the ITC model. This behavior is expected due to the presence of a temperature gradient within the droplet: the outer regions, being in direct contact with the hotter surrounding gas, reach higher temperatures more quickly, thereby accelerating the evaporation process.

Figure 26 presents both experimental and numerical results for a high-pressure condition (2.0 MPa). Under these conditions, *n*-heptane approaches or enters its supercritical regime, where non-ideal thermophysical behavior becomes significant due to the absence of a distinct liquid–vapor interface. This case underscores the importance of further investigation into droplet evaporation under supercritical conditions. Preliminary tests were conducted using the Redlich–Kwong equation of state; however, due to the lack of reliable data for the liquid-phase properties at such elevated pressures, the accuracy of these simulations could not be validated. Since the thermophysical behavior of the liquid phase is also affected—not just that of the gas—the results were omitted from this study. Consequently, this topic remains outside the scope of the present work and is reserved for future exploration.

It is also important to note that Pinheiro [61] discusses the number of terms used in the series expansions of $T(r,t)$ and $Y_l(r,t)$ for solving the internal energy and species equations in the FTC model. She recommends using 20 terms in each series as a compromise between numerical accuracy and computational efficiency. However, tests conducted in this work showed that for droplets with velocities exceeding 20 m/s, a greater number of terms such as 30 for both temperature and species expansions may be required to maintain stability and accuracy. This highlights the need for a case-by-case analysis when simulating high-speed droplets. In the present study, 100 discretized layers were adopted as the default resolution for the FTC model to ensure robustness across different scenarios. Any deviations from this default setting are explicitly indicated when applicable.

7.2.1 FTC or ITC

Sazhin [70] stated that the internal temperature gradient within a droplet can be neglected—thereby justifying the Infinite Thermal Conductivity (ITC) assumption—if the following condition is satisfied:

$$t_p \gg R_d^2/k_l, \tag{113}$$

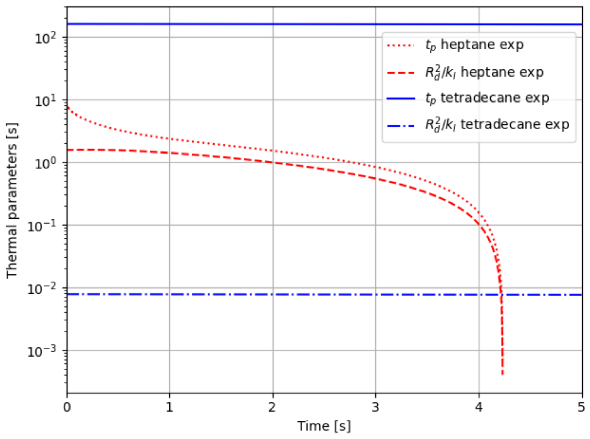

Figure 27: Thermal parameter analysis for the n-heptane experiment by Nomura and the n-tetradecane experiment by Wilm.

where t_p is the characteristic time of the evaporation process, and the inequality is only valid if $k_l \gg k_g$. The corresponding thermal diffusivities for the liquid and gas phases are defined as:

$$\kappa_l = \frac{k_l}{cp_l \rho_l}, \quad \kappa_g = \frac{k_g}{cp_g \rho_g}. \tag{114}$$

Figure 27 illustrates the analysis of these thermal parameters for two reference cases. The tetradecane droplet experiment conducted by Wilm, which will be discussed in a subsequent section, exhibited a total evaporation time of approximately 200 seconds. In contrast, the n-heptane experiment reported by Nomura [55] reached full evaporation in about 4 seconds. Given that the characteristic time t_p is much larger than R_d^2/k_l in the tetradecane case, it is reasonable to apply the ITC assumption, as done by Tonini [81]. Conversely, in cases like Nomura's [55], where shorter timescales are involved, the Finite Thermal Conductivity (FTC) model becomes necessary to capture the internal temperature evolution more accurately.

To assess the impact on computational cost, processing times were analyzed. Tests showed that applying the FTC model with 100 layers resulted in a 4.5% increase in simulation time. When combining FTC with finite diffusion (FD), the processing time increased by approximately 11.6%. These benchmarks were based on the simulation of the Wilms experiment case. It is important to note that these results reflect not only the

Lagrangian framework—since the scenario involves stationary (non-moving) droplets—but also include the solution of other modules within the simulation.

These results reinforce the importance of selecting the appropriate thermal conductivity model based on characteristic process times. Specifically, simulations of short-lived droplets, such as those in Nomura's study [55], justify the use of FTC, while cases involving long evaporation durations, such as those in Wilm's work [89], support the application of ITC.

7.2.2 FTC Layers analysis to Computational Cost Reduction

To reduce the computational cost associated with the Finite Thermal Conductivity (FTC) model, simulations were performed using different numbers of discretized layers inside the droplet. Figure 28 shows that when the number of layers falls below a certain convergence threshold, the solution diverges or becomes unstable. In contrast, as shown in Figure 29, simulations with ten or more layers yielded results that were nearly identical to those obtained using 100 layers, under the same conditions.

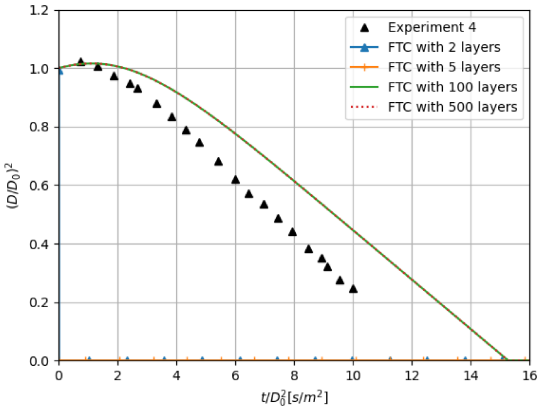

Figure 28: Layers analysis divergence all used UL.

These findings demonstrate that it is possible to significantly reduce computational cost by using fewer layers—such as 10 instead of 100—without compromising accuracy, provided that convergence is verified for the specific case under consideration.

It is important to note that the idea of optimizing resource usage was considered in light of Gerard's software engineering guidelines [35], which outline ten rules for devel-

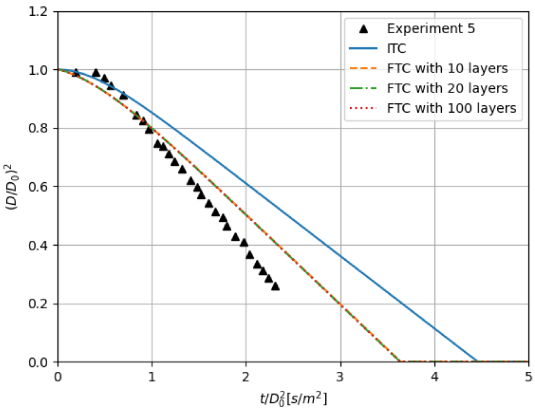

Figure 29: Layers analysis convergence.

oping reliable and maintainable scientific codes. Specifically, the third rule "Do not use dynamic memory allocation after initialization" was a critical constraint. Although dynamic memory allocation could theoretically allow for adaptive refinement based on runtime conditions, it poses risks such as memory leaks or instability when implemented in low-level languages, as is the case with MFSim. Consequently, this optimization strategy was not adopted.

7.3 Radiation

As previously discussed, Nomura [55] conducted experiments on single n-heptane droplets, evaluating the effects of temperature and pressure on evaporation behavior. Kitano [40] introduced a radiation term modeled as a heat sink, which interacts directly with the energy of the mesh element where the droplet is located. The radiative heat transfer is governed by the Stefan–Boltzmann law, with σ_{sb} being the Stefan–Boltzmann constant and ϵ_{sa} the surface absorptance, typically set to 0.93 depending on the substance [92].

$$Q_{rad} = \pi D_p^2 \sigma_{sb} \epsilon_{sa} (T_g^4 - T_d^4), \tag{115}$$

$$Q_s = G\pi D_d N u_m k_m (T_g - T_d) - L_v \dot{m}_d + \pi d_d^2 \sigma_{sb} \epsilon_{sa} (T_g^4 - T_d^4). \tag{116}$$

Figure 30 illustrates the effect of including the radiation term in high-temperature evaporation conditions, using experimental data from Nomura's experiment 5 [55] seen in Table 6. The inclusion of radiation had a more pronounced impact on the evaporation rate than the choice of transport model alone, especially at elevated ambient temperatures.

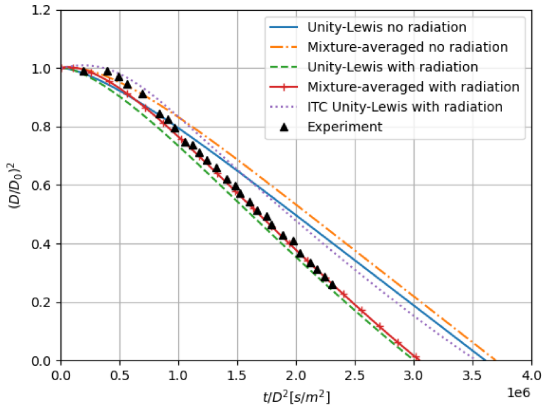

Figure 30: kitano high temperature experiment 5 seen in Table 6 comparison considering radiation term.

These results demonstrate that radiation is a critical component in evaporation modeling under high-temperature conditions. Moreover, the thermal imbalance between the environment and the initial droplet temperature further supports the use of the Finite Thermal Conductivity (FTC) model to resolve internal temperature gradients.

7.4 Transport Model Analysis

Wilms [89] conducted an experiment involving the evaporation of a hexadecane droplet at ambient temperature. Due to the formulation of the radiation term proposed by Kitano [40], radiation effects in this case are negligible. As a result, this configuration provides an ideal opportunity to isolate and analyze the role of diffusion and transport models, with minimal interference from radiative heat transfer. Additionally, the simulations presented in Figures 31 and 32 assume the Infinite Thermal Conductivity (ITC) model, based on the process time criterion discussed earlier and illustrated in Figure 27.

In this case, the droplet evaporates at an ambient temperature of 304 K, resulting in relatively small internal temperature gradients. Consequently, the droplet can be consid-

ered isothermal throughout the process.

As explained in Section 5, there are several diffusion models available, and an inappropriate choice can significantly compromise the accuracy of evaporation simulations. Therefore, tests were conducted to evaluate the applicability and performance of different transport models under controlled conditions.

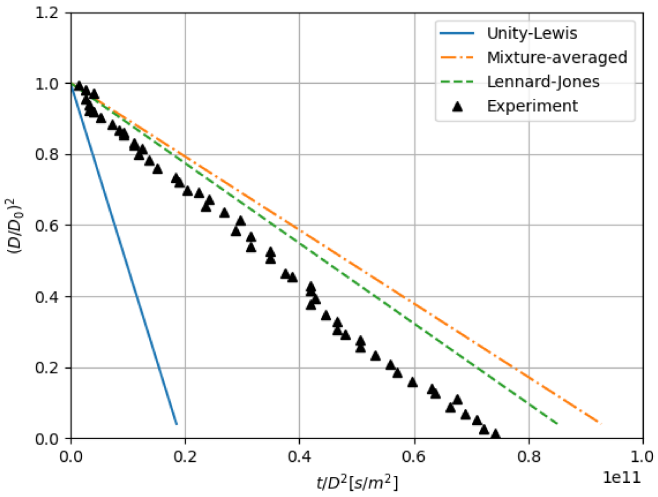

Figure 31: Simulation of the tetradecane evaporation experiment at 1.0 atm and 304 K, based on Wilms [89].

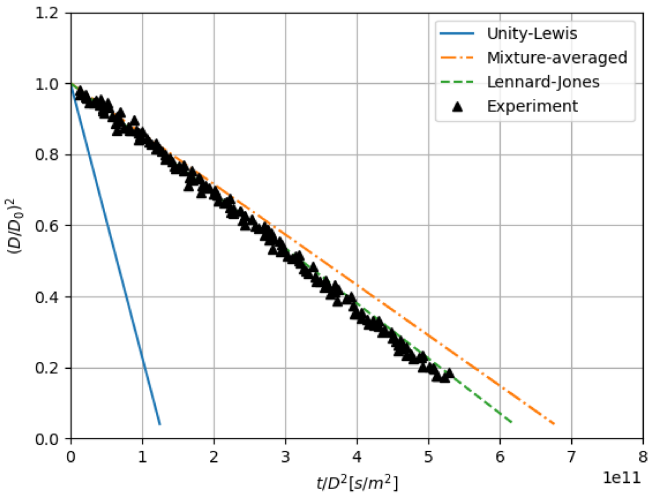

Figure 32: Simulation of the hexadecane evaporation experiment at 1.0 atm and 304 K, based on Wilms [89].

Figures 31 and 32 show that the Mixture-Averaged and Lennard-Jones transport models produced simulation results that closely matched the experimental data presented by

Wilms [89]. In contrast, the Unity-Lewis model exhibited a larger deviation from the observed behavior. Among the models tested, the Lennard-Jones approach provided the highest accuracy in representing the diffusion-driven evaporation dynamics.

The discrepancy observed in the Unity-Lewis evaporation time arises from an overestimation of the diffusivity coefficients for both hydrocarbons. This model assumes a constant Lewis number ($Le = 1$), effectively balancing the diffusivities of all species in the mixture. As a result, the diffusivity of nitrogen is underestimated while the diffusivities of the hydrocarbon components are overestimated. This misrepresentation leads to accelerated evaporation rates for the fuel components. The findings reinforce the necessity of incorporating the radiation term in the energy balance, as it captures the combined effects of transport and thermal gradients—especially under conditions where radiative heat transfer significantly influences evaporation dynamics.

7.5 Condensation Model

Ding et al. [24] proposed a condensation model for Lagrangian droplets based on heat transfer principles and surface thermodynamics. In this approach, the mass transfer rate is determined by the evolution of the droplet radius, accounting for the temperature difference between the droplet and the vapor phase, and for the surface curvature effect through the critical radius.

The mass transfer rate due to condensation or evaporation, $\dot{m}$, is computed as:

$$\dot{m} = A_p \rho_p \frac{dR_d}{dt}, \tag{117}$$

where A_p is the droplet surface area, ρ_p is the droplet density, and, $\frac{dr_p}{dt}$ is the growth rate of the droplet radius. The radius growth rate is given by:

$$\frac{dR_d}{dt} = \sum_{i=k}^{2} \nu_k \frac{(T_r - T_v)}{\rho_p h_v}, \tag{118}$$

where ν_i is the heat transfer coefficient for species i, T_r is the temperature at the droplet

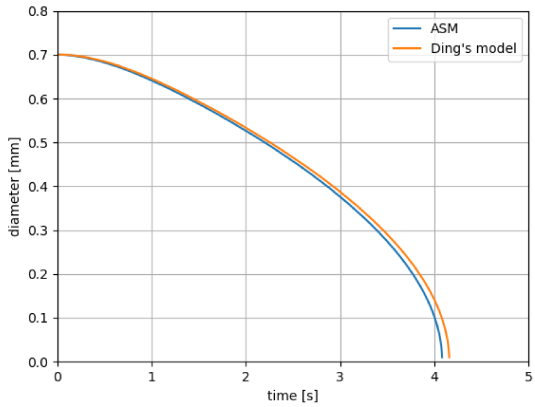

Figure 33: ASM comparison to Ding's model.

surface, T_v is the vapor temperature, and h_v is the latent heat of vaporization.

The main differences between the evaporation model adopted in this research and that proposed by Ding et al. [24] lie in the treatment of Stefan flow and the use of the Spalding number. While the present work assumes quasi-steady diffusion with vapor-gas coupling through the Spalding formulation, Ding's model evaluates the droplet surface temperature using a relation that lies conceptually between the Infinite and Finite Thermal Conductivity models. Additionally, instead of employing Wilke's averaging rule, commonly used in spray evaporation models to compute interfacial properties, Ding's formulation adopts a different approach for estimating the droplet surface temperature.

The droplet surface temperature T_r is computed as:

$$T_s = T_{av} - \frac{r_c}{R_d}(T_{av} - T_g) \tag{119}$$

with the critical radius for nucleation given by:

$$r_c = \frac{2\sigma}{\rho_p R_v T_v \ln(S_s)} \tag{120}$$

where σ is the surface tension, R_v is the vapor gas constant, and S_s is the supersaturation ratio.

Although this model provides a physically consistent framework for condensation phe-

nomena, its application within the MFSim environment revealed significant discrepancies. In particular, when tested under equilibrium conditions—where evaporation and condensation rates are expected to be comparable. The condensation rate predicted by Ding's model was found to be three orders of magnitude higher than the evaporation rate computed using MFSim's original model.

The observed discrepancy emphasizes the importance of using consistent formulations for condensation and evaporation. In equilibrium, the vapor mass fraction in the ambient ($Y_{v,g}$) approaches the saturation value at the droplet surface ($Y_{v,s}$), leading to $B_M \to 0$ and $\dot{m}_d \to 0$. This balance is intrinsic to MFSim's model but not inherently guaranteed in Ding's formulation.

Therefore, although Ding's model was implemented and tested, it was not adopted in the final version of MFSim due to its inconsistency with mass balance under equilibrium conditions. This analysis underscores the need for careful validation when integrating heterogeneous models into a unified multiphase simulation framework.

7.6 Multicomponent Evaporation Model and Differential Diffusion

Multicomponent evaporation in sprays poses a significant modeling challenge. The various components in the liquid phase do not evaporate at uniform rates; instead, phenomena such as differential and preferential diffusion play critical roles. If not properly accounted for, the lighter components may fully evaporate before the droplet reaches its intended target, thereby compromising the system's behavior and predictability.

Extending the algorithm to handle multicomponent evaporation was a nontrivial task. Before this implementation, the treatment of gaseous and liquid species was decoupled, with gaseous components being defined prior to the liquid ones. Furthermore, the simulation framework adopted a non-condensation assumption, meaning that liquid-phase components should not reappear in the gas phase. A major part of this development involved redefining parameter calculations and identifying which parts of the algorithm

required generalization and which did not. As a result of this restructuring, all components are now allowed to both evaporate and condense, enabling a more physically consistent representation of phase-change dynamics in multicomponent systems.

The literature offers several approaches for multicomponent evaporation. For instance, Chen [12] investigated three distinct models: the well-mixed (WM) model, the frozen evaporation (FZ) model, and the diffusion-controlled (DC) model. His findings suggest that the well-mixed model is generally more suitable for predicting evaporation behavior at injection pressures around 0.3 MPa.

In this work, the models proposed by Tonini and Cossali, and by Sacomano, were selected for detailed implementation and evaluation. The choice was based on their compatibility with the assumptions adopted in MFSim and their broad recognition in the field of spray modeling.

7.6.1 Tonini and Cossali Model

Tonini and Cossali [81], a widely recognized reference in spray modeling, analyzed four different models of multicomponent droplet evaporation and validated them against experimental data from Wilms [89]. The most accurate model was based on the formulation originally proposed by Sazhin [71] for bi-component droplets, which Tonini extended and simplified. Notably, the Tonini and Cossali model is derived from a modified version of the classical Abramzon–Sirignano model (ASM), which had already been implemented in MFSim. This shared foundation ensured compatibility with the numerical structure of the code. Due to this alignment and the model's strong acceptance within the spray research community, the Tonini and Cossali formulation was selected for implementation in this work and further extended to more complex multicomponent cases.

The Spalding number B_M is calculated as:

$$B_M = \frac{\sum_k Y_{v,k_s} - \sum_k Y_{v,k_g}}{1 - \sum_k Y_{v,k_s}}, \tag{121}$$

The diffusion coefficient of the vapor mixture is obtained using molar fractions:

$$D_{v,m} = \frac{\sum_k Y_{v,k_m} D_{k,m}}{\sum_k Y_{v,k_m}}. \tag{122}$$

Tonini and Cossali [81] adopt Wilke's rule to estimate mixture properties, referencing Yuen [96]. The overall mass evaporation rate is computed without explicitly including a Sherwood number, under the assumption that the droplet remains stationary during evaporation. In such cases, the Sherwood number approaches a constant value of 2. Although the Sherwood number is not used directly in the equation, it is discussed in Tonini's original work. The mass evaporation rate is expressed as:

$$\dot{m} = 4\pi R_d \rho_m D_{v,m} \ln\left(1 + B_M\right). \tag{123}$$

The fractional evaporation rate of each component ε_k is calculated by:

$$\varepsilon_k = \frac{Y_{v,k_s} - Y_{v,k_g} e^{\left(-\frac{\dot{m}}{4\pi\rho_v R_d D_{k,m}}\right)}}{1 - e^{\left(-\frac{\dot{m}}{4\pi\rho_v R_d D_{k,m}}\right)}}. \tag{124}$$

The boundary conditions applied are:

$$Pv_k(r = R_0) = Pv_k(\zeta = 1) = Pv_{s,k},$$

$$Y_k(r = \infty) = Y_k(\zeta = 0) = Y_{k,g}. \tag{125}$$

In summary, the Tonini and Cossali model provides a simplified yet physically grounded approach to multicomponent droplet evaporation, aligning well with the assumptions and numerical requirements of the present study. Its implementation in MFSim enables the simulation of complex spray dynamics with reasonable accuracy and stability. However, since this model does not explicitly account for condensation effects, which may arise in high-humidity environments or during transient cooling, an additional model capable of

handling condensation phenomena was also investigated to ensure broader applicability and improved physical consistency in such scenarios.

7.6.2 Sacomano Model

Sacomano [28] investigated three multicomponent evaporation models, one of which is detailed in [29] and serves as the basis for the present implementation. The selected model assumes Infinite Thermal Conductivity (ITC), and differs from previous models in several key formulations, starting with the following dimensionless numbers. Notably, unlike the Tonini and Cossali model, the formulation proposed by Sacomano explicitly accounts for condensation, making it particularly suitable for scenarios involving supersaturated environments or transient cooling near the droplet surface.

Sacomano's model differs from the Tonini and Cossali model (TCM) by requiring an additional computational step, similar to the approach described by Zhang and Kong [97]. This step involves solving a nonlinear system to simultaneously compute the total evaporation rate $\dot{m}$ and the fractional mass evaporation rates ε_k for each component.

$$Nu_0 = \begin{cases} 1 + (1 + RePr)^{1/3}, & \text{if } Re \leq 1, \\ 1 + (1 + RePr)^{1/3} Re^{0.077}, & \text{if } Re > 1, \end{cases} \tag{126}$$

$$Sh_0^k = \begin{cases} 1 + (1 + ReSc_k)^{1/3}, & \text{if } Re_m \leq 1, \\ 1 + (1 + ReSc_k)^{1/3} + Re^{0.077}, & \text{if } Re_m > 1. \end{cases} \tag{127}$$

To account for the influence of each individual component in multicomponent systems, Sacomano [29] proposed using species-dependent properties, enabling the model to handle a wide range of environmental conditions, including those with high concentrations of condensable species. The Schmidt and Sherwood numbers for each component k are defined as:

$$Sc_k = \frac{\mu}{\rho D_k}, \tag{128}$$

$$Sh_k = \frac{\ln|B_{M,k}+1|}{B_{M,k}} Sh_k^0, \tag{129}$$

The species-specific Spalding number is given by:

$$B_{M_k} = \frac{Y_{k,s} - Y_{k,g}}{\varepsilon_k - Y_{k,s}}, \tag{130}$$

Although the formulation resembles traditional Spalding expressions, the distinction lies in computing $B_{M,k}$ for each species individually. The total mass evaporation rate is:

$$\dot{m} = 4\pi R_d \rho_m D_{k,m} \ln|1 + B_{M_k}|, \tag{131}$$

and when convective effects are included:

$$\dot{m} = 2\pi R_d \rho_m D_{k,m} Sh_k B_{M_k}, \tag{132}$$

Sacomano [28] explains that if all participating species diffusivity is simplified to the same value $B_{M,k} = B_M$. Therefore, the calculus for ε_k is straightforward:

$$\varepsilon_k = \frac{\dot{m}_k}{\dot{m}} \tag{133}$$

The equations 130, 131 and 133, depends on each other. It means that an equation system must be solved to define the evaporation rate of each component. Due to promising results, but a high complexity, a simplified version of this expression was tested and the results was close to experiments. It led to the implementation with this simplification:

$$B_{M_k} = \frac{Y_{k,s} - Y_{k,g}}{1 - Y_{k,s}}. \tag{134}$$

It helps reduce the computational cost, as no solver is required. However, it also introduces limitations in the accuracy of the model, as it suppresses differential diffusion

effects. These effects can become significant under specific conditions-such as when the evaporating species exhibit considerable differences in thermophysical properties, or when simultaneous evaporation and condensation of different species occur. In such scenarios, the simplified model may lead to less reliable predictions of mass transfer dynamics.

To evaluate multicomponent diffusivities, Sacomano employs Blanc's law [9], given by:

$$D_k = \left(\sum_{\substack{j=0 \\ j \neq k}}^{n} \frac{X_{j,m}}{D'_{k,j}} \right)^{-1} , \tag{135}$$

The binary diffusion coefficients $D'_{k,j}$ are based on data from Marrero and Mason [48]. Although $D'_{k,j}$ slightly differs from the standard binary diffusivity $D_{k,j}$, the approximation $D'_{k,j} \approx D_{k,j}$ is commonly accepted. Some studies express Eq. (135) using mass fractions Y_j instead of mole fractions X_j, as done by Tonini [81], which was considered in this research.

The model developed by Coffee and Heimerl [14] is an alternative formulation validated and suggested by Sacomano:

$$D_{k,m} = (1 - X_k) \left(\sum_{\substack{j=0 \\ j \neq k}}^{n} \frac{X_{j,m}}{D_{k,j}} \right)^{-1} , \tag{136}$$

With the implementation of the Sacomano model, the development of the mathematical framework for multicomponent droplet evaporation in MFSim was concluded. To ensure the fluid dynamic model was physically consistent, it became necessary to refine the pressure–velocity coupling strategy. This led to the implementation of a mass-source-corrected PISO algorithm, which explicitly accounts for mass exchange due to phase change. While the previous subsections focused on the formulation of evaporation and condensation models, this section addresses a critical numerical enhancement needed to preserve local mass conservation.

7.7 Incorporation of Mass Source Term in Pressure Correction (PISO)

To develop a more consistent fluid dynamic model, the PISO algorithm was implemented to achieve segregated pressure–velocity coupling, which had been previously lacking. Starting from the continuity equation:

$$\frac{\partial \rho}{\partial t} + \nabla \cdot (\rho \mathbf{u}) = 0, \tag{137}$$

as presented by [58].

By integrating over the control volume and discretizing in time and space, the pressure correction equation without mass sources is obtained:

$$\frac{\rho_P^{n+1} - \rho_P^n}{\Delta t} \Delta V + \sum_f (\rho \mathbf{u} \cdot \mathbf{n})_f \, \Delta A_f = 0, \tag{138}$$

as shown by Harlow and Amsden [34].

When introducing a mass source term S_m (in kg/m^3·s) into each control volume, Eq. (138) generalizes to:

$$\frac{\rho_P^{n+1} - \rho_P^n}{\Delta t} \Delta V + \sum_f (\rho \mathbf{u} \cdot \mathbf{n})_f \, \Delta A_f = S_m \, \Delta V. \tag{139}$$

To close the system, a linearized equation of state is applied between the estimated step ($*$) and the corrected step (no superscript), as follows:

$$p = \rho R T - p_\infty, \tag{140a}$$

$$p^* = \rho^* R T - p_\infty, \tag{140b}$$

which yields the pressure correction:

$$p' = p - p^* = \rho' RT, \quad \Longrightarrow \quad \rho' = \frac{p'}{RT}, \tag{141}$$

as noted in [58].

At the faces of the control volume, the density correction ρ' is interpolated using a weight kernel (γ_f), for example:

$$\rho'_e = \left(\tfrac{1}{2} + \gamma_e\right)\frac{p'_P}{RT_P} + \left(\tfrac{1}{2} - \gamma_e\right)\frac{p'_E}{RT_E}, \tag{142}$$

and similarly for other faces [58].

Substituting $\rho' = p'/(RT)$ and the face corrections into Eq. (139), the terms are reorganized into a linear system in Poisson form for p':

$$A_P p'_P + \sum_{\text{nb}} A_{\text{nb}}\, p'_{\text{nb}} = Q_P + S_m\, \Delta V, \tag{143}$$

as established in [80].

Finally, the PISO method updates the velocity field using the pressure correction:

$$\mathbf{u}^{n+1} = \mathbf{u}^* - \frac{1}{A_P}\nabla p', \tag{144}$$

In summary, the developments presented in this chapter conclude the core implementation of the multicomponent evaporation framework in MFSim. Special attention was given not only to the physical modeling of droplet heating, phase change, and differential diffusion, but also to the numerical strategies required to ensure solution stability and physical consistency. Among these strategies, the correction of the pressure field using the PISO algorithm with explicit mass source terms plays a central role. This correction guarantees that the divergence of the velocity field matches exactly the mass source term S_m, thereby enforcing local mass conservation. By translating the effects of evaporation and condensation into the pressure equation, this approach preserves the stability and

consistency of the pressure–velocity coupling.

The following chapters shift focus toward model usability enhancements, notably the integration of external thermophysical property databases. These additions aim to streamline the simulation setup, reduce manual input requirements, and minimize the potential for user-induced errors. It is important to note that the chronological order of implementation did not necessarily mirror the structure adopted in this document. Instead, the content has been organized thematically to convey a clearer and more coherent progression of the modeling concepts.

7.8 Fluid Properties Databases

Accurate thermophysical properties are essential for evaluating droplet evaporation rates, especially in multicomponent systems. While the gas-phase properties were readily available through the Cantera library, the liquid-phase initially lacked an integrated database, requiring manual input of correlation coefficients from the literature. This section presents the efforts made to automate and enhance the retrieval of liquid-phase properties, aiming to improve reproducibility, reduce setup time, and minimize input errors. Several database alternatives were tested, and a final implementation based on Yaws' comprehensive dataset was adopted.

As already mentioned, for the gaseous phase, thermophysical properties were obtained using the Cantera library. However, the liquid phase initially lacked an integrated database. To overcome this, liquid properties were calculated using correlations from Yaws [95, 93], which also incur low computational cost but require manual data entry. This approach is time-consuming and prone to human error, as it relies on extracting and inputting coefficients directly from the printed literature.

The following equations were employed for the evaluation of liquid properties:

$$\rho_l(T) = 1000 A_\rho B_\rho^{-(1-\frac{T}{T_{crit}})C_\rho}. \tag{145}$$

$$\mu_l(T) = 0.001 * 10^{\mu_A + \frac{\mu_B}{T} + \mu_C T + \mu_D T^2}. \tag{146}$$

$$k_l(T) = k_A + k_B T + k_C T^2. \tag{147}$$

$$cp_l(T) = \frac{1000}{M(n)}(cp_A + cp_B T + cp_C T^2 + cp_D T^3). \tag{148}$$

$$L = \frac{L_A(1 - T/T_{crit})^{L_B}}{M(n)} \times 10^6. \tag{149}$$

$$Vp_{sat} = 10^{Vp_A - \frac{Vp_B}{T} + Vp_C \log_{10} T + Vp_D T + Vp_E T^2} \times 133.32. \tag{150}$$

Here, ρ_l is the density [kg/m^3], μ_l the dynamic viscosity [Pa·s], k_l the thermal conductivity [W/m·K], cp_l the specific heat [J/kg·K], L the latent heat [J/kg], and Vp_{sat} the saturation vapor pressure [Pa]. $M(n)$ represents the molar mass of each component. An example of component data used for Jet A-1 surrogate is presented in Table 7, based on Pinheiro [62].

Due to the potential for transcription errors and the setup time required, the CoolProp database was tested as an alternative. CoolProp provides access to thermophysical data for 122 pure and pseudo-components and allows automatic property retrieval based on the fluid name. However, the database lacks several heavy hydrocarbons commonly used in Jet A-1 surrogate. Furthermore, its use resulted in a 4–6% increase in process simulation time for single-component droplet evaporation, as shown in Figure 34.

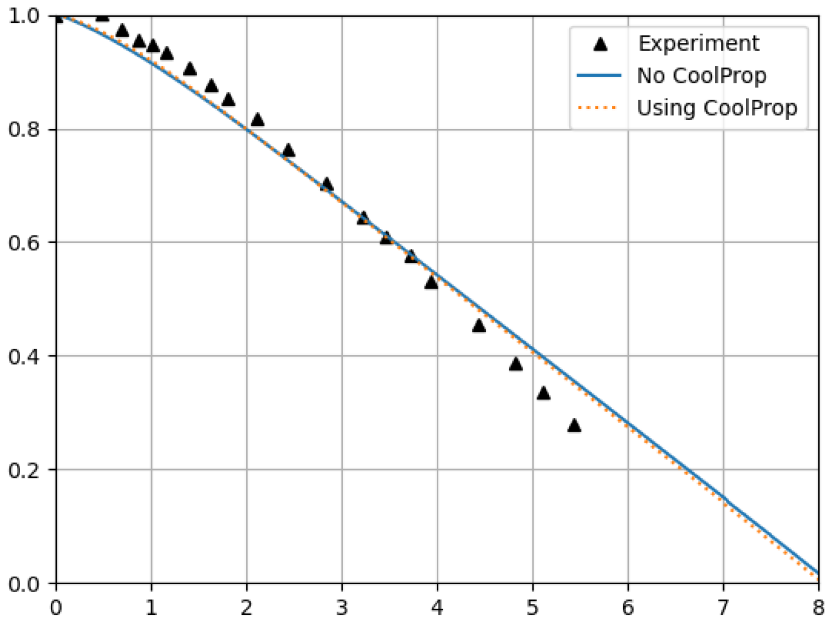

Figure 34: Evaporation time comparison using Yaws-based correlations and CoolProp.

To overcome these limitations, a new internal database was implemented using the Yaws property tables. This version supports over 5000 organic and inorganic compounds and allows automatic replacement of coefficients at runtime, eliminating the need for manual input while maintaining computational efficiency.

The finalized Yaws-based database significantly reduced input preparation time and minimized the risk of human error. It is accessible in its complete form at [94].

Table 7: Components' coefficients from Jet A-1.

Coef	C7H8	NC8H18	IC8H18	C9H12-2	NC10H22	NC12H26	IC12H26	NC14H30	NC16H34
T_{crit}	591.79	568.70	559.64	637.36	617.70	658.00	650.75	693.00	723.00
P_{crit}	41.08	24.90	24.84	32.10	21.10	18.20	19.79	15.70	14.00
ρ_A	0.2918	0.2322	0.2341	0.2776	0.2359	0.2344	0.2428	0.2354	0.2435
ρ_B	0.2619	0.2602	0.2620	0.2591	0.2567	0.2523	0.2539	0.2556	0.2545
ρ_C	0.2989	0.2694	0.2713	0.2798	0.2857	0.2896	0.2857	0.2735	0.3238
Cp_A	83.70	82.74	134.97	83.64	79.74	84.49	213.73	111.81	89.10
Cp_B	0.5167	1.3043	0.8146	0.8786	1.6926	2.0358	1.0747	2.2092	2.7062
Cp_C	-0.0015	-0.0038	-0.0025	-0.0023	-0.0045	-0.0051	-0.0028	-0.0053	-0.0061
Cp_D	2e-6	5e-6	4e-6	3e-6	5e-6	5e-6	3e-6	5e-6	6e-6
k_A	0.2099	0.2229	0.1900	0.1945	0.2218	0.2292	0.1938	0.1956	0.1996
k_B	-0.0003	-0.0003	-0.0003	-0.0002	-0.0003	-0.0004	-0.0003	-0.0002	-0.0002
k_C	3e-8	5e-8	0.00	0.00	1e-7	2e-7	0.00	0.0000	0.00
μ_A	-5.64	-5.92	-4.86	-4.83	-6.07	-7.07	-4.61	-7.87	-8.19
μ_B	910.54	888.09	715.64	832.75	1017.7	1253.0	827.75	1446.7	1557.1
μ_C	0.0109	0.0130	0.0108	0.0089	0.0122	0.0137	0.0079	0.0149	0.0153
μ_D	-0.00001	-0.00001	-0.00001	-0.00001	-0.00001	-0.00001	-0.000007	-0.000012	-0.000012
Lv_A	50.14	59.08	59.50	60.07	71.43	77.17	70.78	86.89	96.68
Lv_B	0.383	0.439	0.481	0.365	0.451	0.407	0.380	0.418	0.422
Vp_A	7.14	7.14	7.13	7.26	7.22	7.23	7.04	7.26	7.36
Vp_B	1457.29	1498.96	1473.84	1695.83	1693.93	1807.47	1632.18	1914.86	2094.08
Vp_C	231.83	225.87	229.44	222.42	216.46	199.38	181.83	183.52	180.41

8 Results and Discussion

The results after analysing and implementing all the components models are divided in the validation of multicomponent models and two industrial cases referring to Petrobras Atmospheric Distillation Towers.

In all simulations, the mesh were discretized to have a aspect ratio of 1, it means that the mesh is cubic. Therefore, only the quantity and only one mesh dimension will be mentioned. The main boundary conditions are described for each simulation. The eulerian transport model assumed is unity-lewis.

8.1 Tonini and Cossali Model Validation

To validate the model, the experimental configuration presented by Wilms [89] was simulated using the Tonini and Cossali [81] equations. The experiment consisted of monitoring the evaporation time of isolated, stationary droplets suspended in quiescent air under ambient temperature and pressure. Due to the negligible temperature gradients within the droplet under such conditions, the Infinite Thermal Conductivity (ITC) assumption was considered valid.

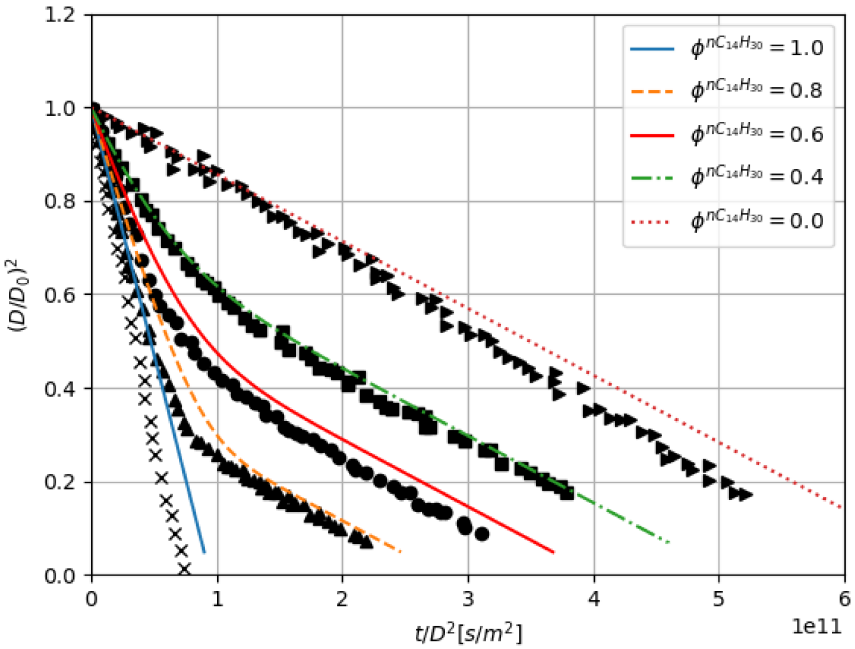

Figure 35: Comparison between the TCM and experimental data from Wilms [89].

Once the model was validated, the Lennard–Jones (LJ) diffusion formulation was incorporated, as shown in Figure 36. Coupling the evaporation model with the LJ-based diffusivity led to improved agreement with the experimental data reported by Wilms [89].

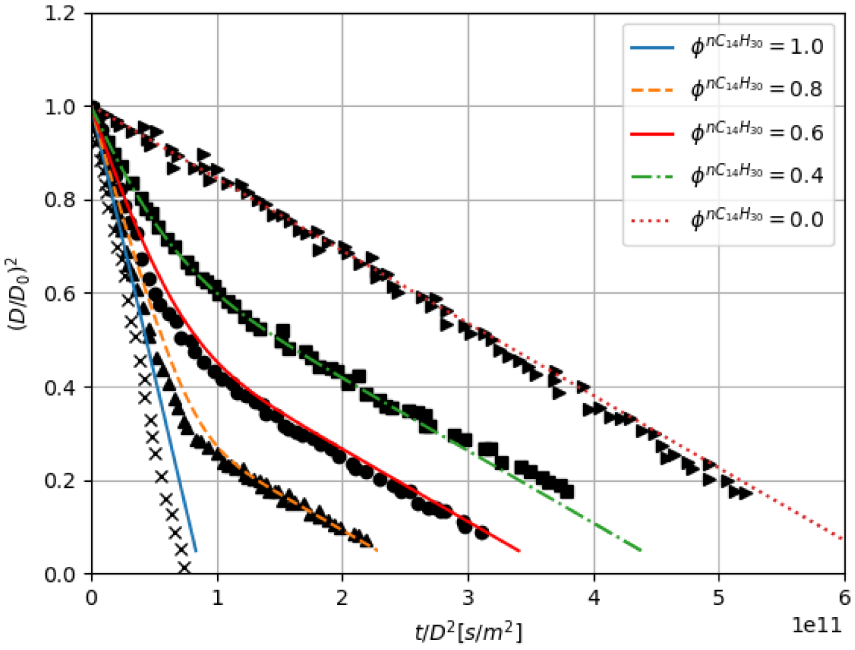

Figure 36: TCM coupled with Lennard-Jones diffusivity.

After evaluating the evaporation rates, the particle mass fraction of each component was computed to ensure consistency. To ensure the correctness of the implementation, a mass conservation check was performed, comparing Eulerian and Lagrangian mass values over time. The results are presented in Figure 37.

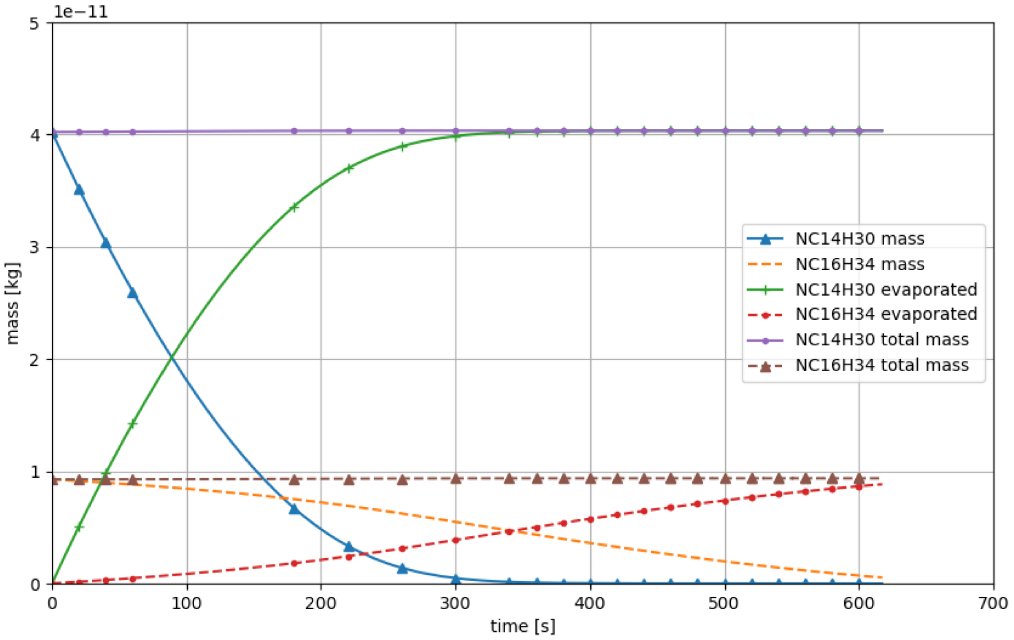

Figure 37: Mass conservation analysis between Eulerian and Lagrangian phases.

The results showed excellent agreement with experimental data. The incorporation of the Lennard-Jones diffusivity model further improved the accuracy of the simulations. While the thermodynamic properties were evaluated using the Cantera range mechanism, which is tabulated starting at 300 K, the reduced LJ approach determines diffusivity directly from molecular characteristic lengths and energy parameters. This difference in formulation may explain why the LJ-based model produced more accurate results.

8.2 Sacomano's Model Validation

Another relevant feature of Sacomano's model is the potential to incorporate non-ideal vapor–liquid equilibrium (VLE) via activity coefficient models such as van Laar [57] or UNIFAC [29, 68, 12]. The importance of accounting for non-ideal behavior is also

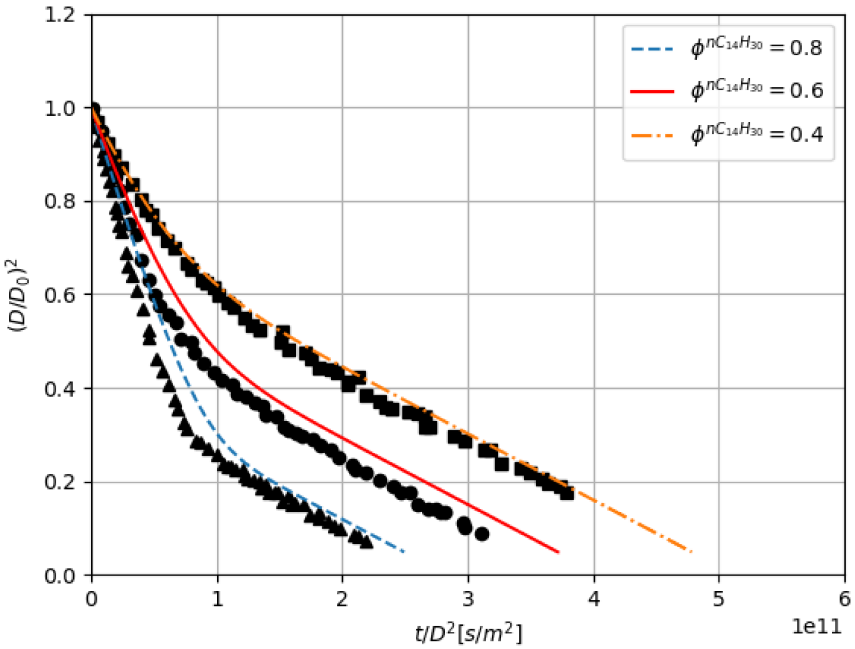

Figure 38: Sacomano's model using the diffusivity pondered by mass fraction.

emphasized by Sazhin et al. [71], who showed that ideal assumptions often underestimate or misrepresent component interactions.

The simplified version of Sacomano's model produced promising results, even without implementing a non-ideal VLE. Figure 38 shows the case where the diffusivity $D_{k,m}$ is weighted by mass fractions at the droplet surface:

Figure 39 shows a case using Blanc's law. Both approaches yielded nearly identical results, differing only at the thirteenth decimal place, confirming the numerical consistency of the implementations.

Figures 39 and 40 yield nearly identical results, likely due to the simplifications adopted in Sacomano's model. These simplifications may suppress the effects of differential diffusion, and under certain conditions—especially when dealing with components that differ significantly in volatility or diffusivity—this assumption could lead to inaccurate predictions of evaporation rates. Such discrepancies are expected to become more evident when simulating mixtures with components more dissimilar than the hydrocarbons analyzed in this study. This discrepancy might also arise under high-temperature conditions, although additional tests are necessary to verify this.

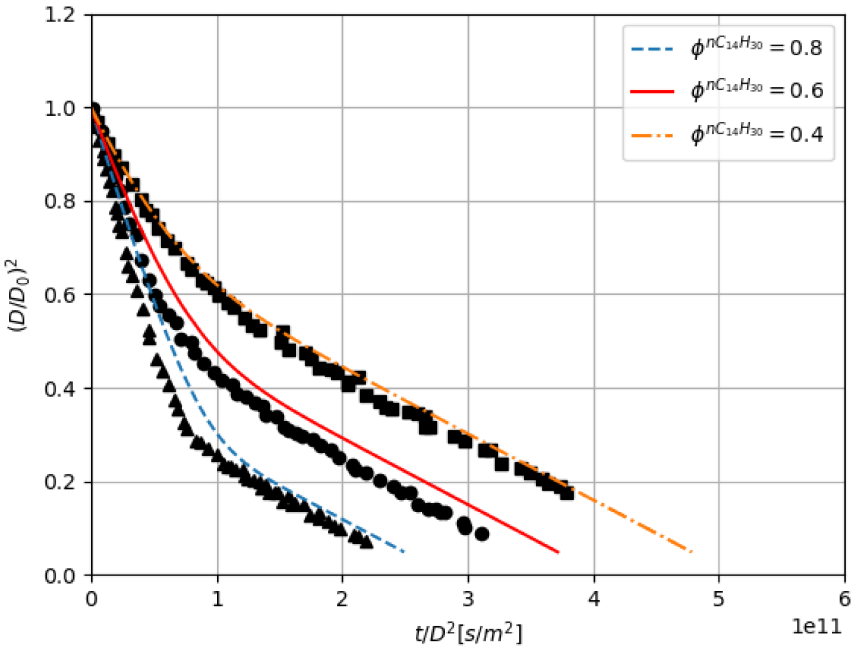

Figure 39: Sacomano's model using Blanc's law.

Both TCM and Sacomano's models successfully reproduced multicomponent evaporation behavior. Each model captures different aspects of the physical process, and both showed excellent agreement with experimental trends, reinforcing their suitability for further use in more complex spray simulations.

8.3 Atmospheric Distillation Towers

Presence of acid compounds (mainly hydrochloric acid) in Crude Distillation Units (CDU) Overhead Systems, where water condenses, leads to the formation of a low pH aqueous phase that may cause acid corrosion. To avoid that, a neutralizer is usually added to the overhead system (either ammonia or neutralizing amines). However, in case there is an excess of chlorides or neutralizer (or both of them), there may be salt deposition, which leads to under-deposit corrosion [19].

In this document two CDU's Overhead Systems are analyzed. The reason to analyze them is to understand the reason the behavior of one system is better than the other. The difference could mainly be studied in thermodynamic models by the correct usage

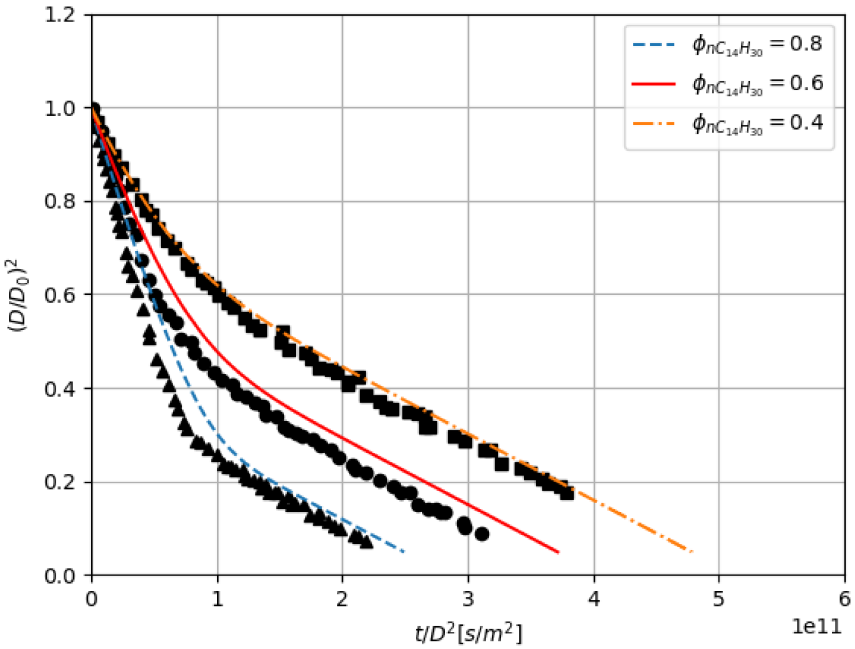

Figure 40: Sacomano's model using Coffee and Heimerl [14] diffusivity.

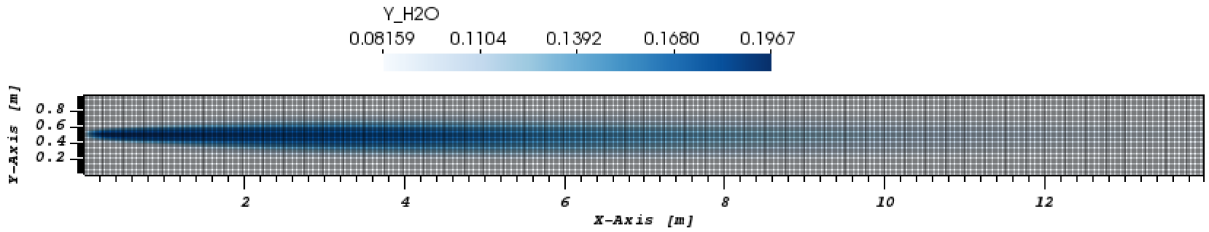

Figure 41: CDU1 mesh refinement

of a multicomponent spray analysis. To simplify the names and explanation, the CDU Overhead System that works correctly is called CDU 1, while the other CDU 2.

Previous analysis were made and the mesh refinement didn't proof any significant improve. Therefore, the dynamic meshing wasn't used.

Table 8: Domain and mesh parameters

	CDU1	CDU2
x-length [m]	30	14
y-length [m]	1	1
z-length [m]	1	1
mesh length [m]	0.025	0.025

Based on preliminary analyses of individual droplets using different transport models,

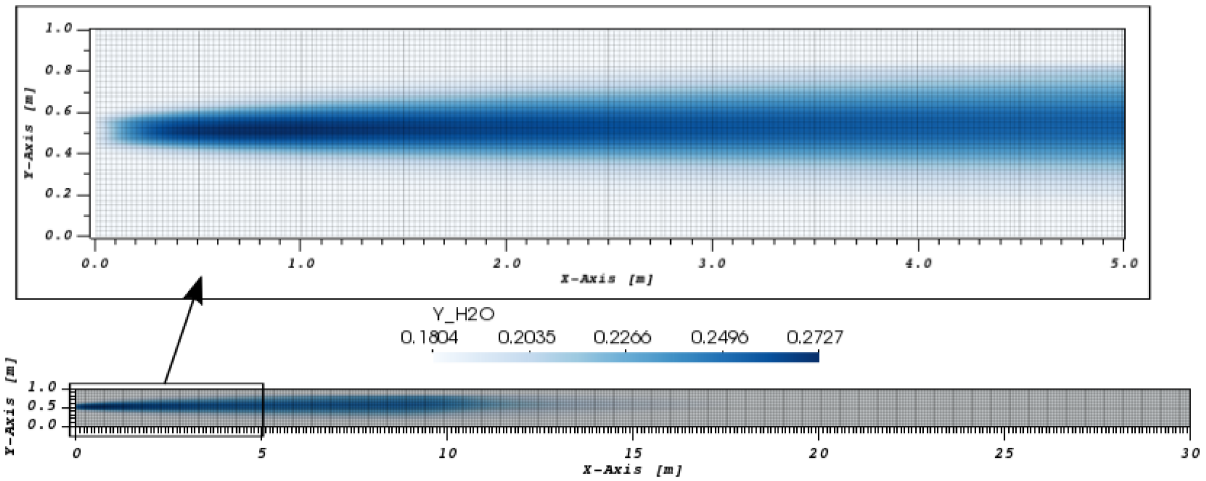

Figure 42: CDU2 mesh refinement

the multicomponent spray simulations were initially carried out with the simplest models, primarily due to the greater numerical stability they offer. From the first results, it became evident that adjustments to the setup and the adoption of more sophisticated models were required to address the limitations identified.

In parallel with the initial simulations, additional cases were conducted for CDU1 and CDU2, considering single-droplet scenarios and focusing on the thermodynamic analysis. Given the complexity of the boundary and inlet conditions in these cases, several adjustments were necessary and will be detailed throughout this results presentation.

Following the analysis and validation of the implemented evaporation models, a considerable number of simulations were performed using different hypotheses and configurations. As a result, the results for CDU1 and CDU2 are presented according to the adopted transport models and modeling assumptions. Several improvements to the setup proved to be essential and were identified through the analysis of the simulation results. Therefore, the results are presented alongside a table that describes each configuration in detail, as well as the progressive modifications introduced throughout the simulation process, as shown in Table 9.

Based on the assumptions mentioned above, the Unity-Lewis diffusivity model was used to calculate species diffusivity in the Eulerian phase, as the Mixture-Averaged approach may lead to inconsistencies related to the calculus of diluent mass fraction.. These

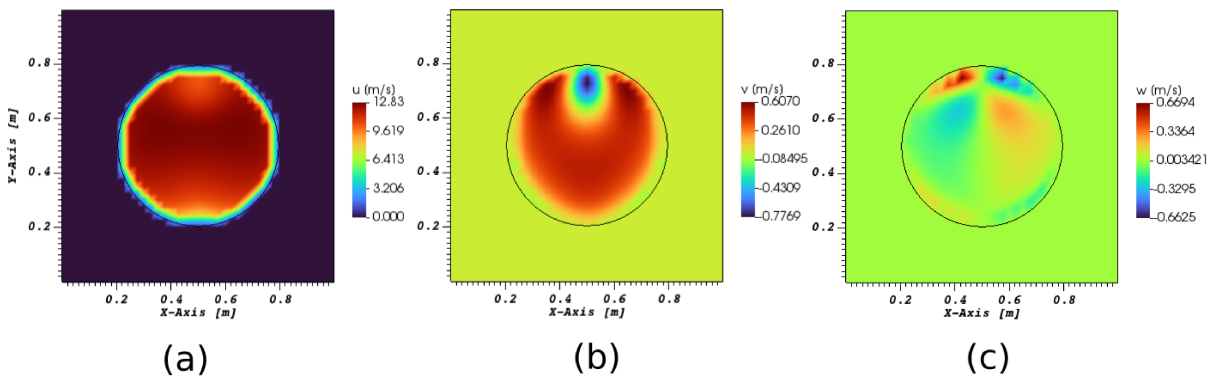

Figure 43: CDU 1 simulated with TCM multicomponent evaporation model approach, assuming ITC and Unity-Lewis in 0.795 physical seconds. (a) Represents the eulerian velocity in x-axis, (b) y-axis and (c) z-axis.

inconsistencies arise from differences in diffusivity among species, which can ultimately lead to a lack of mass conservation [63]. In pursuit of a more physically consistent approach, a correction based on the hypothesis of Hirschfelder and Curtiss [63] is being considered to improve physical consistency.

Due to the validation of the Tonini and Cossali Model (TCM), almost all spray simulations carried out were performed with this model. It is worth noting that the model proposed by Sacomano [29] shows sensitivity to certain physical conditions, which are commonly encountered in complex spray cases such as CDU1 and CDU2—for instance, when the rates of evaporation and condensation are equal, leading to $\dot{m} = 0$. Furthermore, considering that the radiation term described by Kitano [40] is essential in situations where the droplet temperature differs significantly from the surrounding gas temperature, all simulations included this radiative effect.

The inlet boundary conditions was built based on injector experiments, [83] analysed the outlet parameters of these injectors and made a statistical analysis. Overall, the only parameter that was assumed constant was the lagrangian and Eulerian temperature and pressure due to the near-constant results.

The first step was understanding the results by assuming Abramzon Sirignano Model and Unity Lewis approach, which were extracted by Venturi [83] and postprocessed by this author.

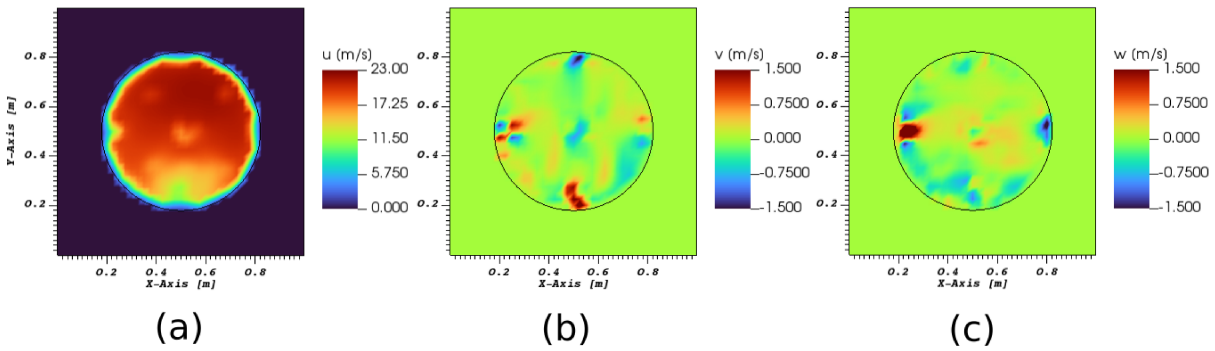

Figure 44: CDU 2 simulated with TCM multicomponent evaporation model approach, assuming ITC and Unity-Lewis in 0.063 physical seconds. (a) Represents the eulerian velocity in x-axis, (b) y-axis and (c) z-axis.

8.3.1 Initial Case with Unity-Lewis

The initial simulations were based on a previously defined setup, in which the only modification was the replacement of the single-component evaporation model with a multicomponent formulation. Since the Unity-Lewis hypothesis was already adopted for the Lagrangian phase, the simulations for CDU1 and CDU2 were conducted according to the conditions presented in Table 9.

Table 9: Boundary conditions for the initial cases of CDU1 and CDU2.

BC	CDU1 Case 1	CDU2 Case 1
Immersed Boundary Type	MDF	
Lagrangian Transport Model	Unity-Lewis	
DPM Thermal Model	ITC	
Parcel	10	
Diluent	NC7H16	C9H19-1
Poisson Model Correction	N/A	

Table 9 summarizes the main parameters that were varied throughout the simulations and had a direct impact on the results. A brief explanation of each entry is provided below:

- Immersed Boundary Model: defines the method used to represent the interaction between the flow and solid boundaries.
- Lagrangian Transport Model: determines the diffusivity and thermal conductivity models applied to the particles.

- DPM Thermal Model: refers to the discretization method for the internal droplet temperature field.
- Parcel: represents the number of physical droplets modeled by a single numerical particle.
- Diluent: chemical species used as the carrier gas in the ambient phase.
- Poisson Model Correction: indicates whether or not mass source terms are included in the Poisson equation used in the PISO algorithm.

The Immersed Boundary Method (IB) enables the simulation of flows around complex geometries using fixed (non-body-fitted) meshes. One widely used strategy to enforce boundary conditions at the immersed surfaces is the Momentum Distribution Formulation (MDF). In this approach, a correction force is calculated at Lagrangian points on the surface and distributed to neighboring Eulerian grid nodes using a discrete delta function. This force is then added as a source term in the momentum equations, ensuring that the no-slip condition is satisfied without the need for mesh deformation or reconstruction.

A critical point in the modeling process was the definition of the diluent species. This choice influences two main strategies in the evaporation model: (i) allowing phase change (evaporation/condensation) for all droplet components, or (ii) assuming that the diluent remains permanently in the gas phase. In this work, the second strategy was adopted, since errors in mass fraction evaluation are absorbed by the diluent, preventing the occurrence of negative mass fractions.

Initially, the first approach was tested, but under the operating conditions of CDU1 and CDU2, the Spalding number (B_M) frequently dropped below -1, making the mass flux $\dot{m}$ undefined due to the logarithmic term $\ln(1 + B_M)$ in the TCM formulation. As shown in Eq. 8.3.1, when the gaseous mass fraction of a component exceeds its surface mass fraction, the Spalding number becomes negative. To address this issue, the model was modified to switch the sign of the mass flux from evaporation to condensation whenever this condition arises.

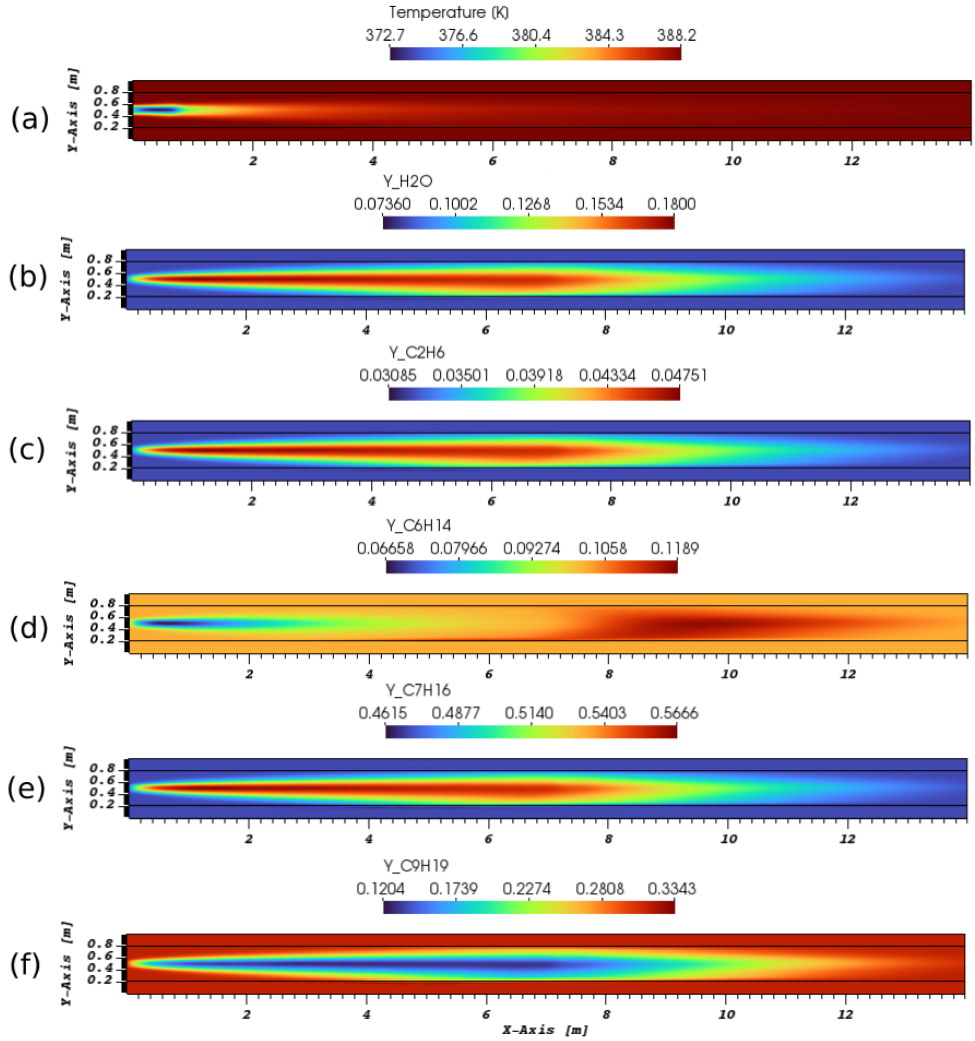

Figure 45: Simulation of CDU1 under the conditions described in Table 9, at 0.795 seconds of physical time, not fully developed. Figure (a) shows the temperature field; figures (b)–(f) depict the Eulerian mass fractions of H_2O, C_2H_6, C_6H_{14}, C_7H_{16}, and C_9H_{19}, respectively.

Several tests were performed using C_2H_6 and C_6H_{14} as candidate diluents. Ethane was considered because its critical temperature is lower than the local gas temperature in both CDUs, keeping it in a gaseous or supercritical state. Hexane, on the other hand, presents a vapor pressure higher than the ambient pressure at the outlet, leading to condensation near the inlet but subsequent evaporation along the domain. This behavior suggests that hexane could be considered a secondary option as a diluent, under the assumption that it predominantly remains in the gas phase.

Due to their low mass fractions and the numerical errors introduced by the MDF model, both species led to nonphysical negative mass fractions. That's the reason the

second approach, calculating the diffusivity of diluent was adopted, where the diluent is fixed as a permanent gas-phase species. The most abundant component in each case was selected: C_7H_{16} for CDU1 and C_9H_{19} for CDU2.

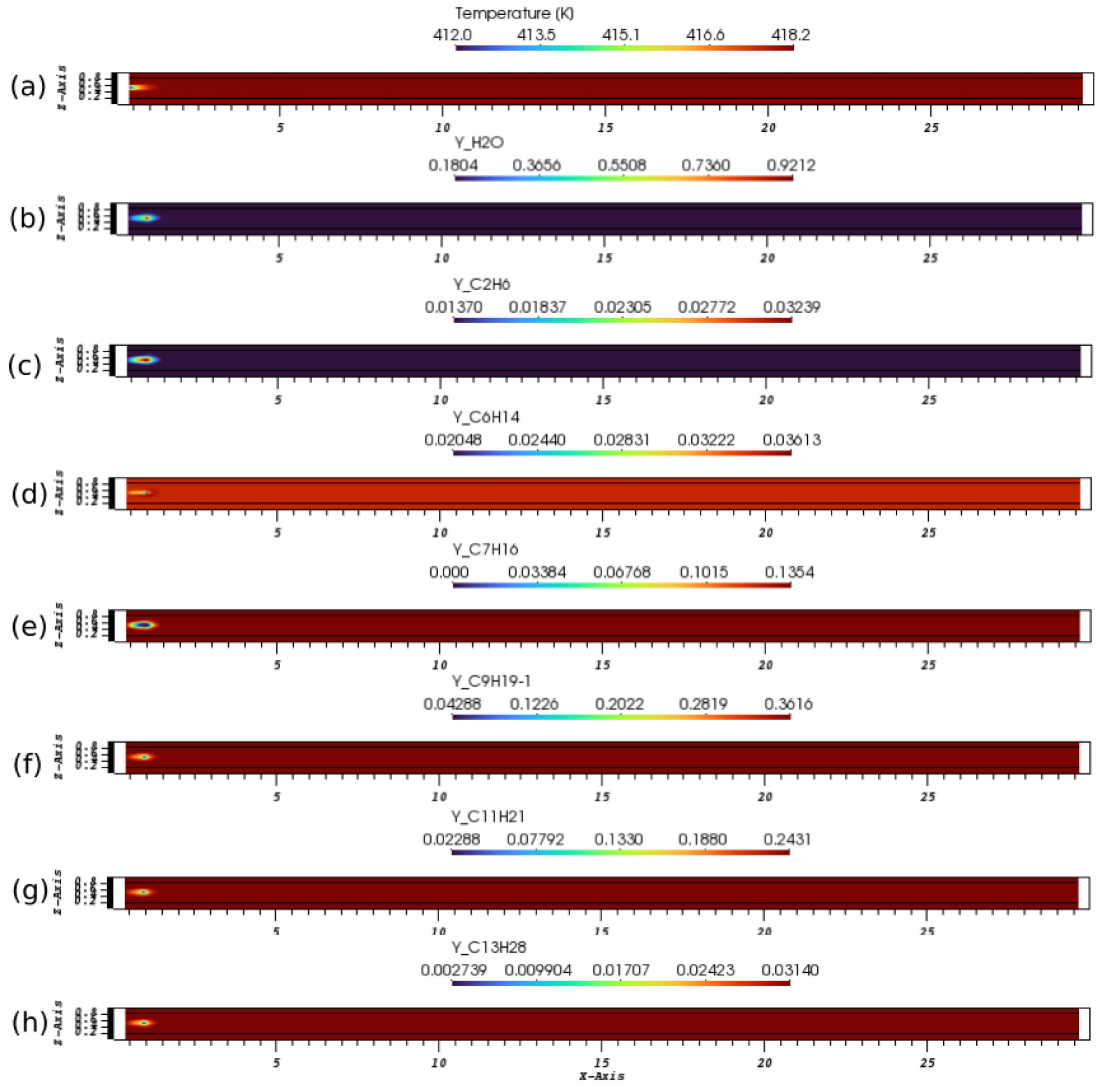

Figure 46: Simulation of CDU2 under the conditions described in Table 9, at 0.063 seconds of physical time. Figure (a) shows the temperature field, while figures (b)–(h) depict the Eulerian mass fractions of H_2O, C_2H_6, C_6H_{14}, C_7H_{16}, C_9H_{19}, $C_{11}H_{21}$, and $C_{13}H_{28}$, respectively.

Figure 47 clearly illustrates the condensation behavior of species, as evidenced by the increasing mass fraction of less volatile components in the particles. Initially, the droplet consisted exclusively of H_2O, and along the pipe a progressive reduction in the water mass fraction can be observed. The particle diameter exhibited only slight decreases, since the condensation rate was nearly equal to the evaporation rate. After further corrections to

the simulation boundary conditions, quantitative results were obtained that clarified this behavior.

Both CDU1 and CDU2 simulations experienced numerical instabilities after short physical times. A detailed analysis revealed that the main causes of divergence were inconsistencies in the evaporation model formulation and issues with the numerical setup. In particular, for CDU2, only 0.063 seconds could be simulated before the computation failed.

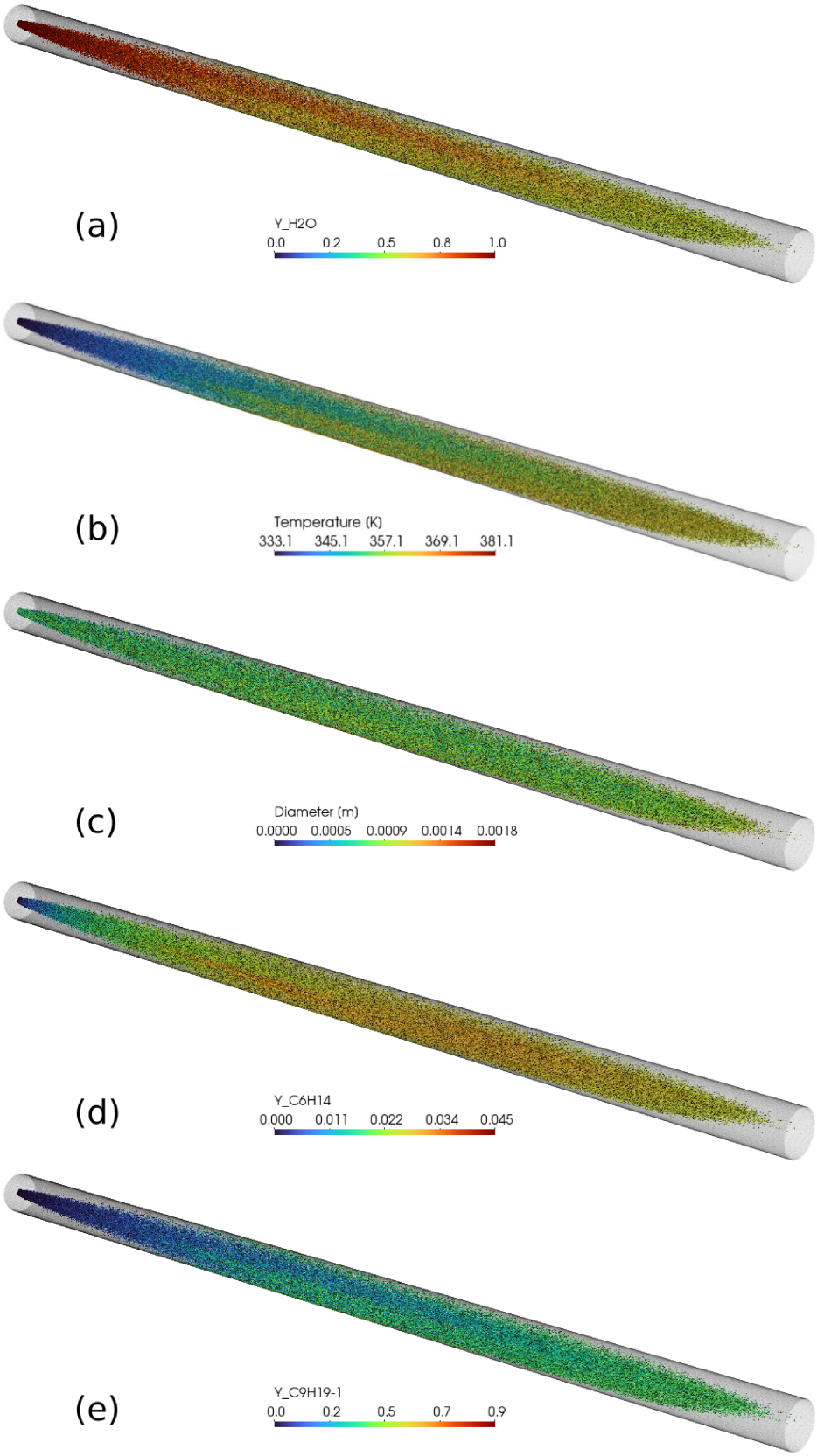

Figure 47: Simulation of CDU1 using the multicomponent TCM, assuming ITC and Unity-Lewis, at 0.795 seconds of physical time. Figure (a) shows the temperature field, and figures (b)–(f) show the Lagrangian mass fractions of H_2O, C_2H_6, C_6H_{14}, C_7H_{16}, and C_9H_{19}, respectively.

Since the simulation of CDU1 Case 1 covered only a single residence time of the sprays, the Lagrangian (liquid-phase) mass flow rate was evaluated at intermediate cross-sections within the domain, as shown in Figure 48. The mass flow rates of each liquid component across the 6.5 m and 10 m planes are shown in Figure 49. These results show a decreasing trend in the H_2O mass fraction due to evaporation, while hydrocarbons condense from the surrounding vapor, a trend also expected in CDU2.

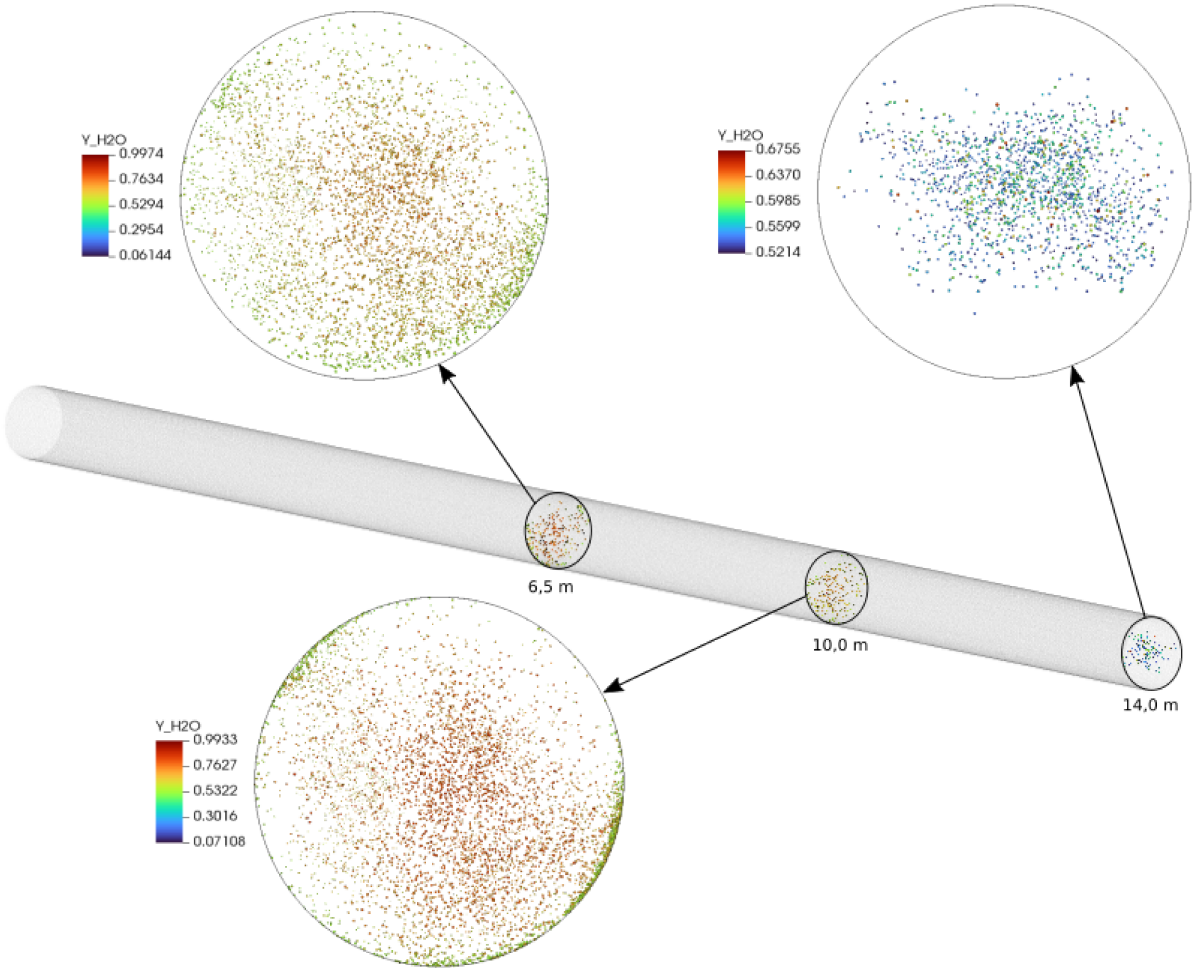

Figure 48: Representation of the cross-sectional planes analyzed for calculating the liquid mass flow rate in CDU1 across the 6.5 m (a) and 10 m (b).

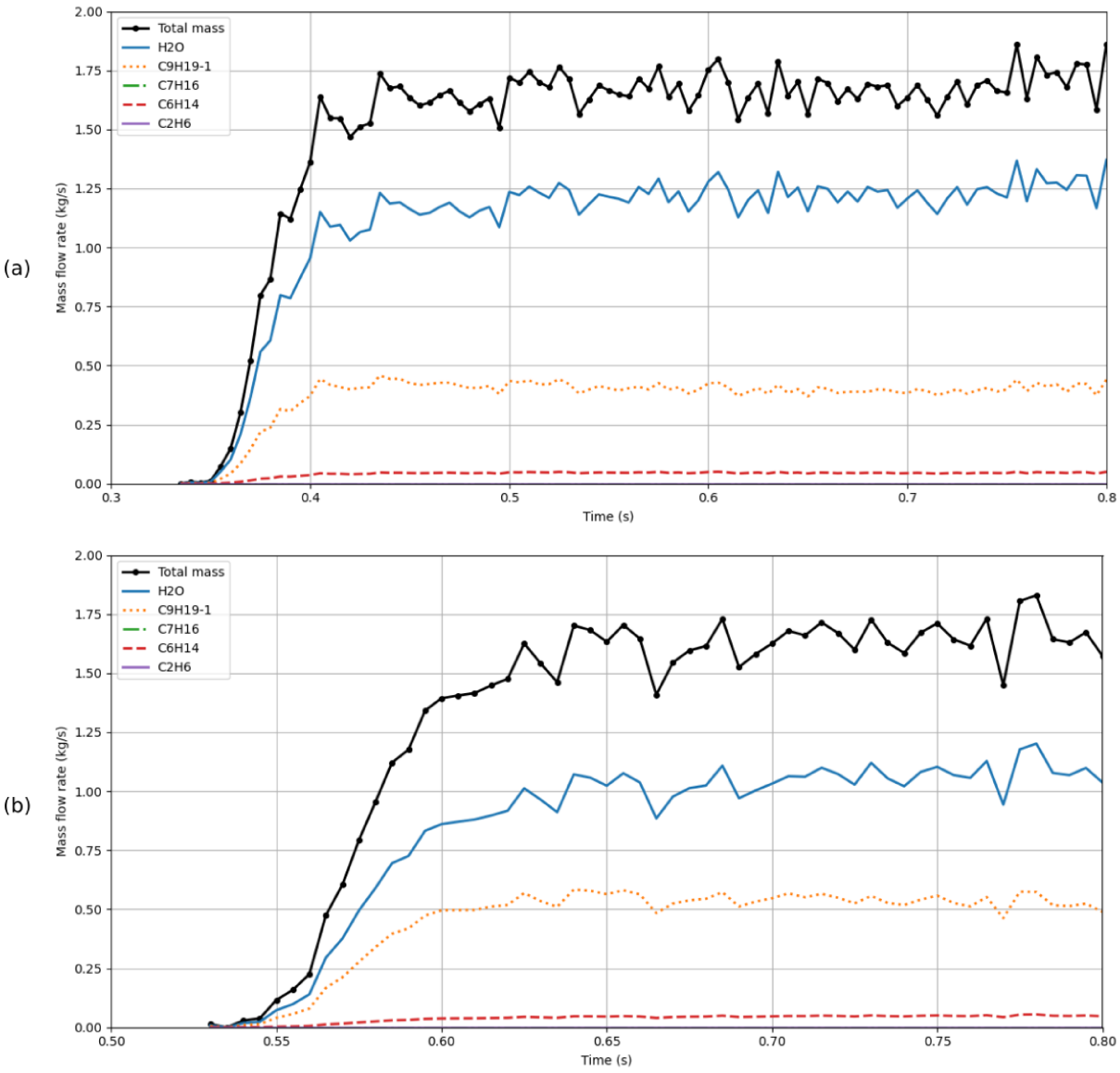

Figure 49: Liquid mass flow rate of the components across the analyzed sections in CDU1.

Given the greater numerical challenges posed by CDU2, the next simulations focused on CDU1, where more advanced modeling assumptions were explored. Case 2 employed the Mixture-Averaged transport model, while Case 3 tested the FTC thermal model, as described in Table 10.

Table 10: Boundary conditions for Cases 2 and 3 of CDU1.

BC	CDU1 Case 2	CDU1 Case 3
IB Type	MDF	
Lagrangian Transport Model	Mixture Averaged	
DPM Thermal Model	ITC	FTC
Parcel	10	
Diluent	NC7H16	
Poisson Model Correction	N/A	

During simulations using the Mixture-Averaged model, a tendency to overestimate condensation was observed. This behavior is linked to the formulation of the Spalding number:

$$B_M = \frac{\sum_k Y^s_{v,k} - \sum_k Y^g_{v,k}}{1 - \sum_k Y^s_{v,k}},$$

where $Y^s_{v,k}$ and $Y^g_{v,k}$ are the vapor mass fractions of component k at the droplet surface and in the surrounding gas, respectively. When the gradient favors condensation ($Y^g_{v,k} < Y^s_{v,k}$), B_M becomes significantly negative, which leads to unphysically large values for $\dot{m}$ due to the logarithmic form of the model.

To mitigate this issue, a simple correction was implemented: when $B_M < 0$, its value was inverted and the evaporation flux was calculated as a condensation term with reversed sign, ensuring a physically realistic condensation rate. This adjustment guarantees that the formulation does not predict condensation rates exceeding evaporation, which would be unphysical; instead, both processes are balanced when this condition arises.

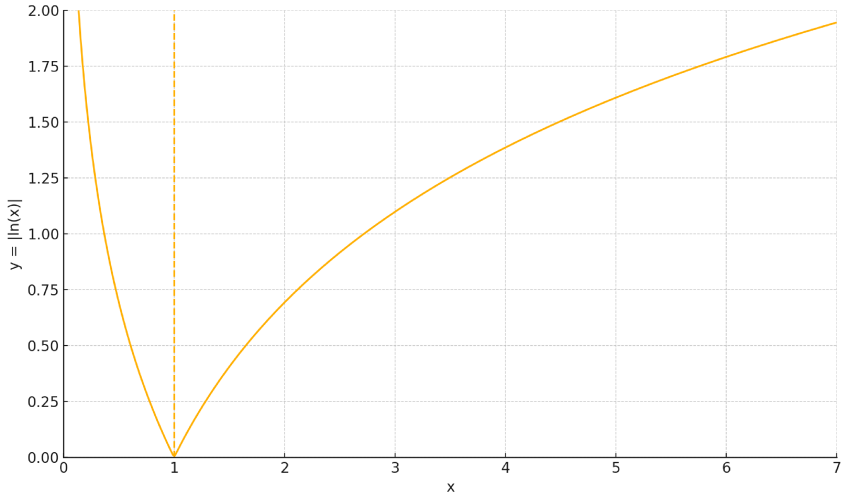

Figure 50: Illustration of how the use of the logarithmic formulation in the Spalding number can compromise the calculation of the condensation rate.

Another important correction was applied to situations in which the sum of surface vapor mass fractions exceeded unity. In these cases, the mass fractions were renormalized to enforce the physical constraint that their sum must equal one. This typically occurs when a component's saturation vapor pressure exceeds the local pressure. The effect was especially notable for C_6H_{14}, as illustrated in Figures 54 and 45(d).

The CDU1 simulation for Case 2 reached 4.55 seconds of physical time, allowing a more detailed assessment of the downstream flow conditions. Although the gas-phase temperature had not fully converged (Figure 53), the water vapor mass flow rate was approximately 1.08 kg/s. These findings, along with limitations of the Immersed Boundary (IB) model and solvers, led to a decision to restart simulations with adjusted boundary conditions.

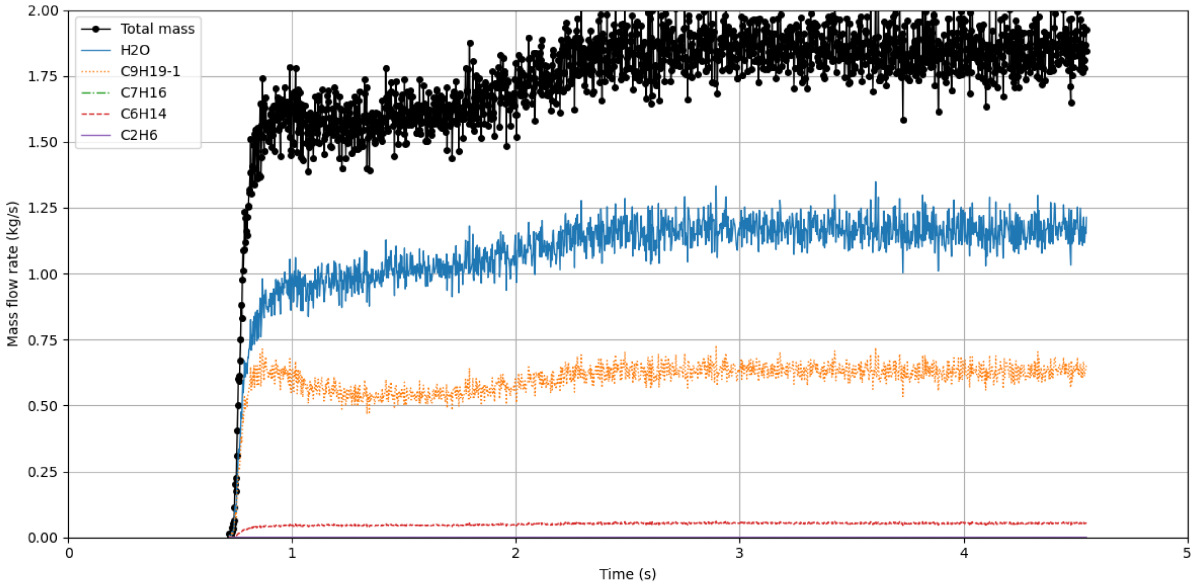

Figure 51: Liquid mass flow rate of the particles along the CDU1 domain for Case 2.

By applying a Gaussian filter to the Lagrangian data, a smoothed time series was obtained, enabling the estimation of a mean droplet temperature of 361.88 K and a total liquid-phase mass flow rate of 1.864 kg/s at the outlet, as shown in Figure 52.

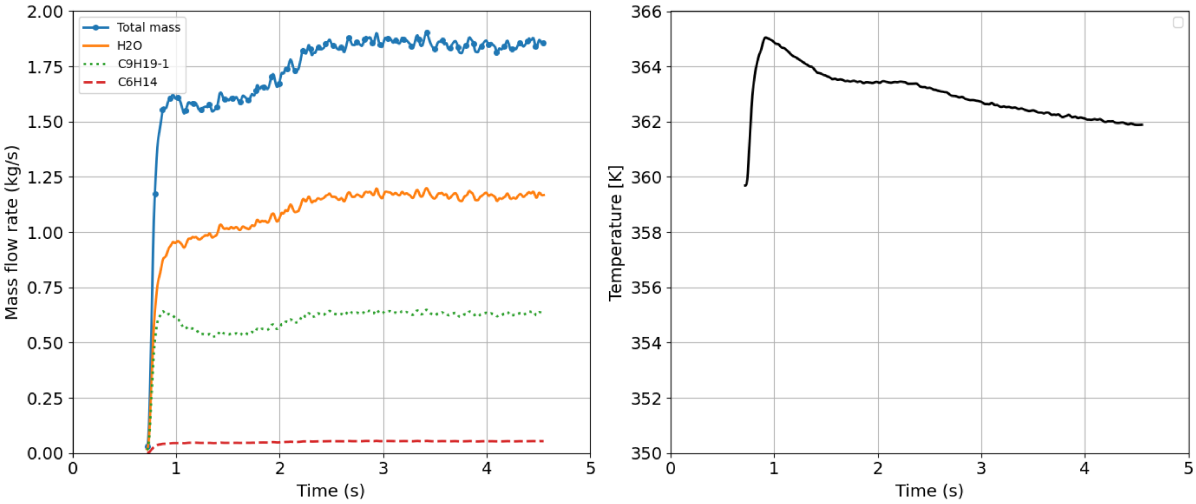

Figure 52: Smoothed time series of the average Lagrangian temperature and liquid mass flow rate for CDU1 Case 2.

Additionally, the water mass fraction along the centerline of the domain was extracted for the gas phase (Figure 56), and a vapor pressure analysis was performed (Figure 54). The increase in particles temperature from 333.15 K to an average of 361.88 K strongly influences phase change behavior for the volatile species.

Figure 52 (b) shows that the particles crossing the outlet section initially exhibit higher temperatures. This behavior is explained by the elevated gas temperature in this region, since no liquid has yet passed through it. Over time, the particle temperature tends to decrease.

The liquid mass flow in Figure 52(a) also shows that a considerable amount of mass tends to condense. Analyzing the $C9H19$-1 liquid mass fraction, it can be observed that between 1 and 2 s the fraction starts with a higher value, then decreases, and subsequently rises again. The first reduction is attributed to the higher temperatures at the beginning of the process, where part of the species had already condensed, thereby reducing its mass fraction. Several factors can contribute to the later increase in the hydrocarbon liquid mass fraction, such as temperature reduction, it means larger droplet diameters lead to higher condensation.

Figure 52(a) also reveals an interesting behavior for C_6H_{14}: the liquid mass flow rate at the outlet remains nearly constant over time. This indicates that the species could not fully evaporate, even though it would be expected to do so under long-term conditions. The limited residence time, caused by the high spray velocity inside the pipe, restricts complete evaporation.

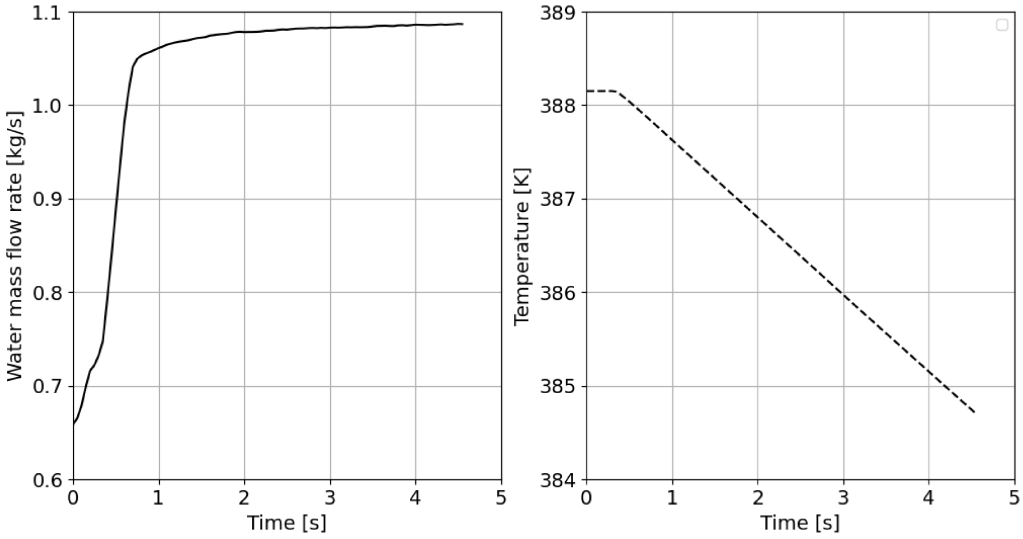

Figure 53: Average temperature and average gas-phase mass flow rate at the outlet of the vertical section of CDU1, for Case 2.

The FTC thermal model proved highly sensitive to timestep size and internal discretization of temperature and liquid mass fraction. Without adequate resolution, energy balance calculations can diverge. Therefore, careful monitoring of simulation logs is required to ensure consistent results. In general, the FTC model is more computationally expensive and prone to numerical errors than the ITC model.

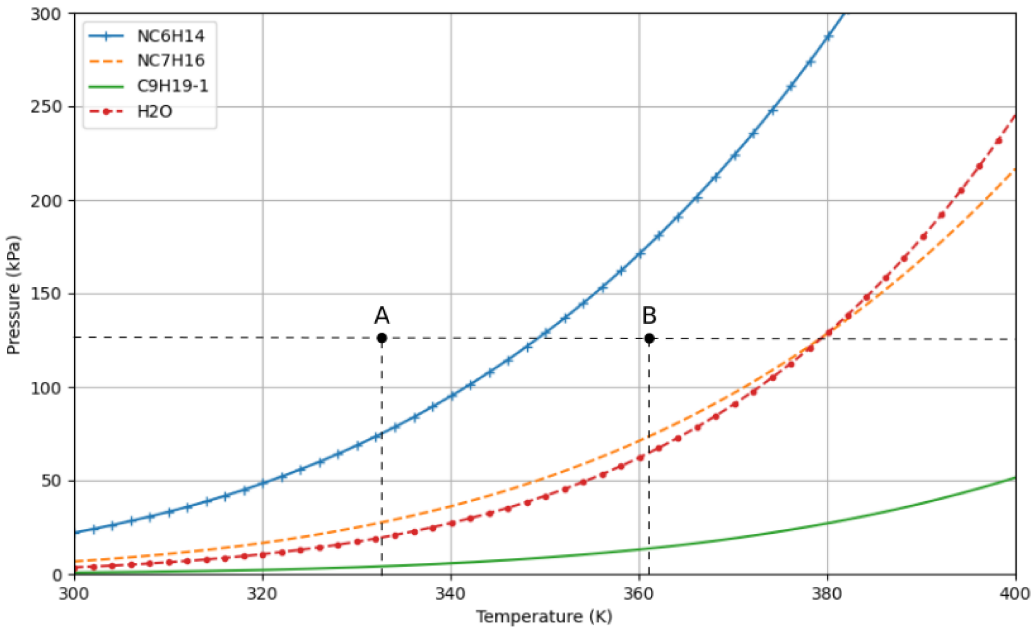

Figure 54: Vapor pressure curves as a function of temperature and ambient pressure for CDU1 Case 2.

As shown in Figure 55, Case 3 (FTC) resulted in higher water evaporation rates compared to Case 2 (ITC), which is also reflected in the central water mass fraction profile (Figure 56). However, the gas temperature remained higher, suggesting incomplete stabilization of the methodology.

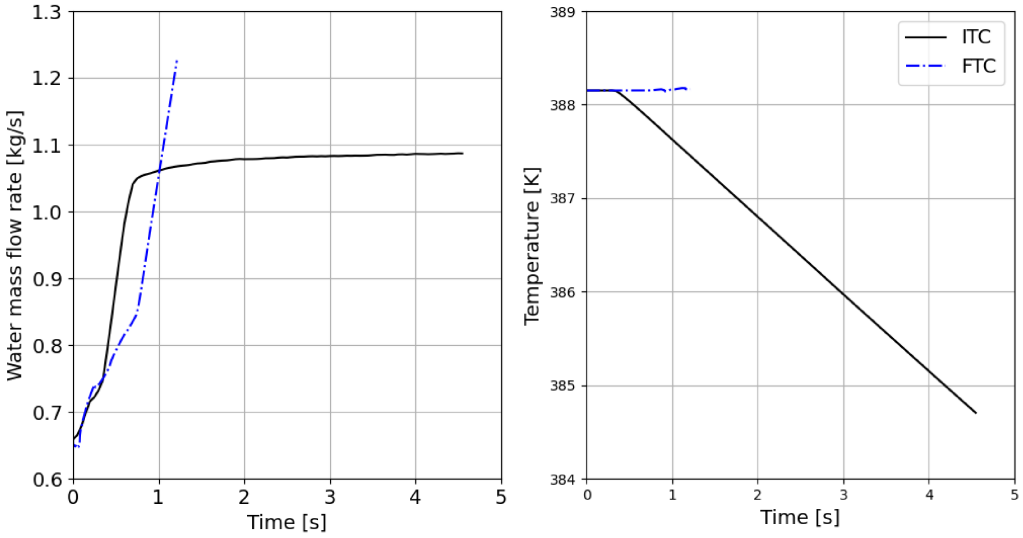

Figure 55: Comparison of the average temperature and Eulerian mass flow rate at the outlet of the vertical section of CDU1 for Cases 2 (ITC) and 3 (FTC).

It is hypothesized that further corrections to the FTC model may yield even greater evaporation and lower gas temperatures due to improved mass conservation.

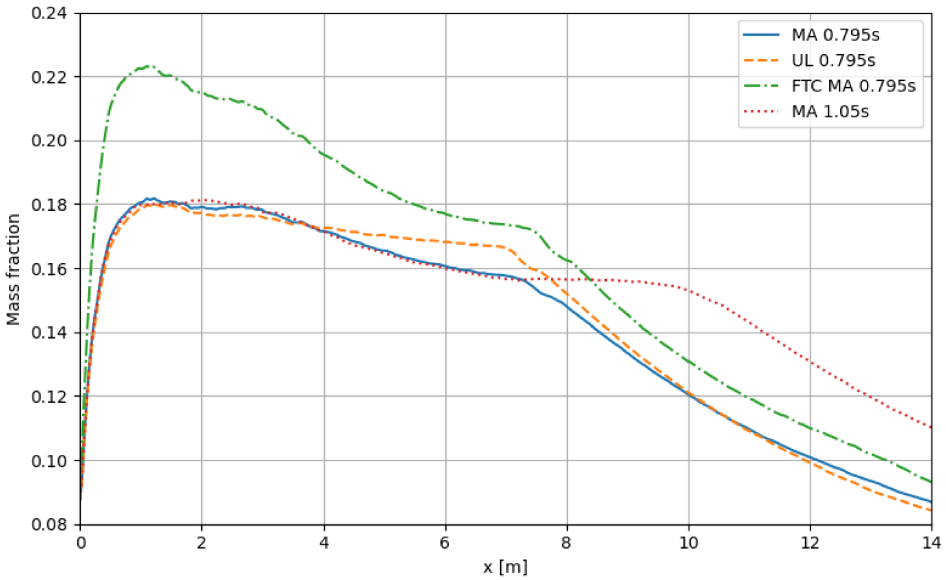

Figure 56: Mass fraction of H_2O along the Eulerian centerline for the different simulated cases.

The effects of higher assumption of diffusivity can be seen in Figure 56, where lower water evaporation rate was observed around 6 m in the Mixture-Averaged case compared to Unity-Lewis.

Finally, the resolution of memory management issues in the CDU2 simulations was crucial. Improper handling of DPM deletion routines led to segmentation faults due to inconsistencies between immediate and deferred memory deallocation. Once these routines were standardized, the simulations ran stably.

It is also worth noting that the multicomponent model requires substantially more memory due to the need to store average and surface properties, source terms, and internal variables across multiple layers. This contributed to slower development in the initial stages.

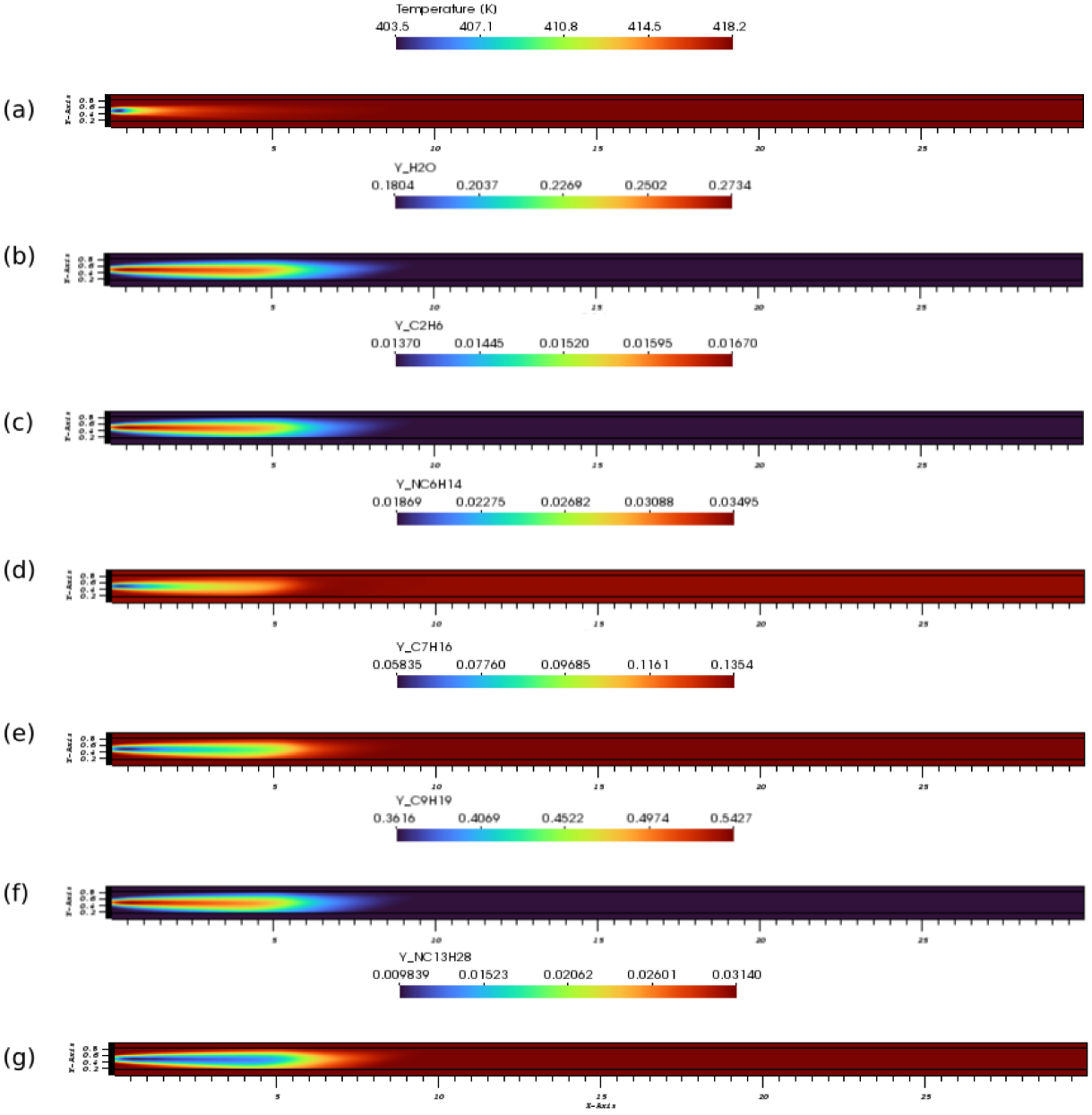

Figure 57: Simulation of CDU2 using the multicomponent TCM, at 0.785 physical seconds, under the conditions defined in Table 9. Figure (a) shows the temperature field; figures (b)–(g) show the Eulerian mass fractions of H_2O, C_2H_6, C_6H_{14}, C_7H_{16}, C_9H_{19}, and $C_{13}H_{28}$, respectively.

Once resolved, the CDU2 simulation reached a longer physical time, as shown in Figure 57. However, in Table 11 severe coupling issues between the MDF and DPM models were identified, leading to excessive DPM iterations (from 10 to 900) and a dramatic increase in simulation time (from 23.7 seconds to 25.5 minutes per timestep). This was attributed to high vorticity near walls, which is more pronounced in CDU2 than in CDU1.

Table 11: Comparison of two MFSim simulations for DPM configuration

Property	Same case	
Number of particles	289,562	289,595
DPM iterations (n_{iter})	10	900
DPM time step (dpm_dt)	2.00×10^{-6}	2.22×10^{-7}
DPM total time (dpm_t)	0.17582	0.17584
Time step wall-clock	23.7762 s	25.5576 min
Max time spent (ToT)	23.4818 s	25.5367 min
Max time with sync (ToS)	18.2698 s	24.9914 min
Sync time (%)	1.2381%	0.0817%
Memory usage	26.9386 GB	26.9387 GB
Estimated end time	1361.8075 days	18807.4069 days
Iterations (ct)	8792	8793
maxU	28.0692	28.0694
maxV	11.7779	11.7777
maxW	11.4109	11.4107
maxT	418.2013	418.2014
DPM Δt	2.00×10^{-5}	2.00×10^{-5}
dt/dt1	1.0	1.0
t	0.1758399999	0.1758599997

Given the MDF model's poor scalar resolution and high computational cost, it was discontinued in favor of the PISO algorithm. Before resuming simulations, the Poisson equation was updated to include the mass source term, as detailed in Section 7.7. This led to significant changes in the pressure distribution, as illustrated in Figure 58.

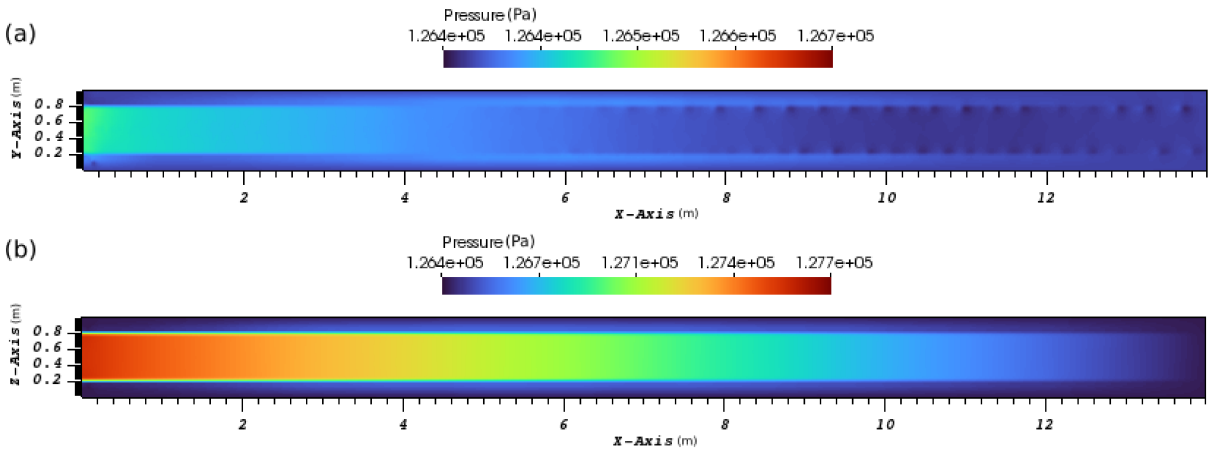

Figure 58: Difference in the pressure profile of CDU1 when considering the mass source term in the Poisson equation, after 4.0 physical seconds of simulation.

An effect that it could create is the micro-explosion of puffing mentioned by Antonov

[5], which mentions the so-called secondary atomization of suspension droplets in combustors, which can increase the evaporation rate increasing the combustion performance. The increase of vapor pressure can create the phenomenon called puffing [67, 5] or microexplosions [79]. Shinjo [73] explains physically the both phenomena.

8.3.2 Simulations with Ghost-Cell Approach

When the Momentum Distribution Formulation (MDF) was employed to impose the immersed boundary conditions, significant numerical instabilities were observed in the vicinity of the particle interface. The smoothing effect introduced by the discrete delta function in MDF can artificially spread the interface over multiple grid cells, which not only leads to a less accurate representation of sharp gradients but also introduces spurious oscillations in the velocity field. These oscillations amplified turbulent fluctuations around the droplet, making the flow field highly unsteady and slowing the convergence of the simulation. In contrast, the Ghost Cell (GC) method directly enforces boundary conditions with higher spatial accuracy and minimal artificial diffusion. As a result, simulations using GC showed much smoother behavior near the interface and achieved convergence more rapidly, especially in cases involving evaporation where accurate resolution of thermal and species gradients is critical.

The new simulations, based on the Ghost-Cell (GC) approach, are detailed in Table 12. The use of the GC technique proved to be considerably more stable and yielded more coherent results, as scalar fields are computed with greater accuracy. However, this approach demands more memory, requires external libraries such as PETSc, and imposes constraints such as the need to simulate the entire IB domain (e.g., if the IB spans 14 m, it is not possible to simulate only 5 m of it).

Table 12: Boundary conditions using the Ghost-Cell (GC) approach.

BC	CDU1 Case 4	CDU2 Case 2
IB type	GC	
Lagrangian Transport Model	Mixture Averaged	Unity-Lewis
DPM Thermal Model	ITC	
Parcel	10	
Diluent	NC7H16	C9H19-1
Poisson Correction	Corrected	

In the simulation of CDU1 Case 4, a physical time of 5.75 seconds was reached. Figures 59 and 60 show that, at the domain outlet, the average Lagrangian temperature was 350.18 K, with a liquid mass flow rate of 1.277 kg/s for H_2O, 0.402 kg/s for $C_9H_{19}-1$, and 0.045 kg/s for C_6H_{14}. In the Eulerian phase, the initial gas mass flow rate of approximately 0.7 kg/s converged to about 1.24 kg/s of H_2O and 6.29 kg/s of total hydrocarbons.

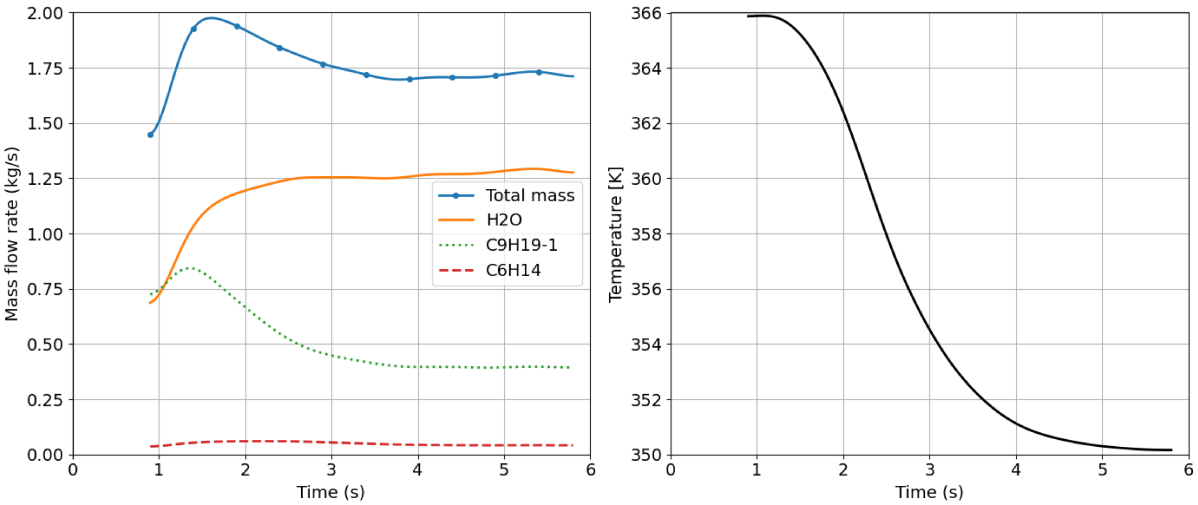

Figure 59: Filtered outlet temperature and liquid mass flow rate of each component in CDU1 — Case 4.

It is important to note that the liquid and gaseous phases at the outlet still exhibit considerably different temperatures. Figures 59(b) and 60(b) present the mean outlet temperature over time, but do not capture the tendency toward equilibrium between the phases. A temperature analysis along the pipe would likely reveal the two phases approaching each other; however, under the present boundary conditions, the persistent temperature difference indicates that thermal equilibrium cannot be achieved.

It is not possible to conclude from these analyses alone whether the faster convergence

of the gas-phase temperature at the outlet was driven primarily by the Poisson correction, the GC implementation, or the Mixture–Averaged assumption. However, it is evident that the imposed boundary conditions improved the results, leading to convergence toward a more expected value, consistent with Petrobras' analysis.

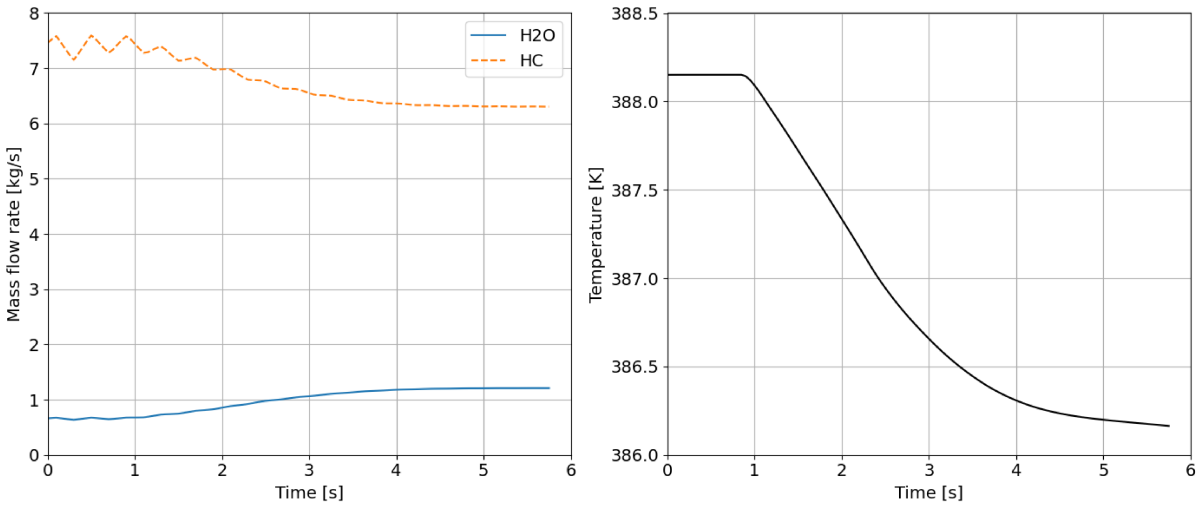

Figure 60: Gas mass flow rate and outlet temperature in CDU1 — Case 4.

In CDU2 Case 2, a total of 2.0325 physical seconds were simulated. The analyzed sections are located at 10 m, 20 m, and 30 m along the domain, as illustrated in Figure 61. However, due to high memory consumption caused by an excessively frequent data saving interval, Lagrangian-phase results were only recorded up to 1.68 seconds. This issue occurred because this was the first long-time simulation performed for CDU2.

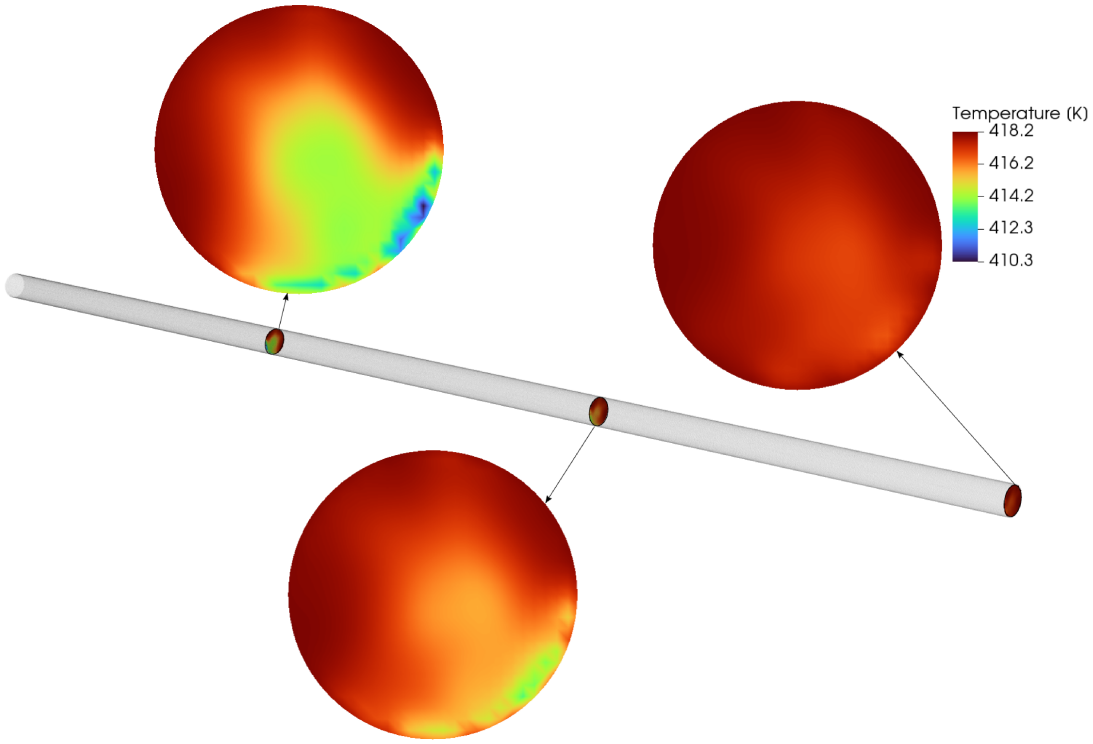

Figure 61: Temperature profile at 10 m, 20 m, and 30 m cross-sections of the CDU2 domain — Case 2.

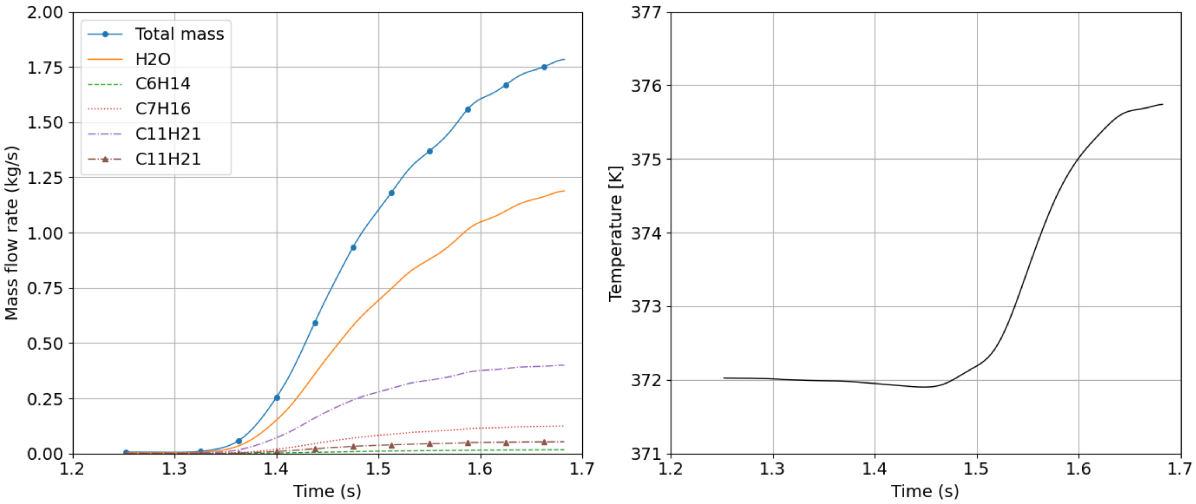

Figure 62: Liquid mass flow rate and outlet temperature in CDU2 — Case 2 (Lagrangian phase).

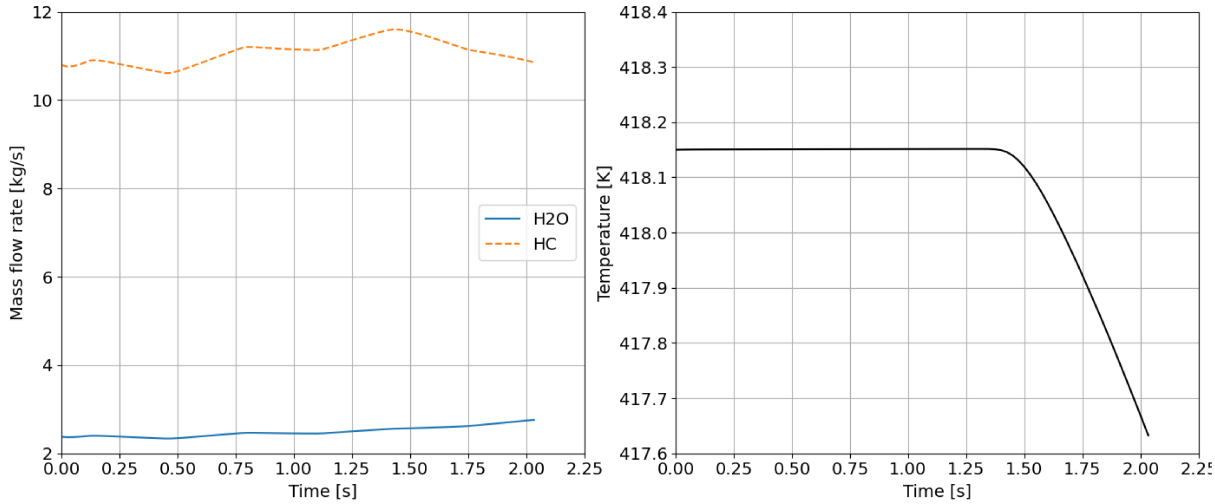

Figure 63: Gas mass flow rate and outlet temperature in CDU2 — Case 2 (Eulerian phase).

A relevant question was raised regarding the possible condensation of H_2O at the beginning of the spray, since the inlet molar fraction was around 60%. Given the initial spray temperature of approximately 60 °C, condensation was expected. However, Figure 64 presents the spatially averaged distribution of the mass source term at the final simulation step, confirming that water in the TCM model did not condense in any region. This suggests that TCM lacks the capability to accurately predict condensation under such conditions, highlighting a limitation of the formulation.

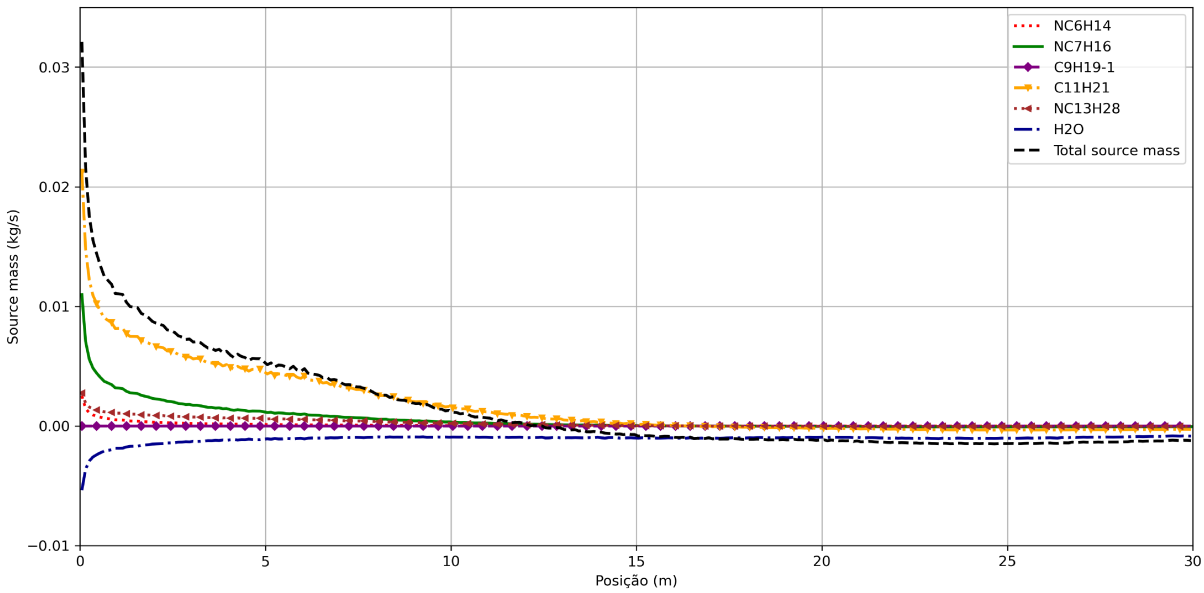

Figure 64: Spatially averaged distribution of mass source terms by component in a not fully converged solution — CDU2, Case 2.

Figure 64 shows that both water and $C11H21$ exhibit evaporative behavior at the outlet. While this outcome was expected for water, the results indicate that $C11H21$ underwent an initial condensation stage, followed by evaporation, due to the relatively high mass fraction that condensed in the early regions of the pipe.

Compared to previous simulations using the monocomponent ASM model (Figure 65), it is observed that the TCM model introduces a certain non-ideality in the vapor–liquid equilibrium. As a result, in the TCM simulation, water begins to evaporate immediately, while the other species condense.

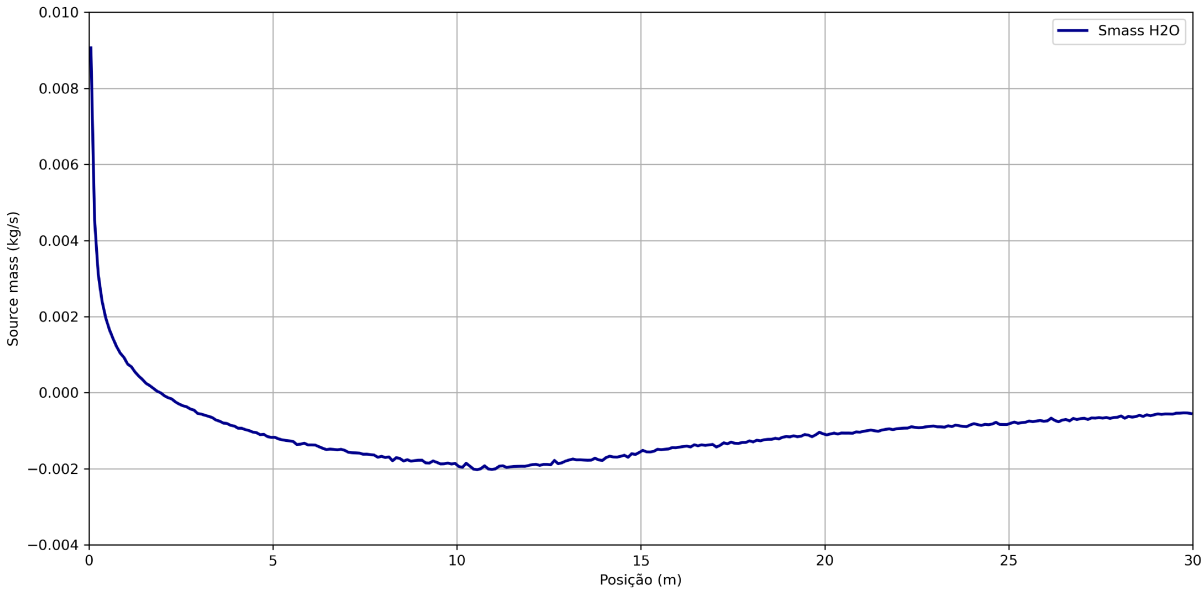

Figure 65: Average mass source term distribution for H_2O — monocomponent ASM simulation.

Additionally, a potential issue was identified regarding the use of the parcel parameter, which represents multiple physical droplets with a single particle. Up to that point, source terms were simply multiplied by the number of represented particles, without applying any correction coefficients. Due to the limitations of this approach, all simulations were rerun with parcel = 1, increasing the number of simulated particles. This adjustment improved accuracy due to the difference in the mean temperature condition at the outlet of the domain. Albeit at a higher computational cost was seen, since the particles were supposed to increase ten times.

8.3.3 Correction with Unit Parcel

Another improvement applied only for CDU1 Case 5 and CDU2 Case 3 was the implementation of dynamic time-stepping, which allowed reaching the equivalent of eight residence times with greater computational efficiency. The conditions for these final simulations are presented in Table 13.

Table 13: Final boundary conditions using Ghost-Cell and unit parcel.

BC	CDU1 Case 5	CDU2 Case 3
IB type	GC	
Lagrangian transport model	Unity Lewis	
DPM thermal model	ITC	
Parcel	1	
Diluent	NC7H16	C9H19-1
Poisson model correction	Corrected	

One limitation of the Lagrangian post-processing was the lack of physical time information in the output files, which only store the time step count. Since a dynamic time step was used, the time axis had to be reconstructed based on the known output interval (every 500 steps). Figure 66 shows the results for CDU2 Case 3.

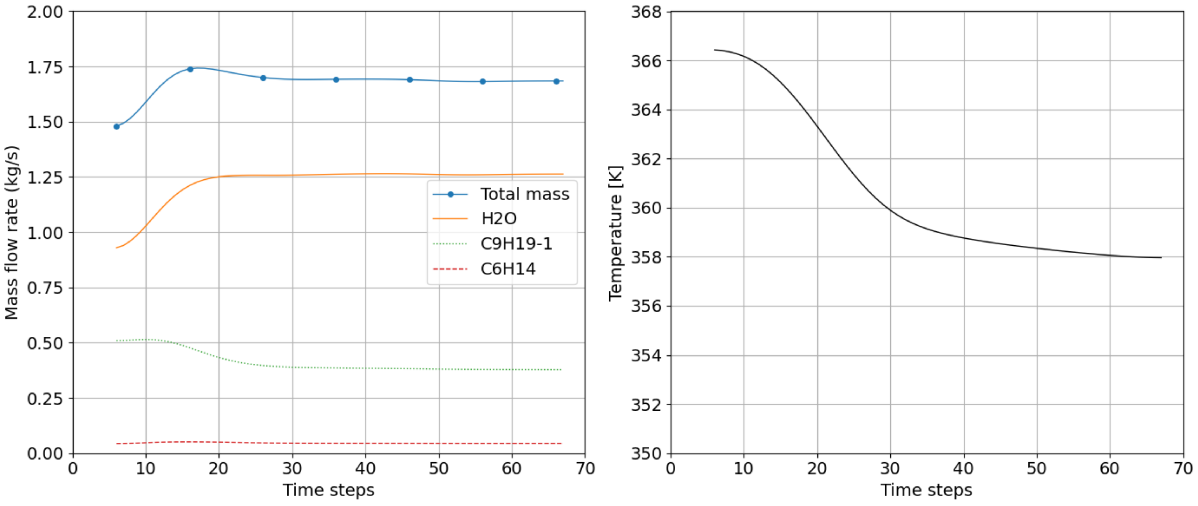

Figure 66: Lagrangian mass flow rate and temperature for CDU2 — Case 3 with unit parcel and dynamic time-stepping.

The use of unit parcel had a significant impact on the results, especially regarding the temperature, when compared to simulations with parcel = 10. As shown in Figure 67, the

average gas temperature at the outlet was lower than that in Figure 60.

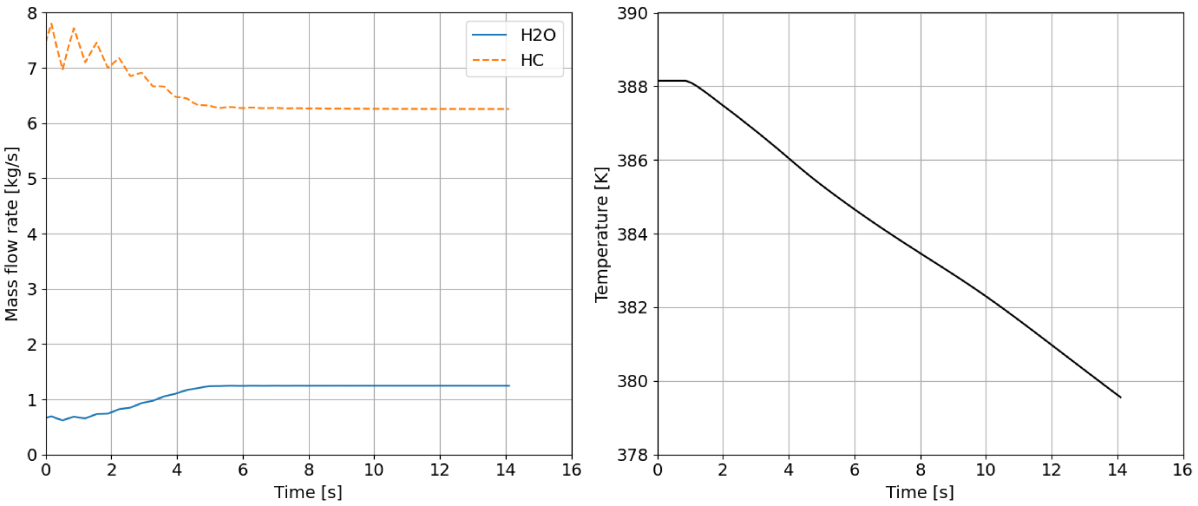

Figure 67: Gas-phase mass flow rate and outlet temperature for CDU1 — Case 5 (Table 13).

Since the gas temperature at 14 m had not yet converged, a logarithmic extrapolation was performed using the values from upstream sections, as shown in Figure 68. The fitted curve resulted in Equation 151, estimating a final temperature of 378.22 K at $x = 14$ m.

$$f(x) = -4.448 \ln(x) + 389.955. \tag{151}$$

Comparing Figure 67 with Figure 60, the gas-phase temperature decreases from 386 K to 378 K. This result indicates that the parcel model implemented in MFSim still requires further corrections and is not yet suitable for reliable use.

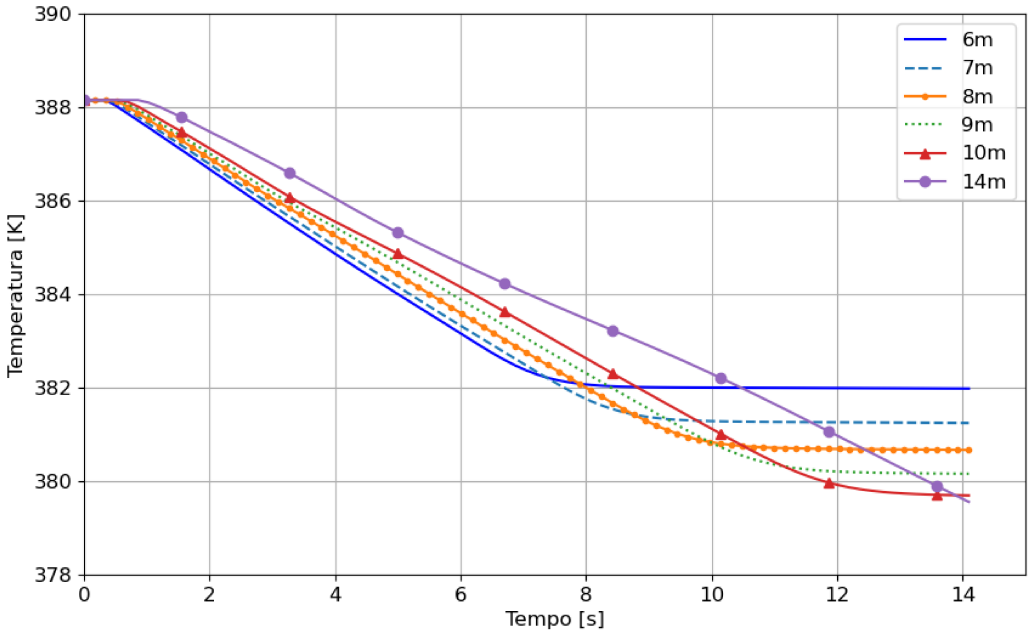

Figure 68: Estimated temperature at the outlet of CDU1 using previous axial sections — Case 5.

In CDU2 Case 3, which is still running, a total of 3.47 physical seconds has been simulated so far. Partial results are shown in Figures 69 and 70.

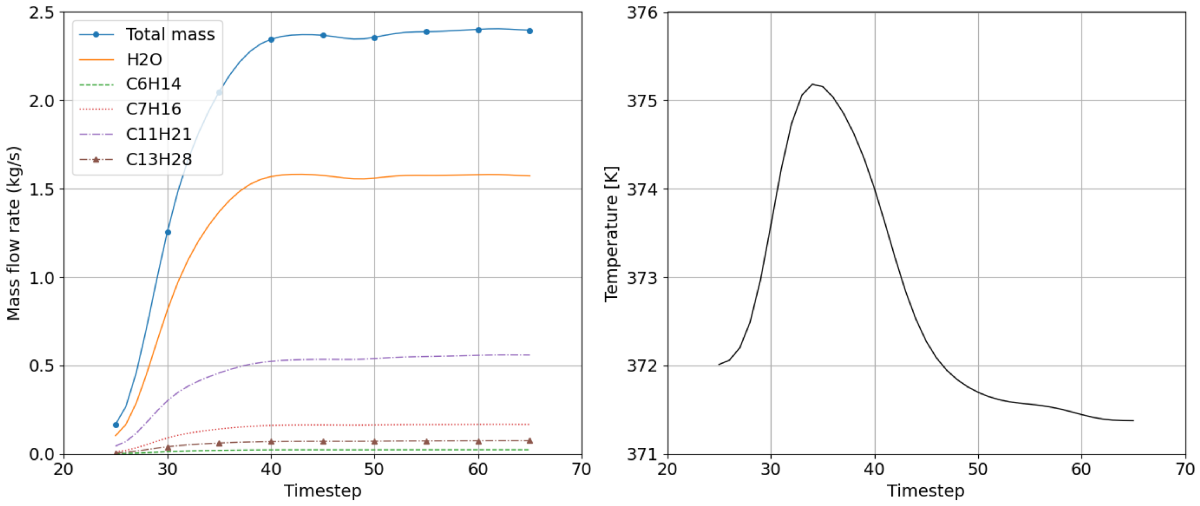

Figure 69: Filtered Lagrangian mass flow rate and temperature for CDU2 — Case 3 (Table 13).

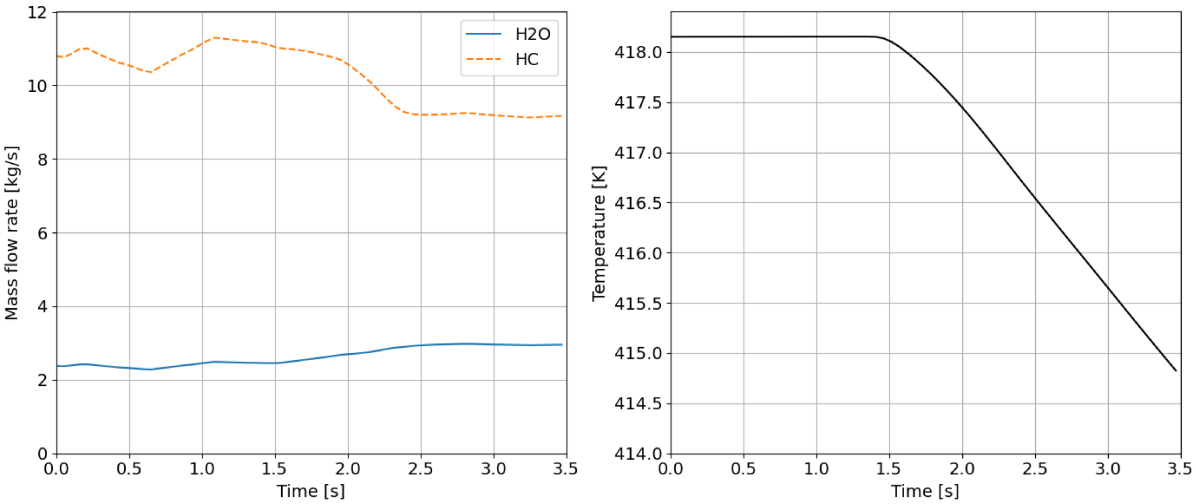

Figure 70: Gas-phase mass flow rate and outlet temperature for CDU2 — Case 3 (Table 13).

Using the same extrapolation method applied in CDU1, the temperature at the outlet of CDU2 was estimated based on earlier sections, as shown in Figure 71. However, since the gas-phase temperature converged only up to 5 m, this estimate is more uncertain.

$$f(x) = 10.549\, e^{-0.1442\, x} + 407.094. \tag{152}$$

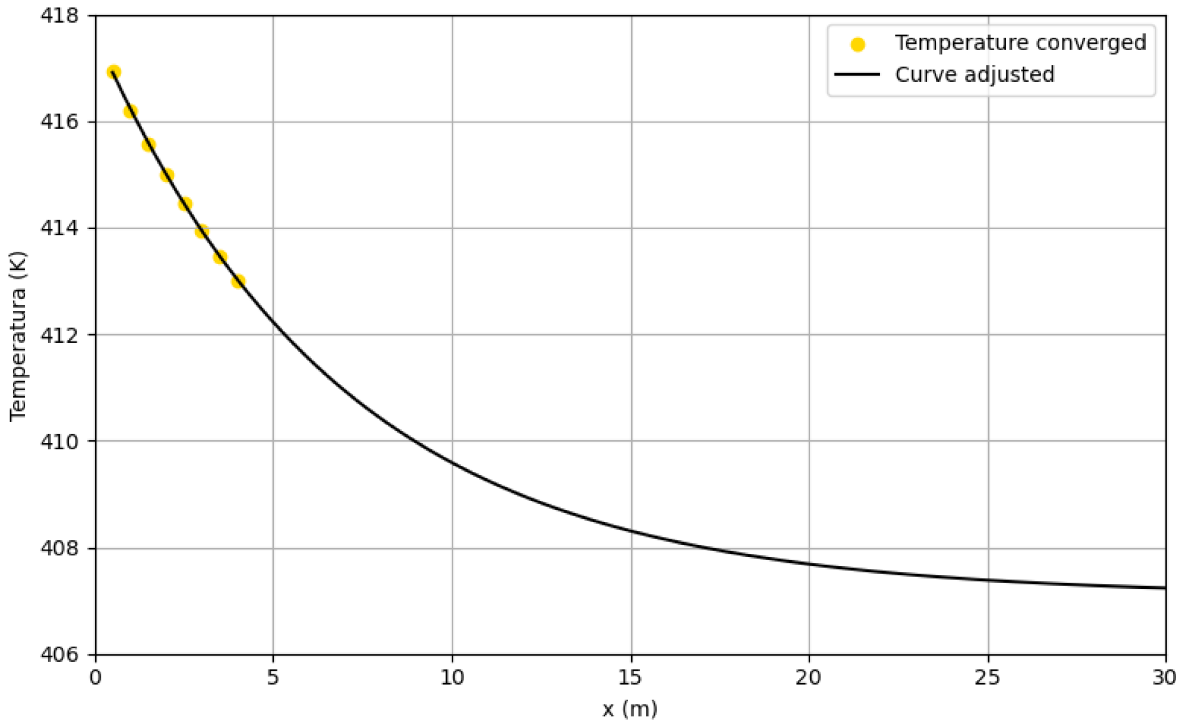

Figure 71: Estimated temperature at the outlet of CDU2 — Case 3 (Table 13).

Figure 71 still shows a significant discrepancy compared to Petrobras' expected results. This outcome was anticipated and indicates that more advanced modeling approaches should be tested in order to simulate CDU2 with higher accuracy.

The last simulation analyzed is presented in Table 14 and refers to CDU1 Case 6. A total of 3.05 physical seconds was simulated using the Mixture-Averaged model and unit parcel.

Table 14: Boundary conditions with Ghost-Cell — CDU1 Case 6.

BC	CDU1 Case 6
IB type	GC
Lagrangian transport model	Mixture-Averaged
DPM thermal model	ITC
Parcel	1
Diluent	NC7H16
Poisson model correction	Corrected

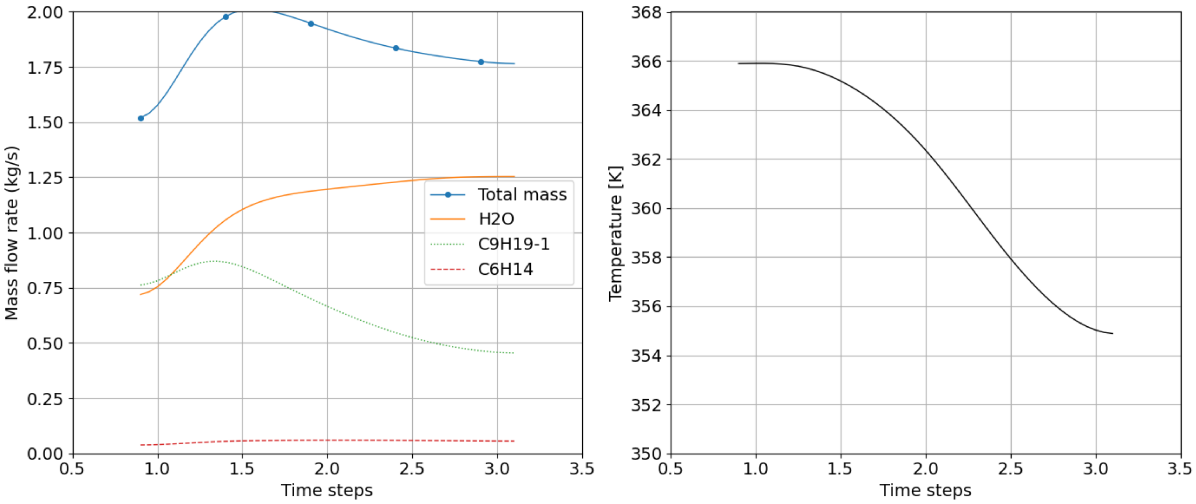

Figure 72: Filtered Lagrangian mass flow rate and temperature for CDU1 — Case 6 (Table 14).

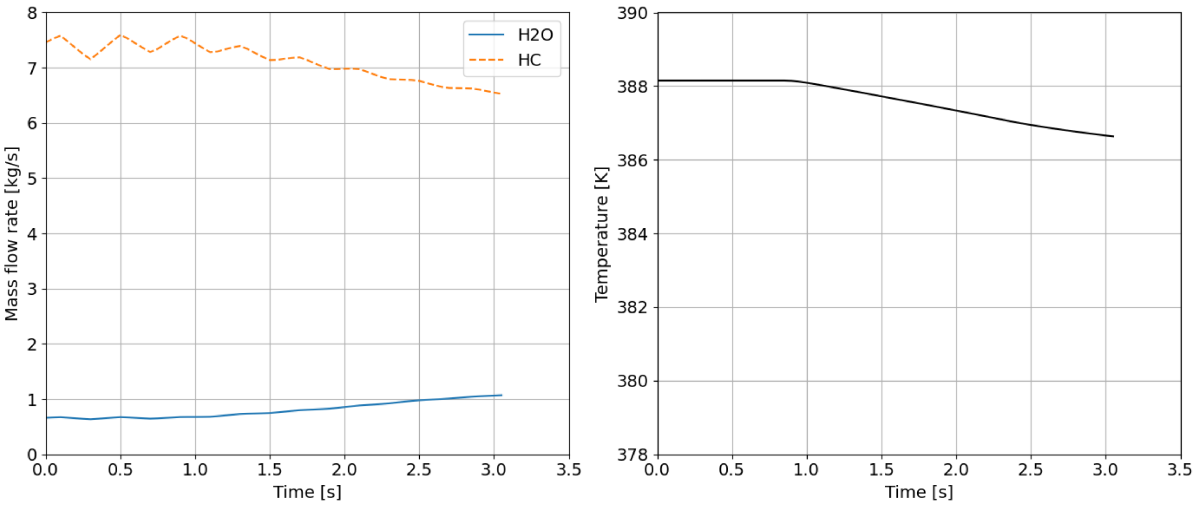

Figure 73: Gas-phase mass flow rate and outlet temperature for CDU1 — Case 6 (Table 14).

As reference values, equilibrium results obtained via PetroSim were used. For CDU2, the expected outlet temperature is approximately 373 K with about 10% of hydrocarbon condensation. For CDU1, the expected range is between 363 K and 368 K.

Based on the longest simulations (CDU1 Case 5 and CDU2 Case 3), the estimated final converged temperature in CDU2 is approximately 407.27 K for the gas phase and 371.5 K for the liquid phase. For CDU1, the estimates are 379.1 K (gas) and 358 K (liquid). Additional simulations with more sophisticated hypotheses are currently underway to further refine the model and improve comparison with real physical behavior.

9 Conclusion and Future Works

This work presented significant advancements in the modeling of multicomponent droplet evaporation, with several key contributions. The implementation and validation of models for differential diffusion, radiation effect, source term corrections in the PISO algorithm, coupling with thermodynamic databases, and the multicomponent evaporation model yielded promising results. Simulations of single droplet evaporation showed good agreement with the literature and experimental data, reinforcing the accuracy of the implemented methodologies.

As discussed throughout the work, the full methodology proposed by Sacomano has not yet been entirely implemented. Three key aspects remain to be addressed. First, the development of a dedicated solver is required to calculate the Spalding number as well as the total and species-specific evaporation rates. In this work, a simplified formulation was used, and a more accurate numerical model should be developed to account for the relationship between the species evaporation rates and their respective Spalding numbers. Second, the implementation of a non-ideal vapor-liquid equilibrium model is required to better represent real multicomponent systems. Third, a more robust framework is needed to handle the condition where evaporation and condensation occur simultaneously at equal rates.

In the current methodology, the total evaporation rate $\dot{m}$ is used to determine whether a droplet is evaporating or condensing, based on the sign of the Spalding number. The mass exchange of each component is then distributed proportionally through $\varepsilon_{vs,k} = \dot{m}_k/\dot{m}$. However, in specific scenarios where evaporation and condensation rates of different components are nearly identical, this approach can lead to unrealistic values of $\varepsilon_{vs,k}$, potentially exceeding unity, which is physically implausible. This limitation stems from the fact that both the mass and energy balances are intrinsically linked to $\dot{m}$. One might consider resolving this numerically through the modeling presented in Sacomano et al [29], which requires a more complex implementation. However, another potential solution would involve splitting ε_{vs} into two separate terms: one for evaporating components and

another for condensing components. Correspondingly, the Spalding number B_M would need to be evaluated separately for each group, introducing two distinct variables into the model.

To further validate the spray evaporation model, comparisons with experimental data are essential. A suitable comparison is the experimental methodology described by Rauch et al. [66], which could be employed to ensure consistency between simulation results and experimental analysis.

Regarding the large-scale simulations of CDU units, future efforts should focus on testing the code with the complete Sacomano model, which accounts explicitly for condensation phenomena. Once this is achieved, the FTC (Fully Transient Conduction) model should be activated. Even without a detailed analysis of droplet evaporation times, the use of the FTC model is likely necessary, considering the particle residence time estimated from their average velocity and the geometry of the pipe. Nevertheless, as Pinheiro [61] highlights, this poses significant numerical challenges, particularly in identifying suitable convergence criteria for each case.

After a detailed investigation of evaporation and condensation phenomena, such as testing FTC and multicomponent models and validating both coupled. The next step, the inclusion of chemical reactions, is essential for a more comprehensive analysis of the system. As noted by Da Silva [19], acid species formed during the evaporation of multicomponent fuels are responsible for corrosion inside heat exchanger tubes. This occurs due to the deposition of acid salts and the formation of liquid acids from hydrocarbon–water interactions. Therefore, incorporating chemical kinetics would provide a deeper understanding of the underlying degradation mechanisms and their impact on the process.

References

[1] Abramzon, B., and Sirignano, W. A. Droplet vaporization model for spray combustion calculations. *International Journal of Heat and Mass Transfer 32* (1989). https://10.1016/0017-9310(89)90043-4.

[2] Aggarwal, S. K., and Mongia, H. C. Multicomponent and high-pressure effects on droplet vaporization. *Journal of Engineering for Gas Turbines and Power 124* (2002). https://doi.org/10.1115/1.1423640.

[3] Albright, L. F. *Albright's Chemical Engineering Handbook*. CRC Press, 2009. https://doi.org/10.1201/9781420014389.

[4] Anderson, J. D. *Computational Fluid Dynamics: The basics with applications*. McGraw-Hill, Inc., 1995.

[5] Antonov, D. V., Fedorenko, R. M., and Strizhak, P. A. Characteristics of child droplets during micro-explosion and puffing of suspension fuel droplets. *International Journal of Heat and Mass Transfer 209* (2023). https://10.1016/j.ijheatmasstransfer.2023.124106.

[6] Atkins, P., and de Paula, J. *Physical Chemistry*, 8 ed. W. H. Freeman and Company, 2006.

[7] Atkins, P., and Jones, L. *Chemical Principles: The quest for insight*, 10 ed. W. H. Freeman and Company, 2010.

[8] Bird, R., Stewart, W., and E.N.Lightfoot. *Transport Phenomena*, 2 ed. John Wiley Sons Inc, 2002.

[9] Blanc, M. *J. Phys. 7* (1908), 825. https://doi.org/10.1051/jphystap:019080070082501.

[10] Brenn, G., Deviprasath, L. J., Durst, F., and Fink, C. Evaporation of acoustically levitated multi-component liquid droplets. *International Journal of Heat*

and Mass Transfer 50 (2007). https://doi.org/10.1016/j.ijheatmasstransfer.2007.07.036.

[11] Chapman, S., and Cowling, T. The kinetic theory of simple and composite monatomic gases : viscosity, thermal conduction, and diffusion. *Proceedings of the Royal Society of London. Series A, Containing Papers of a Mathematical and Physical Character 93* (1916). https://doi.org/10.1098/rspa.1916.0046.

[12] Chen, L., Liu, Z., Lin, Y., and Zhang, C. Different spray droplet evaporation models for non-ideal multi-component fuels with experimental validation. *International Journal of Heat and Mass Transfer 94* (2016). https://doi.org/10.1016/j.ijheatmasstransfer.2015.11.017.

[13] Clift, R., Grace, J., and Weber, M. *Bubbles, Drops, and Particles*. Dover Civil and Mechanical Engineering. Dover Publications, 2013.

[14] Coffee, T. P., and Heimerl, J. M. Transport algorithms for premixed, laminar steady-state flames. *Combustion and Flame 43* (1981). https://10.1016/0010-2180(81)90027-4.

[15] Continillo, G., and Sirignano, W. A. https://10.1016/S0082-0784(89)80209-7, issn = 00820784, issue = 1, journal = Symposium (International) on Combustion, title = Numerical study of multicomponent fuel spray flame propagation in a spherical closed volume, volume = 22, year = 1989.

[16] Cormen, T. H., Leiserson, C. E., Rivest, R. L., and Stein, C. *Introduction to algorithms*. The MIT Press, 2022.

[17] Crowe, C. T., Schwarzkopf, J. D., Sommerfeld, M., and Tsuji, Y. *Multiphase flows with droplets and particles: Second edition*. CRC Press, 2011.

[18] D., H. T. A hash table for c structures. http://troydhanson.github.io/uthash/. Accessed: 2025-02-28.

[19] da Silva, G. P. D. M. Electrolyte thermodynamic modeling for crude distillation units overhead systems. Dissertation. Federal University of Rio de Janeiro, 2017.

[20] Damasceno, M. M. R., de Freitas Santos, J. G., and Vedovoto, J. M. Simulation of turbulent reactive flows using a fdf methodology – advances in particle density control for normalized variables. *Computers and Fluids 170* (2018). https://10.1016/j.compfluid.2018.05.004.

[21] de Freitas Santos, J. G. Modelagem matemática e computational de escoamentos gás-sólido em malha adaptativa dinamica. Dissertation. Federal University of Uberlandia, 2018.

[22] de Freitas Santos, J. G. Advanced computational fluid dynamics in bloodstain pattern analysis: Investigating non-newtonian properties for forensic applications. Dissertation. Federal University of Uberlandia, 2024.

[23] Denbigh, K. G. *The Principles of Chemical Equilibrium: With applications in Chemistry and Chemical Engineering.* Cambridge University Press, 1957.

[24] Ding, H., Zhang, Y., Sun, C., Yang, Y., and Wen, C. Numerical simulation of supersonic condensation flows using eulerian-lagrangian and eulerian wall film models. *Energy 258* (2022). https://doi.org/10.1016/j.energy.2022.124833.

[25] Dixon-Lewis, G. Flame structure and flame reaction kinetics ii. transport phenomena in multicomponent systems. *Proceedings of the Royal Society of London. Series A. Mathematical and Physical Sciences 307* (1968). https://doi.org/10.1098/rspa.1968.0178.

[26] Feng, Z. G., and Michaelides, E. E. Drag coefficients of viscous spheres at intermediate and high reynolds numbers. *Journal of Fluids Engineering, Transactions of the ASME 123* (2001). https://doi.org/10.1115/1.1412458.

[27] Ferziger, J. H., Péric, M., and Street, R. *Computational Methods for Fluid Dynamics.* Springer, 2002.

[28] Filho, F. L. S., de Albuquerque Paixão, L. E., de Carvalho, F., Santos, A. C., and Vié, A. Investigations of the differential diffusion modeling

for hydrophilic fuelvapor in propagating spray flames. *Fuel 379* (2025). https://doi.org/10.1016/j.fuel.2024.133056.

[29] Filho, F. L. S., Santos, A. C., Vié, A., and Filho, G. C. K. A new robust modeling strategy for multi-component droplet heat and mass transfer in general ambient conditions. *International Journal of Heat and Mass Transfer 194* (2022). https://doi.org/10.1016/j.ijheatmasstransfer.2022.123102.

[30] Germano, M., Piomelli, U., Moin, P., and Cabot, W. H. A dynamic subgrid-scale eddy viscosity model. *Physics of Fluids A 3* (1991). https://10.1063/1.857955.

[31] Godsave, G. A. Studies of the combustion of drops in a fuel spray-the burning of single drops of fuel. *Symposium (International) on Combustion 4* (1953). https://10.1016/S0082-0784(53)80107-4.

[32] Goodwin, D., Moffat, H., and Speth, R. Cantera: An object-oriented software toolkit for chemical kinetics, thermodynamics, and transport processes. version 2.2.0. https://doi.org/10.5281/zenodo.48735.

[33] Goodwin, D. G. Cantera: An open-source, object-oriented software suite for combustion. In *NSF Workshop on Cyber-based Combustion Science* (2006).

[34] Harlow, F. H., and Amsden, A. A. A numerical fluid dynamics calculation method for all flow speeds. *Journal of Computational Physics 8* (1971). https://doi.org/10.1016/0021-9991(71)90002-7.

[35] Holzmann, G. The power of ten: Rules for developing safety-critical code, 2006. NASA.

[36] Hubbard, G. L., Denny, V. E., and Mills, A. F. Droplet evaporation: Effects of transients and variable properties. *International Journal of Heat and Mass Transfer 18* (1975). https://10.1016/0017-9310(75)90217-3.

[37] Irannejad, A., and Jaberi, F. Large eddy simulation of turbulent spray breakup and evaporation. *International Journal of Multiphase Flow 61* (2014). https://doi.org/10.1016/j.ijmultiphaseflow.2014.01.004.

[38] Jiang, J., Jiang, X., and Zhu, M. A computational study of preferential diffusion and scalar transport in nonpremixed hydrogen-air flames. *International Journal of Hydrogen Energy 40* (2015). https://doi.org/10.1016/j.ijhydene.2015.08.112.

[39] Kee, R. J., Coltrin, M. E., Glarborg, P., and Zhu, H. *Chemically Reacting Flow: Theory, Modeling, and Simulation*, 2 ed. John Wiley Sons Inc, 2018. https://doi.org/10.1002/9781119186304.

[40] Kitano, T., Nishio, J., Kurose, R., and Komori, S. Effects of ambient pressure, gas temperature and combustion reaction on droplet evaporation. *Combustion and Flame 161* (2014). https://doi.org/10.1016/j.combustflame.2013.09.009.

[41] Kuo, K. K., and Acharya, R. *Fundamentals of Turbulent and Multiphase Combustion*, 1 ed. John Wiley Sons Inc, 2012.

[42] Kuznetsov, V. R. Why does preferential diffusion strongly affect premixed turbulent combustion? Tech. Rep. 19940007847, Nasa, Center for Turbulence Research, 1992.

[43] Law, C. K., and Law, H. K. A d2-law for multicomponent droplet vaporization and combustion. *AIAA Journal 20* (1982). https://10.2514/3.51103.

[44] Leboissetier, A., Okong'O, N., and Bellan, J. Consistent large-eddy simulation of a temporal mixing layer laden with evaporating drops. part 2. a posteriori modelling. *Journal of Fluid Mechanics 523* (2005). https://doi.org/10.1017/S0022112004002101.

[45] Lefebvre, A. H., and McDonell, V. G. *Atomization and Sprays*, 2 ed. CRC Press, 2017.

[46] Li, J., and Mason, D. J. A computational investigation of transient heat transfer in pneumatic transport of granular particles. *Powder Technology 112* (2000). https://10.1016/S0032-5910(00)00302-8.

[47] Lilly, D. K. A proposed modification of the germano subgrid-scale closure method. *Physics of Fluids A 4* (1992). https://10.1063/1.858280.

[48] Marrero, T. R., and Mason, E. A. Gaseous diffusion coefficients. *Journal of Physical and Chemical Reference Data 1* (1972). https://10.1063/1.3253094.

[49] Mason, E. A., and Kronstadt, B. Graham's laws of diffusion and effusion. *Journal of Chemical Education 44* (1967). https://doi.org/10.1021/ed044p740.

[50] Matsuda, H., and Ochi, K. Liquid-liquid equilibrium data for binary alcohol + n-alkane (c 10-c16) systems: Methanol + decane, ethanol + tetradecane, and ethanol + hexadecane. *Fluid Phase Equilibria 224* (2004). https://doi.org/10.1016/j.fluid.2004.05.006.

[51] Maxwell, J. C. IV. On the dynamical theory of gases. *Philosophical Transactions of the Royal Society of London 157* (1867). https://doi.org/10.1098/rstl.1867.0004.

[52] Melo, R. R. *Modelagem e simulação de escoamentos turbulentos com efeitos térmicos, utilizando a metodologia da fronteira imersa e malha adaptativa*. PhD thesis, Federal University of Uberlandia, 2017.

[53] Mukundakumar, N., Efimov, D., Beishuizen, N., and van Oijen, J. A new preferential diffusion model applied to fgm simulations of hydrogen flames. *Combustion Theory and Modelling 25* (2021). https://doi.org/10.1080/13647830.2021.1970232.

[54] Neto, A. d. S. *Escoamentos Turbulentos: Análise Física e Modelagem Teórica*. Composer, 2020.

[55] Nomura, H., Ujiie, Y., Rath, H. J., Sato, J., and Kono, M. Experimental study on high-pressure droplet evaporation using microgravity conditions. *Symposium (International) on Combustion 26* (1996). https://doi.org/10.1016/S0082-0784(96)80344-4.

[56] Nourgaliev, R. R., and Theofanous, T. G. High-fidelity interface tracking in compressible flows: Unlimited anchored adaptive level set. *Journal of Computational Physics 224* (2007). https://doi.org/10.1016/j.jcp.2006.10.031.

[57] O'Connell, B. E. P. . J. M. P. . J. P. *The Properties of Gases and Liquids*, 5 ed. McGraw-Hill, 200'.

[58] Patankar, S. V., and Spalding, D. B. A calculation procedure for heat, mass and momentum transfer in three-dimensional parabolic flows. *International Journal of Heat and Mass Transfer 15* (1972). https://doi.org/10.1016/0017-9310(72)90054-3.

[59] Peters, B., Džiugys, A., and Navakas, R. A discrete approach to thermal conversion of solid fuel by the discrete particle method (dpm). In *10th International Conference Modern Building Materials, Structures and Techniques* (2010).

[60] Pinheiro, A. P. Lagrangian modeling of droplet evaporation. Dissertation. Federal University of Uberlandia, 2018.

[61] Pinheiro, A. P. *Eulerian-Lagrangian modelling of aviation kerosene spray breakup and evaporation.* PhD thesis, Federal University of Uberlandia, 2022.

[62] Pinheiro, A. P., Rybdylova, O., Zubrilin, I. A., Sazhin, S. S., Filho, F. L. S., and Vedovotto, J. M. Modelling of aviation kerosene droplet heating and evaporation using complete fuel composition and surrogates. *Fuel 305* (2021). https://doi.org/10.1016/j.fuel.2021.121564.

[63] Poinsot, T., and Veynante, D. *Theoretical and Numerical Combstion*, 3 ed. Aquaprint, 2011.

[64] Puckett, E. G., Almgren, A. S., Bell, J. B., Marcus, D. L., and Rider, W. J. A high-order projection method for tracking fluid interfaces in variable density incompressible flows. *Journal of Computational Physics 130* (1997). https://doi.org/10.1006/jcph.1996.5590.

[65] Ranz, W. E., and Jr., W. R. M. Evaporation from drops - part ii. *Chemical Engineering Progress 48* (1952).

[66] Rauch, B., Calabria, R., Chiariello, F., Clercq, P. L., Massoli, P., and Rachner, M. Accurate analysis of multicomponent fuel spray evaporation in turbulent flow. *Experiments in Fluids 52* (2012). https://doi.org/10.1007/s00348-011-1169-0.

[67] Rosli, M. A., Aziz, A. R. A., Ismael, M. A., Elbashir, N. O., A., E. Z. Z., Baharom, M., and Mohammed, S. E. Experimental study of micro-explosion and puffing of gas-to-liquid (gtl) fuel blends by suspended droplet method. *Energy 218* (2021). https://doi.org/10.1016/j.energy.2020.119462.

[68] Santos, A. C., Filho, F. L. S., and Vié, A. The general formulation of the energy equation and the impact of enthalpy diffusion on multi-component droplet heat and mass transfer. *International Journal of Heat and Mass Transfer 210* (2023). https://doi.org/10.1016/j.ijheatmasstransfer.2023.124172.

[69] Sazhin, S. *Droplets and Sprays*. Springer, 2014. https://doi.org/10.1007/978-1-4471-6386-2.

[70] Sazhin, S. S. Mono-component droplet heating and evaporation. abramzon and sirignano model. In *Heat and mass transfer in roplets* (2024).

[71] Sazhin, S. S., Elwardany, A., Krutitskii, P. A., Castanet, G., Lemoine, F., Sazhina, E. M., and Heikal, M. R. A simplified model for bi-component droplet heating and evaporation. *International Journal of Heat and Mass Transfer 53* (2010). https://doi.org/10.1016/j.ijheatmasstransfer.2010.06.044.

[72] Sazhin, S. S., Kristyadi, T., Abdelghaffar, W. A., and Heikal, M. R. Models for fuel droplet heating and evaporation: Comparative analysis. *Fuel 85* (2006). https://doi.org/10.1016/j.fuel.2006.02.012.

[73] Shinjo, J., Xia, J., Ganippa, L. C., and Megaritis, A. Physics of puffing and microexplosion of emulsion fuel droplets. *Physics of Fluids 26* (2014). https://10.1063/1.4897918.

[74] Shirolkar, J. S., Coimbra, C. F., and McQuay, M. Q. Fundamental aspects of modeling turbulent particle dispersion in dilute flows. *Progress in Energy and Combustion Science 22* (1996). https://doi.org/10.1016/S0360-1285(96)00006-8.

[75] Smith, J. M., Ness, H. C. V., Abbott, M. M., and Swihart, M. T. *Introduction to chemical engineering thermodynamics*, 8 ed. Mc Graw Hill Education, 2018.

[76] Spalding, D. B. Combustion of liquid fuels. *Nature 165* (1950). https://10.1038/165160a0.

[77] Starinskaya, E. M., Miskiv, N. B., Nazarov, A. D., Terekhov, V. V., Terekhov, V. I., Rybdylova, O., and Sazhin, S. S. Evaporation of water/ethanol droplets in an air flow: Experimental study and modelling. *International Journal of Heat and Mass Transfer 177* (2021). https://doi.org/10.1016/j.ijheatmasstransfer.2021.121502.

[78] Stefan, J. Über das gleichgewicht und die bewegung, insbesondere die diffusion von gasgemengen. *Sitzungsberichte der Kaiserlichen Akademie der Wissenschaften, Mathematisch-Naturwissenschaftliche Classe 63* (1871), 63–124.

[79] Stodt, M. F., Groeneveld, J. D., Mädler, L., Kiefer, J., and Fritsching, U. Microexplosions of multicomponent drops in spray flames. *Combustion and Flame 240* (2022). https://doi.org/10.1016/j.combustflame.2022.112043.

[80] Stone, H. L. Iterative solution of implicit approximations of multidimensional partial differential equations. *SIAM Journal on Numerical Analysis 5* (1968). https://doi.org/10.1137/0705044.

[81] Tonini, S., and Cossali, G. E. A novel formulation of multi-component drop evaporation models for spray applications. *International Journal of Thermal Sciences 89* (2015). https://doi.org/10.1016/j.ijthermalsci.2014.10.016.

[82] Vedovoto, J. M. *Mathematical and numerical modeling of turbulent reactive flows using a hybrid LES/PDF methodology.* PhD thesis, Federal University of Uberlandia, 2011.

[83] Venturi, D. N. *From Dilute to Dense Gas-Solid Flows Simultaion: The CFB riser case study. Dissertation. Federal University of Uberlandia.* PhD thesis, Federal University of Uberlandia, 2020.

[84] Villar, M. M. *Análise Numérica Detalhada de Escoamentos Multifásicos Bidimensionais.* PhD thesis, Federal University of Uberlandia, 2007.

[85] Wang, C., Dean, A. M., Zhu, H., and Kee, R. J. The effects of multicomponent fuel droplet evaporation on the kinetics of strained opposed-flow diffusion flames. *Combustion and Flame 160* (2013). https://doi.org/10.1016/j.combustflame.2012.10.012.

[86] White, F. M. *Fluid Mechanics*, 5 ed. Mc Graw-Hill Inc., 2002.

[87] Wilke, C. *A viscosity equation for gas mixtures*, 3 ed. McGraw-Hill, 2014.

[88] Wilke, C. R., and Lee, C. Y. Estimation of diffusion coefficients for gases and vapors. *Industrial Engineering Chemistry 47* (1955). https://doi.org/10.1021/ie50546a056.

[89] Wilms, J. *Evaporation of Multicomponent Droplets.* PhD thesis, Universitat Stuttgart, 2005.

[90] Woodrow, J. E. The laboratory characterization of jet fuel vapor and liquid. *Energy and Fuels 17* (2003). https://10.1021/ef020140p.

[91] Wörner, M. A compact introduction to the numerical modeling of multiphase flows. *Report Forschungszentrum Karlsruhe FZKA* (2003).

[92] Yang, J. R., and Wong, S. C. On the discrepancies between theoretical and experimental results for microgravity droplet evaporation. *International Journal of Heat and Mass Transfer 44* (2001). https://doi.org/10.1016/S0017-9310(01)00091-6.

[93] Yaws, C. Transport properties of chemicals and hydrocarbons: viscosity, thermal conductivity, and diffusivity of clto cl00 organics and ac to zr inorganic. *William Andrew Inc* (2009).

[94] Yaws, C. L. Handbook of thermodynamic and physical properties of chemical compounds and chemical properties. https://www.academia.edu/39804996/Yaws_Handbook_of_Thermodynamic_and_Physical_Properties_of_Chemical_Compounds_and_Chemical_Properties. Accessed: 2024-08-14.

[95] Yaws, C. L. *Chemical Properties Handbook: Physical, Thermodynamic, Environmental, Transport, Safety, and Health Related Properties for Organic and Inorganic Chemicals*. MC Graw Hill, 1999.

[96] Yuen, M. C., and Chen, L. W. On drag of evaporating liquid droplets. *Combustion Science and Technology 14* (1976). https://doi.org/10.1080/00102207608547524.

[97] Zhang, L., and Kong, S. C. Multicomponent vaporization modeling of bio-oil and its mixtures with other fuels. *Fuel 95* (2012). https://doi.org/10.1016/j.fuel.2011.12.009.

[98] Çengel, Y. A., and Cimbala, J. M. *Fluid Mechanics: Fundamentals and Application*, 3 ed. McGraw-Hill, 2014.